

Dear Editor,

We have revised our original manuscript titled: "Active tectonic field for CO₂ Storage management: Hontomín onshore study-case (SPAIN)", by Pérez-López et al., according to the revisions suggested by Pr. Graham Yielding and an anonymous reviewer (AR2) under the Open Discussion of Solid Earth.

We thank both reviewers their generous contribution. Firstly, we have revised Mr. Yielding's comments because this revision was more complex. Secondly, the anonymous AR2 comments were also faced. Definitively, both remarks have improved the original manuscript and focused the main goal, the study of the active tectonics applied in CO₂ storage, on the text. We hope that this revision response enough both reviewers and the SE editor. Both reviewers are thanked for their oportune and successful contributions.

The authors, March, 2020.

P.S. We have detected some minor mistakes and typos not noted by the reviewers that we have removed.

Answers step-by-step:

Dear Dr. Yielding,

Thank you very much for your time and effort in reviewing the manuscript under the open discussion of Solid Earth and your kind comments. You pointed accurately the main objective of the paper, "the reactivation of faults due to the injection of fluids and the potential for triggering earthquakes, within the vicinity of the CCS (Carbon Capture and Storage), and pilot plant facilities". According to the suggestion of anonymous reviewer #2, hereafter we refer to Geological Storage of CO₂ (GSC) instead of CCS.

We agree with you that the main goal of the paper was not the paleostrain evolution and global tectonic events recognized in the Basque-Cantabrian area and Duero and Ebro river basins (North part of Spain), but the role of the fault sets affecting the GSC by the present-day strain field. The high-quality outcrops in the near-field (<20 km) gave us a good chance to estimate different paleostrain local tensors affecting geological formations at different ages.

On the other hand, the controversy related to the assignment of geological ages to the different strain tensors calculated in geological outcrop is still an open debate. We well-know the problems to reconstruct paleostrain fields and how to match these results with large-scale tectonic events throughout the geological evolution of a geological basin. Of course, stress/strain axis rotations due to different paleogeographic constrains, magnetic field changes, among others, obviously difficult that reconstruction. As a matter of fact, the paleostrain reconstruction is always controversial, more if you take into account that all of our study is restricted to the local scale. This kind of analysis is always constrained by the quality of the outcrop and the ability to assign strain tensors to large-scale tectonic events affecting the studied area. We have indeed tried to match the paleostrain tensors calculated from slip fault data with those global tectonic events defined by other authors in the area. Perhaps, we have failed to suggest that this is only a local analysis.

Consequently, we accept to remove the paleostrain evolution from the manuscript. Instead, we have included the Mohr-Coulomb failure criterion applied to the fault pattern affecting the outcrop located in the Hontomín Pilot Plant (subsection 5.1 within the section 5. Discussion). Therefore, original figure 8 and figure 9 were removed and new figures were included: Figs. 8, 9, 10 and 11.

Ancient Fig. 8 (REMOVED): Upper left frame: Synthesis of the K' - map obtained from Giner-Robles et al. (2018) for the whole Iberian Peninsula from focal mechanism solutions. HPP is located between a triple junction of K' defined by compression towards the north, extension to the southeast and strike-slip to the west. Black dots are the earthquakes with focal mechanism solutions used. Sketches represent the e_y , S_{Hmax} trajectories obtained from the outcrops for early Triassic, Early Cretaceous, Late Cretaceous, Early Oligocene, Early – Middle Miocene and Present-day strain field from Herraiz et al. (2000). Main structures activated under the strain field defined are also included.

Ancient Fig. 9 (REMOVED): Tectonic field evolution of the Burgalesa Platform domain (20-km radius circle centred at HPP), interpreted from the paleostrain analysis. The regional tectonic field from other authors are also included. Ages were estimated from the HTM outcrops affecting geological well-dated deposits. N: extensional faulting; R: compressive faulting; SS: strike-slip faulting. Red and white means local paleostrain field, and red with white dots means superposed modern paleostrain field.

Concerning the inclusion of the fault-slip data from the outcrop HTM17, as suggested by Dr. Yielding, we have incorporated a new section. At the beginning of this work, it was a long discussion among the authors about the convenience either to describe this outcrop, having in mind the relevance of the site-effects, or to remove this outcrop from the huge amount of information we had to deal with. We have included the section 4.4 Cretaceous Outcrop HTM17 on the Hontomín Pilot Plant and several new figures.

New Figs. 8 and 9: Results of the paleostrain analysis of HTM17

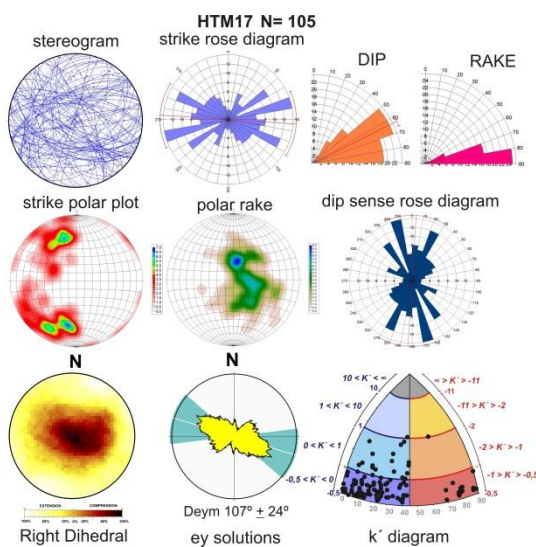


FIGURE 8

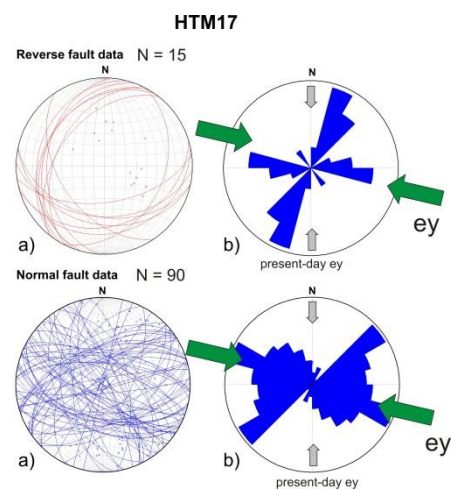


FIGURE 9

New Fig. 8. Fault data from the outcrop HTM17 located on top of the HPP. See figure 5 for the geographical location. Stereogram plot is lower hemisphere and Schmidt net.

New Fig. 9. Normal and reverse faults stereograms (lower hemisphere and Schmidt net), and rose diagrams measured in HTM17. Green arrows indicate the orientation of the local paleostrain field. Grey arrows indicate the orientation of the present-day regional stress field (Herraiz et al., 2000).

Besides, we have calculated how the present-day stress tensor affects to each strain tensor solution and fault sets as Yielding' suggestion. (Figure 10, Mohr-Coulomb failure criterion).

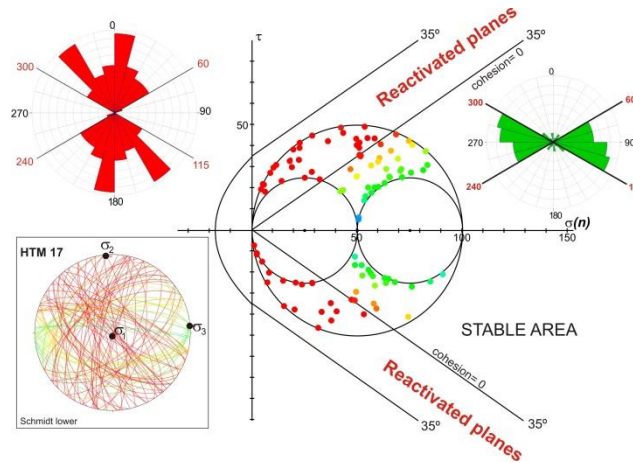


Figure 10. Mohr-Coulomb failure analysis for the fault-slip data measured in HTM17 under the present-day stress tensor determined by Herraiz et al. (2000). Red dots are faults reactivated, and green and orange dots are located within the stable zone. Red rose diagram shows the orientation of reactivated faults, between N-S to N60°E and from N115°E to N180°E. Green rose diagram shows the fault orientation for faults non-reactivated under the active stress field within the area. See text for further details.

Some sentences were modified from the abstract, introduction and other sections of the manuscript, concerning that HTM17 was not included here.

Finally, we don't agree with Dr. Yielding with the idea concerning the document has to be drastically rewritten. It is true that we have to include a new section describing the HTM17 outcrop and two new figures with the main data, and it is true again that we have rearranged the discussion section, by including the Mohr-Coulomb failure analysis applied to the HTM17 fracture pattern. However, the main analysis and focus of the manuscript is the same.

Nevertheless, we would like to thank to Pr. Yielding for putting the focus of our manuscript in the fault reactivation under fluid injection in GCE storage. We were some naïve to include a more complex analysis like the paleostrain reconstruction and matching with major tectonic events.

Thank you very much for your kind comments, revisions, and suggestions, that were properly focused on the aim of the manuscript, the role of the present-day strain field for GSC operations, and which definitively will improve the final manuscript.

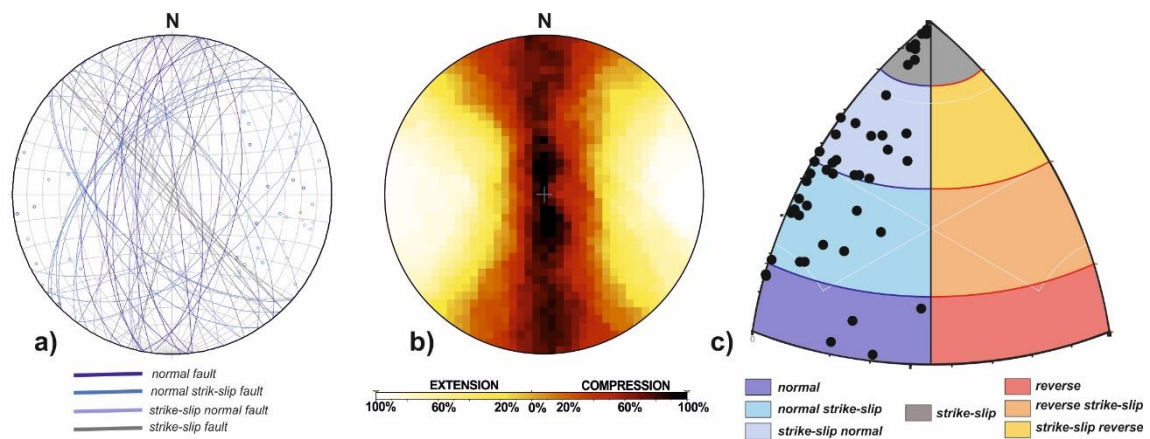


Figure 11. a) Stereogram and poles of fault sets (HTM17) reactivated under the present-day stress field suggested by Herraiz et al. (2000). b) Right-Dihedral of the reactivated fault sets. c) K'-strain diagram showing the type of fault for each fault-set.

NEW REFERENCES INCLUDED:

Allmendinger, R. W., Cardozo, N. C., and Fisher, D.: Structural Geology Algorithms: Vectors & Tensors: Cambridge, England, Cambridge University Press, 289 pp, 2012.

De Vicente, G. Muñoz, A., Giner, J.L.: Use of the Right Dihedral Method: implications from the Slip Model of Fault Population Analysis, Rev. Soc. Geol. España, 5(3-4), 7-19. 1992.

Goodman, R. E.: Introduction to Rock Mechanics, 2nd Edition. John Wiley & Sons, Inc., New York. 576 pp., 1989.

Labuz, J. F., Zang, A.: Mohr–Coulomb Failure Criterion. Rock Mech. Rock Eng., 45, 975–979, <https://doi.org/10.1007/s00603-012-0281-7>, 2012.

Pan, P., Wu, Z., Feng, X., Yan, F.: Geomechanical modeling of CO₂ geological storage: A review. J. Rock Mech. and Geotech. Eng., 8, 936-947, <http://dx.doi.org/10.1016/j.jrmge.2016.10.002>, 2016.

Xu, S.-S., A.F. Nieto-Samaniego, S.A. Alaniz-Álvarez: 3D Mohr diagram to explain reactivation of pre-existing planes due to changes in applied stresses. Rock Stress and Earthquakes – Xie (ed.), 739-745 p, 2010.

Answer to Anonymous referee #2 (AR2) related to the interactive comment on “Active tectonic field for CO₂ storage management: Hontomín onshore study-case (SPAIN)” by Pérez-López et al.

The authors (March, 2020)

First of all, thank you very much for your time and your effort, and for the constructive review of our work. We really feel that an open discussion improves the scientific results and we are willing to deal with it.

As detailed below, we answer all the points kindly provided by the Anonymous Referee #2 (hereafter AR2), in the same order he did.

We didn't analyze the past and present “stress” fields, we have analyzed the past and present “strain” fields. Although the orientations of both fields are similar, it is important to highlight the difference in terminology and concept between stress and strain. We have calculated strains. The Right Dihedral based on fault slip data yield “strain” and “paleostrain” fields. It is assumed that in the general case for the Anderson fault model, ϵ_y (the trajectory of maximum strain) is parallel to S_{Hmax} (maximum horizontal shortening) being different terms although (e.g. Giner-Robles et al. 2009). Therefore, the term strain is well used across the manuscript.

Our results do not evaluate “the risk” for leakage of CO₂ injection neither the possibility of triggering a M5 earthquake as AR2 suggests. RISK is a term that includes HAZARD plus VULNERABILITY plus EXPOSITION, and in our manuscript, we didn't calculate that. In our conclusions, we expose the fault sets and orientation according to the present-day stress orientation which are affecting the caprock and the vicinity. We also describe a low-cost methodology to obtain paleostrain data, fault sets and their relationship with the present-day stress field, and we suggest including this kind of low-cost analyses for long-term geological CO₂ storage (GSC).

On the other hand (**we have removed this expression from the manuscript obeying the suggestion of AR2**), for estimating the potential seismic triggering of active faults, more analyses have to be carried out, for example, the study of active faulting by tectonic geomorphology and paleoseismology (see McCalpin 1996 and Papanikolaou et al. 2016, for instance). Therefore, the risk assessment for leakage of CO₂ is out of the scope of our manuscript.

Comment 1a. AR2 said that the analysis we made is common in monitoring strategies for GSC management. We don't know any work about “strain inversion techniques” applied in GSC management so far. All the references suggested by AR2 are devoted to induced seismicity and the tectonic role in GSC management. We do not claim that we are pioneers in induced seismicity and tectonic studies on GSC. We simply present how the Structural Analysis of fault/slip data can improve the knowledge of the tectonic large-scale fault network for the potential seismic reactivation during fluid injection and time-depend scale for fluid stays. We have reinforced this idea by including this sentence at the end of the introduction section.

Comment 1b. In this point, we agree with AR2 regarding the terminology about Carbon Capture and Storage (CCS), geological storage even Carbon sequestration (discarded terminology that we have used in the conclusion section). Hence, we will use only one. We agree with the term of geological CO₂ storage (GSC) and therefore, **we have changed CCS (carbon capture and storage, and other some former term which was included in the manuscript and removed for the revised version) for the term GSC.**

Comment 1c. Once again, the “*risk assessment*” was not performed in our work. This confusion is relevant to solve, it could lead to major mistakes for managing GSC. We insist that we have not carried out any kind of “*risk analysis*”.

On the other hand, the expression used by AR2: “*extremely unlike*”, to describe the potential of triggering M5 earthquakes by active faults near the GSC is not relevant to determine the real seismic hazard. There is no formal reference to this sentence and therefore we have ignored it.

We have applied a physic model to estimate the total volume injected (yes, we did it in room conditions), from the official data (referenced in the manuscript), and then we have applied the McGarr’s (2014) approximation. Taking into account the uncertainties, our analysis “*should not be regarded as an absolute physical limit*”, paraphrasing McGarr (2014)’ words (page 1, ending sentence of the abstract section). According to McGarr (2014), the utility of the analysis that we have performed is “*to predict in advance of a planned injection whether there will be induced seismicity*”, and in the case of the Hontomín Pilot Plant, by the estimation of the “*total injected volume*” in a small-scale injection plant (yes, the utility of a small injection plant, as pointed out by Cook et al., 2014).

McGarr (2014) applied his approach for three cases: (1) wastewater injection, (2) hydraulic fracturing, and (3) geothermal injection. We have gone one step beyond by including geological storage of CO₂. We assume that the pore pressure increases from CO₂ injection, in a similar way that wastewater does (originally defined by Frohlich, 2012). **We have included this paragraph in the revised manuscript.**

Regarding **Lines 673 and 674: We agree with AR2** that we have calculated the volume in “*room conditions*” for estimating the total injected volume, but we disagree with AR2 that it is a wrong estimation. We have read the work from McGarr (2014), and we did not found a reference that the injected value for the McGarr equation (eq 13) should be in “*reservoir conditions*”. That means that our volume estimation was correct, and simply we have included “*room conditions*”.

Regarding the calculation of the maximum seismic moment Mo(max), originated by the total injected fluid, we included the next paragraph:

We have applied a physic model to estimate the total volume injected (room conditions), and then we have applied the McGarr’s (2014) approximation. The injection of 10 k tons of CO₂ in Hontomín (Gastine et al., 2017), represents an approximated injected volume of CO₂ of 5.56 x10⁶ m³ (room conditions). We have used the expression Mo(max) (Nm) = G ·ΔV (McGarr 2014, eq. 13), where G is the modulus of rigidity and for the upper limit is 3 x 10¹⁰ Pa, and ΔV is the

total injected volume (in room conditions). The result is $M_0(\max)$ equal to 1.67×10^{17} Nm (Joules), which corresponds to a maximum seismic moment magnitude $M_w(\max) = 5.45$, by applying the equation $M_w = (\text{Log } M_0(\max) - 9.05)/1.5$ from [Hanks and Kanamori \(1979\)](#); where Log is the logarithm to the base 10.

We agree with AR2 that we have to include this calculation in the revised manuscript. Also, it was a misprint of the result, the correct number is $M_w = 5.45$ instead of $M = 6.01$, by using the seismic moment magnitude instead of the Richter Magnitude. We have solved this and give thanks to AR2 for reviewing the math operations.

Regarding the Ubierna Fault System (UFS), we simply claim that it is necessary to know the seismic cycle of their active segments to know the possibility that small induced seismicity could trigger a natural earthquake by changing the strain conditions. Today, that question is not well-known but as a matter of fact, the study of the strain fields by inversion techniques and the relationships with the active faults in the vicinity is a good approach to get a realistic answer. Up to now, there is not a known model or work analyzing the seismic cycle of the UFS. Our statement about the paleostrain and present-day strain analysis is a suggestion for best practice in the long term geological storage, not a fact. Regarding the “seismic cycle” and missing references, we have included Scholz (2018), one of the most general explanations of a wide-used description of active faults and related references.

Comment 2. AR2 asked a statistical analysis to the fault dataset but the Fault Population analysis in Structural Geology is a statistical analysis itself, so we did it. Perhaps AR2 means a calculation of uncertainties from age outcrops associated with quality parameters measured on the field. In this sense, we do not find any quality differences between the faults striations measured on fault planes. Any field data with doubt or potential misinterpretation from the field data was directly obviated to avoid biased results. Only high-quality striations and fibers were measured (see annexed figure 1). Moreover, geological ages mapped in the outcrops are enough constrained to be homogenous for the paleostrain reconstructions.

Comment 3. Thank you very much for your time and your effort to improve our English style, although we are not pretty sure that all of your suggestions are correct. Anyway, all of your suggestions will be revised and included if so. As a non-native English speaker, we always use professional aid. Bearing in mind that the manuscript was written by three different authors and finally homogenized by the first one, the English style could oscillate in different parts of the text. Thanks indeed.

Minor comments in the supplementary doc: (Major questions, English grammar questions are no answered here). In total, 17 questions were faced and answered. Line number is for the annotated text of the supplementary doc by the reviewer.

Q1 (abstract). AR2 asks about the “tectonic parameters”: They are those parameters which characterize the tectonic field and framework: stress/strain parameters like $S_{H\max}$, ϵ_y , k' , R , natural heat-flow, Moho depth, crustal thickness, etc. In this case, the stress/strain ellipsoid

and strain trajectories, master faults, tectonic slip rates, were showed in our work. **WE HAVE INCLUDED THIS SENTENCE.**

Q2 (abstract). Did In Salah (Algeria) case analyze the “*tectonic strain field*”? Please give us a reference.

Q3 (abstract). The reviewer confuses **stress** with **strain** again. They could be related in space, but are different concepts, as we said before. (see comment 1c.)

Q4 (page3). Ancient literature does not mean outdated literature. Please, indicate more appropriate literature if so related to the first stages of GSC and why Pearce 2006 is obsolete.

Q5 (Line74). What do you mean by long-term monitoring? We are meaning about the expected life of the reservoir in geological terms, from hundreds to thousand years.

Q6 (Line92). Geomechanical models related to the active tectonic field is not the aim of the paper and is out of the scope.

Q7. The election of 20 km for the strain analysis from geological outcrops is well explained. (3. Method and Rationale, section 3.5).

Q8 (Line110). Ok, removed.

Q9 (Line113). Why should we indicate that Hontomín is a pilot plant before the geological framework? We don't know any reason to prioritize this. Geology is the key for underground storage.

Q10 (Line211). Geomorphic markers (misfit).

Q11 (Fig. 5). Some outcrops are close to 20 km but not exactly. Well, despite we use a GPS in the field, some outcrops were slightly out of 20 km but quite close to have influence in the geological map. We checked if outcrops were located about 20 km but not exactly. This is another reason to include the outcrops in a geological map.

Q12 (Line449). We strongly disagree. The tectonic field is relevant and their expressions are the master faults, they accommodate all of the deformations that it generates. The tectonic field and master faults are not independent concepts.

Line 592. Reference misprint removed (Alcalde et al., 2014.).

Line 631-640. One of the tectonic parameter to be considered is the crustal heat flow (see Q1). The relevance of this paragraph is to highlight that within intraplate areas large earthquakes could appear.

Line 643. Both strain fields.

Line 691. The use of focal mechanism solutions is crucial for understanding the failure mechanism in seismic prone areas. This information is world-wide used for the study of seismogenic faulting, modeling, earthquake hazard, seismic wave propagation, design of the seismic network, etc.

Line 693-696. Well, one thing is the permeability and lateral diffusion due to a single injection, and another thing is the mechanical behavior of the caprock under episodic injections. Both things have to be considered.

Minor remarks like the use of cap letters in Induced Seismicity and minor English grammar suggestions have been included in the revised manuscript.

NEW REFERENCES

Frohlich, C.: Two-year survey comparing earthquake activity and injection-well locations in the Barnett Shale, Texas. PNAS, vol. 109 (35), 13934 – 13938. 2012.

Hanks, T.C., Kanamori, H.: A Moment Magnitude Scale, J. Geophys. Res., 84 (B5), 2348–2350, <https://doi.org/10.1029/JB084iB05p02348>, 1979.

Scholz, C.: The seismic cycle. In *The Mechanics of Earthquakes and Faulting* (pp. 228-277). Cambridge: Cambridge University Press. 2018.

Active tectonic field for CO₂ Storage management: Hontomín onshore study-case (SPAIN)

Raúl Pérez-López¹, José F. Mediato¹, Miguel A. Rodríguez-Pascua¹, Jorge L. Giner-Robles²,
[Adrià Adrià](#) Ramos¹, Silvia Martín-Velázquez³, Roberto Martínez-Orío¹, Paula Fernández-Canteli¹

1. IGME – Instituto Geológico y Minero de España – Geological Survey of Spain. C/Ríos Rosas 23, Madrid 28003 – SPAIN. Email: r.perez@igme.es, jf.mediato@igme.es, ma.rodriguez@igme.es, a.amos@igme.es, ro.martinez@igme.es, paula.canteli@igme.es

2. Departamento de Geología y Geoquímica. Facultad de Ciencias. Universidad Autónoma de Madrid. Campus Cantoblanco, Madrid. SPAIN. Email: jorge.giner@uam.es

3. Universidad Rey Juan Carlos. Email: silvia.martin@urjc.es

Abstract

*One of the concerns of underground CO₂ onshore storage is the triggering of Induced Seismicity and fault reactivation **by pore pressure increasing**. Hence, a comprehensive analysis of the tectonic parameters involved in the storage rock formation is mandatory for safety management operations. Unquestionably, active faults and seal faults depicting the storage bulk are relevant parameters to be considered. However, there is a lack of analysis of the active tectonic strain field affecting these faults during the CO₂ storage monitoring. The advantage of reconstructing the tectonic field is the possibility to determine the strain trajectories and describing the fault patterns affecting the reservoir rock. In this work, we adapt a methodology of systematic geostructural analysis to the underground CO₂ storage, based on the calculation of the strain field and defined by the strain field from kinematics indicators on the fault planes (e_y and e_x for the maximum and minimum horizontal shortening respectively). This methodology is based on statistical analysis of individual strain tensor solutions obtained from fresh outcrops **from Triassic to Miocene**. Consequently, we have collected 447 fault data in 32 field stations located within a 20 km radius. The understanding of the fault sets role for underground fluid circulation can also be established, helping for further analysis about CO₂ leakage and seepage. We have applied this methodology to Hontomín*

Código de campo cambiado

Código de campo cambiado

Código de campo cambiado

Código de campo cambiado

Código de campo cambiado

Código de campo cambiado

Código de campo cambiado

33 onshore CO₂ storage facilities (Central Spain). The geology of the area and the number
34 of high-quality outcrops, made this site as a good candidate for studying the strain field
35 from kinematics fault analysis. The results indicate a strike-slip tectonic regime with the
36 maximum horizontal shortening with N160°E and N50°E trend for local regime, which
37 activates NE-SW strike-slip faults ~~and NE-SW compressional faults~~. A regional
38 extensional tectonic field was also recognized with N-S trend, which activates ~~EN-W-S~~
39 ~~compressional-extensional~~ faults, ~~and NNE-SSW plus and NNW-SSE strike-slip faults~~,
40 measured in the Cretaceous limestone on top of the Hontomín facilities. Monitoring of
41 ~~E-W~~ these faults within the reservoir is suggested in addition with the possibility of
42 obtaining focal mechanism solutions for micro earthquakes ($M < 3$).

43

44 Keywords: onshore CO₂ storage, tectonic field, paleostrain analysis, active fault,
45 Hontomín onshore pilot-plant.

46

47 1. INTRODUCTION

48 Industrial made-man activities generate CO₂ that could change the chemical balance of
49 the atmosphere and their relationship with the geosphere. The Geological Carbon
50 Storage (GSC) ~~Carbon capture and sequestration (CCS)~~ appears as a good choice to
51 reduce the CO₂ gas emission to the atmosphere (Christensen, 2004), allowing the
52 industry increasing activity with a low pollution impact. There is a lot of literature about
53 what must have a site to be a potential underground storage suitable to ~~CCS-GSC~~ (e.g.
54 Chu, 2009; Orr, 2009; Goldberg et al., 2010 among others). The reservoir sealing, the
55 caprock, permeability and porosity, plus injection pressure and volume injected, are the
56 main considerations to choose one geological subsurface formation as the CO₂ host-
57 rock. In this frame, the tectonic active field is considered in two principal ways: (1) to

58 prevent the fault activation and earthquakes triggering, with the consequence of leakage
59 and seepage, and (2) the long-term reservoir behavior, understanding as long-term from
60 centennial to millennial time-span. Therefore, what is the long-term behavior of
61 CCSGSC? What do we need to monitor for a safe CCS-GSC management? [Winthaegen](#)
62 [et al. \(2005\)](#) suggest three subjects for monitoring: (a) the atmosphere air quality near
63 the injection facilities, due to the CO₂ toxicity (values greater than 4%, see [Rice, 2003](#)
64 and [Permentier et al., 2017](#)), (b) the overburden monitoring faults and wells and (c) the
65 sealing of the reservoir. The study of natural analogues for CCS-GSC is a good strategy
66 to estimate the long-term behavior of the reservoir, considering parameters as the
67 injected CO₂ pressure and volume, plus the brine mixing with CO₂ ([Pearce, 2006](#)).
68 Hence, the prediction of site performance over long timescales also requires an
69 understanding of CO₂ behavior within the reservoir, the mechanisms of migration out of
70 the reservoir, and the potential impacts of a leak on the near surface environment. The
71 assessments of such risks will rely on a combination of predictive models of CO₂
72 behavior, including the fluid migration and the long-term CO₂-porewater-mineralogical
73 interactions ([Pearce, 2006](#)). Once again, the tectonic active field interacts directly on
74 this assessment. Moreover, the fault reactivation due to the pore pressure increasing
75 during the injection and storage has also to be considered ([Röhmman et al., 2013](#)).
76 Despite the uplift measure by [Röhmman et al. \(2013\)](#) are submillimeter (c.a. 0.021 mm)
77 at the end of the injection processes, given the ongoing occurrence of microearthquakes,
78 long-term monitoring is required. The geomechanical and geological models predict the
79 reservoir behavior and the caprock sealing properties. The role of the faults inside these
80 models is crucial for the tectonic long-term behavior and the reactivation of faults that
81 could trigger earthquakes.

82 Concerning the Induced Seismicity, Wilson et al. (2017) published the Hi-Quake
83 database, with a classification of all man-made earthquakes according to the literature,
84 in an online repository (<https://inducedearthquakes.org/>, last access on May, 2019). This
85 database includes 834 projects with proved Induced Seismicity, where two different
86 cases with earthquakes as large as M 1.7, detected in swarms about 9,500
87 microearthquakes, are related to ~~CCS-GSC~~ operations. Additionally, Foulger et al.
88 (2018) pointed out that ~~CCS-GSC~~ can trigger earthquakes with magnitudes lesser than
89 M 2, namely the cases described in their work are as large as M 1.8, with the epicenter
90 location 2 km around the facilities. McNamara (2016) described a comprehensive
91 method and protocol for monitoring ~~CCS-GSC~~ reservoir for the assessment and
92 management of Induced Seismicity. The knowledge of active fault patterns and the
93 stress/strain field could help on designing monitoring network and identifying those
94 faults capable ~~for~~ of triggering micro-earthquakes ($M < 2$) and/or breaking the sealing
95 for leakage (patterns of open faults for low-permeability CO₂ migration).

96 In this work, we propose that the description, the analysis and establishment of the
97 tectonic strain field have to be mandatory for long-term ~~CCS-GSC~~ monitoring and
98 management, implementing the fault behavior in the geomechanical models. This
99 analysis does not increase the cost for long-term monitoring, given that they are low-
100 cost and the results are acquired in a few months. Therefore, we propose a methodology
101 based on the reconstruction of the strain field from the classical studies in geodynamics
102 (Angelier, 1979 and 1984; Reches, 1983; Reches, 1987). As a novelty, we introduce the
103 strain fields (SF) analysis between 20 away from the subsurface reservoir deep
104 geometry, under the area of influence of induced seismicity for fluid injection. The
105 knowledge of the strain field at local scale allows ~~to classify~~ classifying the type of
106 faulting and their role for leakage processes, whilst the regional scale explores the

107 | tectonic active ~~faults which~~faults that could affect the reservoir. The methodology is
108 | rather simple, taking measures of slickensides and striations on fault planes to establish
109 | the orientation of the maximum horizontal shortening (e_y), and the minimum horizontal
110 | shortening (e_x) -for the strain tensor. The principal advantage of the SF analysis is the
111 | directly classification of all the faults involved into the geomechanical model and the
112 | prediction of the failure parameters. Besides, a Mohr-Coulomb failure analysis was
113 | performed to the fault pattern recognized in the Cretaceous outcrop located on top of the
114 | pilot plant.

115 | The tectonic characterization of the ~~CCS-GSC~~ of Hontomín was implemented in the
116 | geological model described by Le Gallo and de Dios (2018). Beyond the use of Induced
117 | Seismicity and potentially active faults, the scope of this method is to propose an initial
118 | ~~analysis protocol~~ to manage underground storage operations. We present how the
119 | Structural Analysis of fault/slip data can improve the knowledge of the tectonic large-
120 | scale fault network for the potential seismic reactivation during fluid injection and time-
121 | depend scale for fluid stays.

122

123 2. HONTOMÍN ONSHORE STUDY CASE

124 2.1 Geological description of the reservoir

125 | The CO₂ storage site of Hontomín is enclosed in the southern section of the Mesozoic
126 | Basque–Cantabrian Basin, known as Burgalesa Platform (Serrano and Martínez del
127 | Olmo, 1990; ~~;~~ Tavani, 2012), within the sedimentary Bureba Basin (**Fig. 1**). This
128 | geological domain is located in the northern junction of the Cenozoic Duero and Ebro
129 | basins, forming an ESE-dipping monocline bounded by the Cantabrian Mountains
130 | Thrust to the north, the Ubierna Fault System (UFS) to the south and the Asturian
131 | Massif to the west (**Fig. 1**).

132 The Meso-Cenozoic tectonic evolution of the Burgalesa Platform starts with a first rift
133 period during Permian and Triassic times ([Dallmeyer and Martínez-García, 1990](#);
134 [Calvet et al., 2004](#); ~~[Dallmeyer and Martínez-García, 1990](#)~~), followed by a relative
135 tectonic quiescence during Early and Middle Jurassic times (e.g. [Aurell et al., 2002](#)).

136 The main rifting phase took place during the Late Jurassic and Early Cretaceous times,
137 due to the opening of the North Atlantic and the Bay of Biscay-Pyrenean rift system
138 ([García-Mondéjar et al., 1986](#); [Le Pichon and Sibuet, 1971](#); [Lepvrier and Martínez-](#)
139 [García, 1990](#); ~~[García—Mondéjar et al., 1996](#)~~; ~~[Le Pichon and Sibuet, 1971](#)~~; ~~[Lepvrier and](#)~~
140 ~~[Martínez-García, 1990](#)~~; [Roca et al., 2011](#); [Tugend et al., 2014](#)). The convergence
141 between Iberia and Eurasia from Late Cretaceous to Miocene times triggered the
142 inversion of previous Mesozoic extensional faults and the development of [an](#) E-W
143 orogenic belt (Cantabrian domain to the west and Pyrenean domain to the east) formed
144 along the northern Iberian plate margin ([Muñoz, 1992](#); [Gómez et al., 2002](#); ~~[Muñoz,](#)~~
145 ~~[1992](#)~~; [Vergés et al., 2002](#)).

146 The [Hontomín](#) facilities are located within the Basque-Cantabrian Basin (**Fig. 1b**). [The](#)
147 [geological reservoir structure is bordered by the UFS to the south and west, by the Poza](#)
148 [de la Sal diapir and the Zamanzas Popup structure \(Carola, 2014\) to the north and by the](#)
149 [Ebro Basin to the east \(Fig. 1\). The structure is defined as a forced fold related dome](#)
150 [structure \(Tavani et al., 2013; Fig. 2\), formed by an extensional fault system with](#)
151 [migration of evaporites towards the hanging wall during the Mesozoic \(Soto et al.,](#)
152 [2011\). During the tectonic compressional phase, associated with the Alpine Orogeny](#)
153 [affecting the Pyrenees, the right-lateral transpressive inversion of the basement faults](#)
154 [was activated, along with the reactivation of transverse extensional faults \(Fig. 2;](#)
155 [Tavani et al., 2013; Alcalde et al., 2014\).](#)

156 ~~This reservoir is a deep saline aquifer developed in fractured Jurassic carbonates, with a~~
157 ~~low porous permeability matrix, located at almost 1,500 m depth (Alcalde et al., 2013).~~
158 ~~The Hontomín geological structure was described by Alcalde et al. (2013) and Le Gallo~~
159 ~~and de Dios (2018), and it is defined as a fold-related dome (Tavani et al., 2013). The~~
160 ~~reservoir structure is associated to the Cenozoic extensional tectonic stages, according~~
161 ~~to these authors. The present day geological structure is related with the reactivation by~~
162 ~~a tectonic compressional phase during the Cenozoic Pyrenees compression (Alcalde et~~
163 ~~al., 2013).~~

164 ~~The Hontomín structure is bordered by the UFS to the south and west, by the Poza de la~~
165 ~~Sal diapir and the Zamanzas Popup structure (Carola, 2014) to the north and by the~~
166 ~~Ebro Basin to the east (Fig. 1). The structure has been classified as forced fold-related~~
167 ~~dome structure (Tavani et al., 2013; Fig. 2), which was formed by an extensional fault~~
168 ~~system with migration of evaporites towards the hanging wall during the Mesozoic~~
169 ~~(Soto et al., 2011). During the tectonic compressional phase, associated with Cenozoic~~
170 ~~tectonics affecting the Pyrenees, the right lateral transpressive inversion of the basement~~
171 ~~faults was activated, plus the reactivation of transverse extensional faults (Fig. 2; Tavani~~
172 ~~et al., 2013; Alcalde et al., 2014).~~

173 ~~At the HPP, t~~The target reservoir and seal formations consist of Lower Jurassic marine
174 carbonates, arranged in an asymmetric dome-like structure (**Fig. 2**) with an overall
175 extent of 15 km² and located at 1,485 m of depth (Alcalde et al., 2013, 2014; Ogaya et
176 al., 2013). The target CO₂ injection point is a saline aquifer formed by a dolostone unit,
177 known as “Carniolas”, and an oolitic limestone of the Sopeña Formation, both
178 corresponding to Lias in time (Early Jurassic). The estimated porosity of the Carniolas
179 reaches over 12% (Ogaya et al., 2013; Le Gallo and de Dios, 2018) and it is slightly
180 lower at the Carbonate Lias level (8.5% in average). The reservoir levels contain saline

181 water with more than 20 g/l of NaCl and very low oil content. The high porosity of the
182 lower part of the reservoir (i.e., the Carniolas level) is the result of secondary
183 dolomitization and different fracturing events (Alcalde et al., 2014). The minimum
184 thickness of the reservoir units is 100 m. The potential upper seal unit comprises Lias
185 marlstones and black shales from a hemipelagic ramp (Fig. 2); Pliensbachian and
186 Toarcian) of the “Puerto del Pozazal” and Sopenña Formations.

187

188 2.2 Regional tectonic field

189 The tectonic context of HPP has been described from two different approaches: (1) the
190 tectonic style of the fractures bordering the Hontomín reservoir (De Vicente et al., 2011;
191 Tavani et al., 2011) and (2) the tectonic regional field described from earthquakes with
192 mechanism solutions and GPS data (Herraiz et al., 2000; Stich et al., 2006; De Vicente
193 et al., 2008).

194 (1) The tectonic style of the Bureba Basin was described by De Vicente et al. (2011),
195 which classified the Basque-Cantabrian Cenozoic Basin (Fig. 1a) as transpressional
196 with contractional horsetail splay basin. The NW-SE oriented Ventaniella fault (Fig.
197 1a), includes the UFS in the southeastward area, being active between the Permian and
198 Triassic period, and strike-slip during the Cenozoic contraction. In this tectonic
199 configuration, the Ubierna Fault is ~~affects~~ as a right-lateral strike-slip fault. These
200 authors pointed out the sharp contacts between the thrusts and the strike-slip faults in
201 this basin. Furthermore, Tavani et al. (2011) also described complex Cenozoic tectonic
202 context where right-lateral tectonic style reactivated WNW-ESE trending faults. Both
203 the Ventaniella and the Ubierna faults acted as transpressive structures forming 120 km
204 long and 15 km wide of the UFS, and featured by 0.44 mm/yr of averaged tectonic
205 strike-slip deformation between the Oligocene and the present day. The aforementioned

206 authors described different surface segments of the UFS of right-lateral strike-slip
207 ranging between 12 and 14 km length. The structural data collected by [Tavani et al.](#)
208 [\(2011\)](#) pointed out the 60% of data correspond to right lateral strike-slip with WNW-
209 ESE trend, together with conjugate reverse faulting with NE-SW, NW-SE and E-W
210 trend, and left-lateral strike-slip faults N-S oriented. They concluded that this scheme
211 could be related to a transpressional right-lateral tectonic system with a maximum
212 horizontal compression, S_{Hmax} , striking N120°E. Concerning the geological evidence of
213 recent sediments affected by tectonic movements of the UFS, [Tavani et al. \(2011\)](#)
214 suggest Middle Miocene in time for this tectonic activity. However, geomorphic
215 | markets (river and valley geomorphology) could indicate tectonic activity at present-
216 times. All of these data correspond to regional or small-scale data collected to explain
217 the Basque-Cantabrian Cenozoic transpressive basin. The advantage of the
218 methodology proposed here to establish the tectonic local regime affecting the reservoir,
219 is the searching for local-scale tectonics (20 km sized), and the estimation of the depth
220 for the non-deformation surface for strata folding in transpressional tectonics ([Lisle et](#)
221 [al., 2009](#)).

222 (2) Regarding the stress field from earthquake focal mechanism solutions, [Herraiz et al.](#)
223 [\(2000\)](#) pointed out the regional trajectories of S_{Hmax} with NNE-SSW trend, and with a
224 NE-SW S_{Hmax} trend from slip-fault inversion data. [Stich et al. \(2006\)](#) obtained the stress
225 field from seismic moment tensor inversion and GPS data. These authors pointed out a
226 NW-SE Africa-Eurasia tectonic convergence at tectonic rate of 5 mm/yr approximately.
227 However, no focal mechanism solutions are found within the Hontomín area (20 km)
228 and only long-range spatial correlation could be made with high uncertainty (in time,
229 space and magnitude). The same lack of information appears in the work of [De Vicente](#)
230 [et al. \(2008\)](#), with no focal mechanism solutions in the 50 km surrounding the HPP. In

231 | this work, these authors classified the tectonic regime ~~within the study area~~ as uniaxial
232 | extension to strike-slip with NW-SE S_{Hmax} trend.
233 | Regional data about the tectonic field ~~within the HPP (Bureba basin)~~, inferred from
234 | different works (Herraiz et al., 2000; Stich et al., 2006; De Vicente et al., 2008, 2011;
235 | Tavani et al., 2011; Tavani, 2012), show differences for the S_{Hmax} ~~trend~~. These works
236 | explain the tectonic framework for regional scale, ~~Nevertheless~~, local tectonics could
237 | determine the low permeability and the potential ~~Induced-induced Seismicity-seismicity~~
238 | within the Hontomín reservoir. In the next section, we have applied the methodology
239 | described at the section 3 of this manuscript, in order to compare the regional results
240 | from these works and to establish the tectonic evolution of the Burgalesa Platform.

241

242 | 2.3 Strategy of the ENOS European Project

243 | Hontomín pilot-plant (HPP) for CO₂ onshore storage is the only one in Europe
244 | recognized as a key-test-facility, and it is managed and conducted by CIUDEN
245 | (*Fundación Ciudad de la Energía*). ~~This~~ The HPP is located within the province of
246 | Burgos (**Fig. 1b**), in the northern central part of Spain.

247 | The methodology proposed in this work and its application for long-term onshore ~~CCS~~
248 | GSC managing in the frame of geological risk, is based on the strain tensor calculation,
249 | as part of the objectives proposed in the European project “ENabling Onshore CO₂
250 | Storage in Europe” (ENOS). The ENOS project is an initiative of CO₂GeoNet, the
251 | European Network of Excellence on the geological storage of CO₂ for supporting
252 | onshore storage and fronting the associated troubles as ~~CCS-GSC~~ perception, the safe
253 | storage operation, potential leaking management and health, and environmental safety
254 | (Gastine et al., 2017). ENOS combines a multidisciplinary European project, which
255 | focuses in onshore storage, with the demonstration of best practices through pilot-scale

256 projects in the case of Hontomín facilities. Moreover, this project claims for creating a
257 favorable environment for CCS-GSC onshore through public engagement, knowledge
258 sharing, and training (Gastine et al., 2017). In this context, the work-package WP1 is
259 devoted to “ensuring safe storage operations”. ~~The IGME team is committed to develop
260 and to carry out a technology to determine the active strain field affecting the sub-
261 surface reservoir and fault patterns and to assign the fault type for the estimation of
262 potential fault patterns as low permeability paths as well.~~

263

264 3. METHODS AND RATIONALE

265 The lithosphere remains in a permanent state of deformation, related to plate tectonics
266 motion. Strain and stress fields are the consequence of this deformation on the upper
267 lithosphere, arranging different fault patterns that determine sedimentary basins and
268 geological formations. Kinematics of these faults describes the stress/strain fields, for
269 example measuring grooves and slickensides on fault planes (see Angelier, 1979,
270 Reches, 1983 among others). The relevance of the tectonic field is that stress and strain
271 determine the earthquake occurrence by the fault activity. In this work, we have
272 performed a brittle analysis of the fault kinematics, by measuring slickenfiber on fault
273 planes (~~dip-/ D dip direction and rake~~), in several outcrops in the surroundings of the
274 onshore reservoir. ~~These faults were active during the Mesozoic, and from Late
275 Miocene to Quaternary.~~ To carry out the methodology proposed in this work, the study
276 area was divided in a circle with four equal areas, and we searched outcrops of fresh
277 rock to perform the fault kinematic analysis. This allows establishing a realistic tectonic
278 very-near field to be considered during the storage seismic monitoring and long-term
279 management. Finally, we have studied the fault plane reactivation by using the Mohr-

280 | [Coulomb failure criterion \(Pan et al., 2016\), from the fault pattern obtained in the](#)
281 | [Cretaceous limestone outcrop located on top of the HPP facilities.](#)

283 | [23.1 Paleostrain Analysis](#)

284 | We have applied the strain inversion technique to reconstruct the tectonic field
285 | (paleostrain evolution), affecting the Hontomín site between the Triassic, Jurassic,
286 | Cretaceous and Neogene ages (late Miocene to present times). For a further
287 | methodology explanation, see [Etchecopar et al. \(1981\)](#), [Reches \(1983\)](#) and [Angelier](#)
288 | [\(1990\)](#). The main assumption for the inversion technique of fault population is the self-
289 | similarity to the scale invariance for the stress/strain tensors. This means that we can
290 | calculate the whole stress/strain fields by using the slip data on fault planes and for
291 | homogeneous tectonic frameworks. The strain tensor is an ellipsoid defined by the
292 | orientation of the three principal axes and the shape of the ellipsoid (k). This method
293 | assumes that the slip-vectors, obtained from the pitch of the striation on different fault
294 | planes, define a common strain tensor or a set in a homogeneous tectonic arrangement.
295 | We assume that the strain field is homogeneous in space and time, the number of faults
296 | activated is greater than five and the slip vector is parallel to the maximum shear stress
297 | (τ).

298 | The inversion technique is based on the Bott equations ([Bott, 1959](#)). These equations
299 | show the relationship between the orientation and the shape of the stress ellipsoid:

300

$$301 \quad \tan(\theta) = [n / (1 * m)] * [m^2 - (1 - n^2) * R'] \quad [\text{eq.1}]$$

$$302 \quad R' = (\sigma_z - \sigma_x) / (\sigma_y - \sigma_x) \quad [\text{eq.2}]$$

303

304 Where l , m and n are the direction cosines of the normal to the fault plane, θ is the pitch
305 of the striation and R' is the shape of the stress ellipsoid obtained in an orthonormal
306 coordinate system, x , y , z . In this system, σ_y is the maximum horizontal stress, σ_x is the
307 minimum horizontal stress axis and σ_z is the vertical stress axis.

308

309 *3.2 The Right-Dihedral Model for Paleostrain Analysis*

310 The Right-Dihedral (RD) is a semi-quantitative method based on the overlapping of
311 compressional and extensional zones by using a stereographic plot. The final plot is an
312 interferogram figure, which usually ~~defined~~defines the strain-regime. This method is
313 strongly robust for conjugate fault sets and with different dip values for a same tensor.

314 The RD was originally defined by Pegoraro (1972) and Angelier and Mechler (1977), as
315 a geometric method, adjusting the measured fault-slip data (slickensides) in agreement
316 with theoretical models for extension and compressive fault-slip. Therefore, we can
317 constraint the regions of maximum compression and extension related to the strain
318 regime.

319

320 *3.3 The Slip Model for the Paleostrain Analysis*

321 The Slip Model (SM) is based on the Navier-Coulomb fracturing criteria (Reches,
322 1983), taking the Anderson model solution for this study (Anderson, 1951; Simpson,
323 1997). The Anderson model represents the geometry of the fault plane as monoclinic,
324 relating the quantitative parameters of the shape parameter (K') with the internal
325 frictional angle for rock mechanics (ϕ) (De Vicente 1988, Capote et al., 1991).

326 Moreover, this model is valid for neoformed faults, and some considerations have to be
327 accounted for previous faults and weakness planes present in the rock. These
328 considerations are related to the dip of normal and compressional faults, such as for

329 ~~compressional faulting dip values lower than 45° such as for compressional faulting~~
330 ~~values lower than $b < 45^\circ$~~ , reactivated as extensional faults. This model shows the
331 relationships between the K' , ϕ and the direction cosines for the striation on the fault
332 plane (De Vicente, 1988; Capote et al., 1991):

333

$$334 \quad K' = e_y / e_z \quad [eq.3]$$

335

336 Where e_z is the vertical strain axis, e_y is the maximum horizontal shortening and e_x is
337 the minimum horizontal shortening. This model assumes that there is no change of
338 volume during the deformation and $e_y = e_x + e_z$.

339 For isotropic solids, principal strain axes coincide with the principal stress axes. This
340 means that in this work, the orientation of the principal stress axis, S_{Hmax} is parallel to
341 the orientation of the principal strain axes, e_y , and hence, the minimum stress axis, S_{hmin} ,
342 is parallel to the minimum strain axis, e_x . This assumption allows us to estimate the
343 stress trajectories (S_{Hmax} and S_{hmin}) from the D_{e_y} SM results.

344 Resolving the equations of Anderson (~~Anderson, 1951~~) for different values (~~Anderson,~~
345 ~~1951~~), we can classify the tectonic regime that activates one fault from the measurement
346 of the fault dip, sense of dip (0° - 360°) and pitch of the slickenside, assuming that one of
347 the principal axes (e_x , e_y or e_z) ~~are-is~~ vertical (Angelier, 1984). We can classify ~~of~~ the
348 tectonic regime and represent the strain tensor by using the e_y and e_x orientation.

349

350 3.4 The K' strain diagram

351 Another analysis can be achieved by using the K' -strain diagram developed by Kaverina
352 et al. (1996) and codified in python-code by Álvarez-Gómez (2014). These authors have
353 developed a triangular representation based on the fault-slip, where tectonic patterns can

354 be discriminated between strike-slip and dip-slip types. This diagram is divided in 7
355 different zones according to the type of fault: (1) pure normal, (2) pure reverse and (3)
356 pure strike-slip; combined with the possibility of oblique faults: (4) reverse strike-slip
357 and (5) strike-slip with reverse component; and lateral faults: (6) normal strike-slip and
358 (7) strike-slip faults with normal component (**Fig. 3**). Strike-slip faults are defined by
359 small values for pitch ($p < 25^\circ$) and dips close to vertical planes ($\beta > 75^\circ$). High pitch
360 values ($p > 60^\circ$) are related to normal or/reverse fault-slip vectors. Extensional faults
361 show e_y in vertical whereas compressional faults show e_y in horizontal plane.

362 This method was originally performed for earthquake focal mechanism solutions by
363 using the focal parameters, the nodal planes (dip and strike) and rake ([Kaverina et al.,](#)
364 [1996](#)). The triangular graph is based on the equal-area representation of the T, N or B
365 and P axes in spherical coordinates (T tensile, N or B neutral and P pressure axes), and
366 the orthogonal regression between [earthquake magnitudes](#) M_s and m_b for the Harvard
367 earthquake CMT global catalogue in 1996. [Álvarez-Gómez \(2014\)](#) presented a code
368 python-based for computing the Kaverina diagrams, and we have modified the input
369 parameters by including the K' intervals for the strain field from the SM. The
370 relationship between the original diagram of Kaverina (**Fig. 3a**) and the K' -dip diagram
371 (**Fig. 3b**) that we have used in this work is shown in the figure 3. The advantage of this
372 diagram is the fast assignation of the type of fault and the tectonic regime that determine
373 this fault pattern, and the strain axes relationship.

374 Table 1 summarizes the different tectonic regimes of the figure 3b showing the
375 relationship with the strain main axes e_y , e_x and e_z . This diagram exhibits a great
376 advantage to classify the type of fault according to the strain tensor. Therefore, we can
377 assume the type of fault from the fault orientation affecting geological deposits for each
378 strain tensor obtained.

379

380 3.5 The Circular-Quadrant-Search (CQS) strategy for the paleostrain analysis

381 In this work, we propose a low-cost strategy based on a well-known methodology for
382 determining the stress/strain tensor affecting a ~~CCS-GSC~~ reservoir, which will allow ~~for~~
383 ~~the long-term~~ monitoring ~~long-term of the~~ geological and seismic behavior (Fig. 4). The
384 objective is to obtain enough structural data and spatially homogeneous of faults (Figs.
385 4, 5), for reconstructing the stress/strain tensor ~~by using the methodologies described~~
386 ~~above~~. The key-point is the determination of the orientation of the e_y , e_x and K' to plot
387 in a map and therefore, to establish the tectonic regime. We have chosen quadrants of
388 the circles with the aim to obtain a high-quality spatial distribution of point for the
389 interpretation of the local and very near strain field. Hence, data are homogeneously
390 distributed, instead of being only concentrated in one quadrant of the circle.

391 Pérez-López et al. (2018) carried out a first approach to the application of this
392 methodology at Hontomín, under the objective of the ENOS project (see next section
393 for further details). We propose a circular searching of structural field stations (Figs. 4,
394 5), located within a 20 km radius. This circle was taken, given that active faults with the
395 capacity of triggering earthquakes of magnitudes close to M 6, exhibits a surface rupture
396 of tens of kilometers, according to the empirical models (Wells and Coppersmith,
397 1994). Moreover, Verdon et al. (2015) pointed out that the maximum distance of
398 induced earthquakes for fluid injection is 20 km. Larger distances could not be related
399 to the stress/strain regime within the reservoir, except for the case of large geological
400 structures (folds, master faults, etc.). Microseismicity in ~~CCS-GSC~~ reservoir is mainly
401 related to the operations during the injection/depletion stages and long-term storage
402 (Verdon 2014, ~~Verdon~~; Verdon et al., 2015, ~~;~~ McNamara, 2016).

403 The presence of master faults (capable to trigger earthquakes of magnitude = or > than 6
404 and 5 km long segment) inside the 20 km radius circle, implicates that the regional

405 | tectonic field ~~is relevant for the reservoir geodynamics, being responsible for~~determines
406 | the strain accumulation in kilometric fault-sized. Furthermore, the presence of master
407 | faults could increase the occurrence of micro-earthquakes, due to the presence of
408 | secondary faults prone to trigger earthquakes by their normal seismic cycle (Scholz,
409 | 2018). Bearing in mind that CCS-GSC onshore reservoirs use to be deep saline aquifers
410 | (e.g. Bentham and Kirby, 2005), as the Hontomín ~~is case~~ (Gastine et al., 2017, Le Gallo
411 | and de Dios, 2018), ~~and be related to~~which is confined in folding-folded and fractured
412 | deep geological structures, in which local tectonics plays a key role in micro-seismicity
413 | and the possibility of CO₂ leakage.

414 | ~~The constraints of this strategy are related to the absence of kinematics indicators on~~
415 | ~~fault planes. It could occur due to later overlapping geological processes as neoformed~~
416 | ~~mineralization. Also, a low rigidness eludes the slicken fiber formation, and no~~
417 | ~~kinematic data will be marked on the fault plane.~~~~The constraints of this strategy are~~
418 | ~~related to the absence of kinematics indicators on fault planes, due to the geomechanical~~
419 | ~~property of the lithology involved or the erase by later geological processes as~~
420 | ~~neoformed mineralization, etc.~~ A poor spatial distribution of the outcrops was also taken
421 | into account for constraining the strategy. The age of sediments does not represent the
422 | age of the active deformations and hence, the active deformation has to be analyzed by
423 | performing alternative methods (i.e. paleoseismology, archaeoseismology).

424

425 | 4. RESULTS

426 | 4.1 Strain Field Analysis

427 | We have collected 447 fault-slip data on fault planes in 32 outcrops, located within a 20
428 | km radius circle centered at the HPP (**Fig. 5**). The age of the ~~structural-field~~
429 | ~~stations~~outcrops ranges between Early Triassic to present-day post-Miocene and are

430 mainly located in Cretaceous limestones and dolostones (Fig. 5, Table 2). However,
431 ~~No~~ Jurassic outcrops were located, and only seven stations are located on Neogene
432 sediments, ranging between Early Oligocene to Middle-Late Miocene. The ~~short-small~~
433 number of Neogene stations is due to the mechanical properties of the affected
434 sediments, mainly poor-lithified marls and soft-detrital fluvial deposits. Despite that, all
435 the Neogene stations exhibit high-quality data with a number of fault-slip data ranging
436 between 7 and 8, enough for a minimum quality analysis.

437 We have labeled the outcrops with the acronym HTM followed by a number (see figure
438 5 for the geographical location and Table 2 and figure 6 for the fault data). The station
439 with the highest number of faults measured is HTM17 with ~~107–105~~ faults on
440 Cretaceous limestone. ~~Nevertheless, we have removed the HTM17 to the analysis due~~
441 ~~to the high number of measurements, including lot of noise that could disturb the whole~~
442 ~~analysis.~~ Conjugate fault systems can be recognized in most of the stations (HTM1, 3,
443 5, 7, 10, 14, 16, 21, 23, ~~2524~~, ~~2625~~, 29, 30 and 32, Fig. 6), although there are a few
444 stations with only one well defined fault set (6, 22, 32). We have to bear in mind that
445 the recording of conjugate fault systems ~~are-is~~ more robust for the brittle analysis than
446 recording isolated fault sets, better constraining the solution (Žaholar and Vrabc,
447 2008). In total, 29 of 32 stations were used (HTM24, 27, 28 with no quality data), and
448 from these 29 stations, ~~24–21~~ were analyzed with the paleostrain technique. Solutions
449 obtained here are robust to establish the paleostrain field in each outcrop as the
450 orientation of the e_y , S_{Hmax} (Figs. ~~7, and 8~~).

451 The results obtained from the application of the paleostrain method have been expressed
452 in stereogram, right dihedral (RD), slip method (SM) and K' - diagram (Fig. 7). The K' -
453 diagram shows the fault classification as normal faults, normal with strike-slip
454 component, pure strike-slip, strike-slip with reverse component and reverse faults (see

455 **Fig. 3).** Main faults are lateral strike-slips and normal faults, followed by reverse faults,
456 strike-slips and oblique strike-slips faults. The results of the strain regime are as
457 follows: 1) 43% of extensional with shear component; 2) 22% of shear; 3) 13% of
458 compressive strain (lower Cretaceous and early-middle Miocene, **Table 2**); 4) 13% of
459 pure shear and 5) 9% of shear with compression strain field, although with the presence
460 of five reverse faults.

461 ~~On the other hand~~**In contrast**, we can observe that there are solutions with a double
462 value for the e_y , S_{Hmax} orientation: HTM1, 2, 10, 11, 13, 15, 19, 26, and 30. The stations
463 HTM3 and 23 (upper Cretaceous), show the best solution for strike-slip strain field as a
464 pure strike-slip regime and e_y with N25°E and N99°E trend, respectively (**Fig. 7**).

465 It is easy to observe the agreement between the e_y results from the SM and the K'- strain
466 diagram, for instance, in the HTM-2 the K'-diagram indicates strike-slip faults with
467 reverse component for low dips ($0^\circ < \beta < 40^\circ$), but also indicates strike-slip faults with
468 normal component for larger dips ($40^\circ < \beta < 90^\circ$). However, both results are in
469 agreement with a strain field defined by the orientation for e_y , S_{Hmax} with $N150^\circ \pm 18^\circ$
470 trend. This tectonic field affects Cretaceous carbonates and coincides with the regional
471 tectonic field proposed by [Herraiz et al. \(2000\)](#), ~~[Stich et al. \(2006\)](#)~~, [Tavani et al. \(2011\)](#)
472 and [Alcalde et al. \(2014\)](#).

473 ~~Two e_y , S_{Hmax} directions can be considered, N150°E and N50°E. We obtained an~~
474 ~~averaged value of N105°E by mixing both values of trend. However, a large number of~~
475 ~~measured faults and their uncertainties slightly disturb the results (Table 2).~~

476

477 4.2 Late Triassic *Outcrop* Paleostrain

478 Strain analysis from HTM5 fault set shows e_y with NW-SE trending and shear regime
479 with extension defined by strike-slip faults (**Figs. 7a and 8**). This is in agreement with

480 | the uniaxial extension described in Tavani (2012), ~~author that~~ constraining this regime
481 | with S_{hmin} with NE-SW trending.

482

483 | 4.3 Cretaceous Outcrops Paleostrain

484 | We have divided this result in two groups, (a) outcrops within the 20km circle from
485 | HPP and (b) the outcrop the HTM17 (Fig. 5), which is located in the HPP facilities and
486 | described in the next section. HTM-14 is the only outcrop from early-Early Cretaceous
487 | age, showing a compressive tectonic stage with reverse fault solutions, defined by e_y
488 | with NE-SW trending (Fig. **87b and 7c**). Taking into account the extensional stage
489 | related to the Main Rifting Stage that took place in Early Cretaceous times (i.e. Carola,
490 | 2004; Tavani, 2012; Tugend et al., 2014) ~~during this age~~, we interpreted these results as
491 | a modern strain field, probably related to the Cenozoic Inversion stage. ~~A local~~
492 | ~~compressive stage was discarded due to the absence of compressive structures related to~~
493 | ~~this age in the area and surroundings.~~

494 | Outcrops HTM 2, 3, 8, 17, 19, 20, 21, 22, 23, 25, 26, 29, 31 and 32 are from the upper
495 | Cretaceous carbonates, ~~and four main strain fields are described, depending on the fault~~
496 | ~~sets (Fig. 87).~~ Results are: (1) a compressive stage featured by e_y with NW-SE trending,
497 | similar to ~~those the~~ stage described in Tavani (2012), and (2) a normal strain stage with
498 | e_y striking both E-W and NE-SW (Fig. **87**, HTM 20, 21, 31 and 32). Finally, a (3) ~~a~~
499 | shear stage (activated strike-slip faults) and (4) a shear with ~~an~~ extension (strike-slip
500 | with normal component) were described as well. These two late stages are featured by
501 | e_y with NE-SW and NW-SE trends. The existence of four different strain fields is
502 | determined by different ages during the Cretaceous and different spatial locations in
503 | relation to the main structures, the Ubierna Fault System, Hontomín Fault, Cantabrian
504 | Thrust, Montorio folded band and the ~~anticline~~ Polientes syncline (Fig. **81**).

505
506
507
508
509
510
511
512
513
514
515
516
517
518
519
520
521
522
523

4.4 Cretaceous Outcrop HTM17 on the Hontomín Pilot Plant

This outcrop is located on top of the geological reservoir, in a quarry of Upper Cretaceous limestones. The main advantage of this outcrop is the well-development of striation and carbonate microfibers which yields high-quality data. 105 fault-slip data were measured, with the main orientation striking N75°E; N-50°E; and a conjugate set with N130°E (±10°) trend (Fig. 8). The result of the strain inversion technique shows an extensional field featured by an ey trajectory striking N107°E (±24°) related to an extensional strain field (see the K' diagram in figure 8). Most of the faults are extensional faults (Fig. 9) oriented NE-SW and NW-SE oriented (Fig. 9), in agreement with the extensional RD solution. Reverse faults are oriented NNE-SSW, E-W and WNW-ESE. The advantage of this outcrop is the geographical and stratigraphic position. It is located on top of the HPP facilities in younger sediments than the ~~host rocks for storage~~ reservoir rocks. Furthermore, ~~as given that the Jurassic host~~ reservoir rock and the Cretaceous upper unit are both composed by carbonates, the fault pattern measured here could be a reflex of the fracture network affecting the Jurassic storage rocks in depth (see Figs. 2, 9).

Con formato: Fuente: Cursiva

4.4.5 Cenozoic outcrops strain field

The Cenozoic tectonic inversion was widely described in the area by different authors (e.g. Carola, 2004; Tavani, 2012; Tungend et al., 2014). This tectonic inversion is related to compressive structures, activating NW-SE and NE-SW thrusts with NW-SE and NNE-SSW e_y trends, respectively. The Ubierna Fault has been inverted with a right-lateral transpressive kinematics during the Cenozoic (Tavani et al., 2011). Early

530 Oligocene outcrop (HTM13, **Figs. 7c and 8**) shows a local extensional field with e_y
531 with NNE-SSW and N150°E trending. During the Lower-Middle Miocene,
532 HTM15 and HTM30 outcrops exhibit the same e_y striking trend, but for a compressive
533 tectonic stage regime (**Figs. 7e and 8**). In addition, during the middle Miocene, an
534 extensional tectonic strain is described and characterized by NNE-SSW and NE-SW
535 trends. HTM1 shows extensional tectonics with e_y oriented N50°E and N130°E.
536 Summarizing, the Cenozoic inversion and tectonic compression are detected during the
537 early Early to middle Middle Miocene, later to and the Oligocene. However, but during
538 the middle Miocene, only one extensional stage was interpreted (HTM1, Fig. 7c).
539 The outcrops located closer to the HPP (HTM 17, 31, 32, **Figs. 5 and 7**), show E-W
540 faults. HTM05 is located on the Ubierna Fault, showing a NW-SE trend, whilst HTM03
541 shows strike-slip NE-SW strike-slip. Moreover, this station is located within a valley
542 with the same orientation and surrounding faults have the same orientation (Fig. 5).
543 Close to the HPP facilities, E-W faults are measured. This fault set was activated under
544 a strain field defined by e_y with E-W trending and K' diagram shows normal faults with
545 strike-slip component. However, the present day e_y with a roughly N-S trend (Herraiz et
546 al., 2000, Stich et al., 2006), could active E-W faults as reverse faults and hence, more
547 energy would needed to move like seismic sources. In addition, fault dip data obtained
548 from structural analysis can be included in geomechanical analysis of fault rupture.
549 Strain analysis suggests that the planes parallel to the S_{Hmax} orientation (NNW-SSE and
550 N-S), that could affect induce the leakage into the reservoir would be those planes
551 parallel to the S_{Hmax} orientation, that is, NNW-SSE and N-S (Fig. 7). Moreover, N50°E
552 S_{Hmax} orientation could also affect the reservoir. HPP facilities are close to the
553 Hontomin Fault (Fig. 5), a WNW-ESE oriented fault, although the HTM17 station
554 shows that N-S fault planes could play an important role for seepage of fluid into the

Con formato: Subíndice

555 ~~reservoir. HPP facilities are close to WNW-ESE fault although the HTM17 station~~
556 ~~shows that N-S fault planes could play an important role for seepage fluid into the~~
557 ~~reservoir.~~

558

559 5. DISCUSSION

560 *5.1. Mesozoic—Cenozoic Paleostrain evolution*

561 ~~We propose a tectonic field evolution for the Hontomín CCS area, from the Triassic to~~
562 ~~Neogene times (Fig. 9), based on the results obtained from the paleostrain analysis (Fig.~~
563 ~~8). Furthermore, the data used in this work were completed from available bibliographic~~
564 ~~data of paleostress and paleostrain affecting the Burgalesa Platform (see references in~~
565 ~~Fig. 9) and large-scale tectonic events.~~

566 ~~Triassic age is featured by a uniaxial extension determined by a paleostrain field with e_x~~
567 ~~striking NE-SW (Tavani, 2012). The oldest tectonic strain field that we have obtained,~~
568 ~~recorded during the Late Triassic, is represented by a strike-slip tectonic field with shear~~
569 ~~component (Figs 7a, 8 and 9), which we have related with the break-up of Pangaea. In~~
570 ~~this stage, NE-SW right lateral faults are dominant.~~

571 ~~No Jurassic outcrops are in the studied area and hence, the Jurassic deformation~~
572 ~~assumed in this work comes from Tavani (2012), suggesting the aperture of the Bay of~~
573 ~~Biscay in a large-scale N-S extension. Alcalá et al. (2014) pointed out a tectonic~~
574 ~~evolution from Lias diparism (Early Jurassic) and N-S tectonic extension, activating E-~~
575 ~~W extensional faults. Moreover, Vegas et al. (2016) interpreted a rift extension during~~
576 ~~this period.~~

577 ~~The Early Cretaceous tectonic field shows a e_y with NE-SW trend, determining a~~
578 ~~compressive and convergence local stage (Figs 7a, 8). However, we have assumed this~~
579 ~~strain field as modern, probably during the Cenozoic inversion, overlapping the~~

580 extensional regional paleostrain (Fig. 9, red with white circles). The Upper Cretaceous
 581 tectonic strain is defined by several e_y trends, from an initial N-S and NE-SW, to NW-
 582 SE in a final transtensional state, which is in agreement with Soto et al. (2011), being
 583 active even during the Early Oligocene.

584 The tectonic convergence represented by a NE-trending S_{Hmax} , determining a reverse
 585 field to have taken place during the Early Miocene, although Tavani (2012) pointed out
 586 that the Cenozoic tectonic inversion could start at the Upper Cretaceous. During the
 587 Miocene, normal faults with shear during this period (Fig. 9) could be interpreted as
 588 folding fractures. In this case, extensional faulting could appear in the upper part of
 589 anticlines formed by bending. The middle Miocene is interpreted as an extensional stage
 590 with normal strain field.

591 Finally, the active strain field (Miocene-Present day), shows a local compressional field
 592 with N50°E trending e_y , S_{Hmax} with and the regional field with N150°E trending e_y ,
 593 S_{Hmax} . The active regional field proposed by Herraiz et al. (2000), Stich et al. (2006),
 594 Tavani et al. (2011) and Alcalde et al. (2014), shows e_y , S_{Hmax} with almost NNW-SSE
 595 and N-S trends.

597 ~~5.2 Active faulting in the surrounding of HPP~~

598 5.1 Regional active stress tensor in HTM17 fault pattern

599 The active regional field proposed by Herraiz et al. (2000), Stich et al. (2006), Tavani et
 600 al. (2011) and Alcalde et al. (2014), shows e_y , S_{Hmax} with almost NNW-SSE and N-S
 601 trends. Namely, the work from Herraiz et al. (2000) calculates three stress tensors
 602 within the 20 km of our study area and a Quaternary ~~onestress~~ stress tensor close to the area
 603 (c.a. 40 km southward of Hontomín). The age of the first one is Miocene, and defined
 604 by σ_1 87°/331°; σ_2 01°/151°; σ_3 00°/061° (dip/dip sense 0°-360°), with an R=0.06 and

Con formato: Fuente: Cursiva

Con formato: Fuente: Cursiva

Con formato: Fuente: Cursiva

Con formato: Fuente: Cursiva

Con formato: Fuente: Symbol

Con formato: Subíndice

Con formato: Fuente: Symbol

Con formato: Subíndice

Con formato: Fuente: Symbol

Con formato: Subíndice

Con formato: Sin Resaltar

605 S_{Hmax} trending N151°E, under an extensional tectonic regime. Two post-Miocene stress
 606 tensors are defined by: (1) σ_1 87°/299°; σ_2 00°/209°; σ_3 01°/119° with R = 0.13, S_{Hmax}
 607 with N29°E trend under an extensional tectonic regime and (2) σ_1 00°/061°; σ_2
 608 86°/152°; σ_3 03°/331°, with R=0.76, and S_{Hmax} N62°E under strike-slip tectonic regime.
 609 Finally, these authors calculated a Quaternary stress tensor defined by: σ_1 85°/183°; σ_2
 610 02°/273°; σ_3 03°/003°; R=0.02 and S_{Hmax} with N101°E trend under an extensional
 611 tectonic regime. The regional active stress tensor defined for Pliocene-Quaternary ages
 612 is σ_1 88°/197°; σ_2 01°/355°; σ_3 00°/085° for 327 data with R = 0.5 and S_{Hmax} with N-S
 613 trend under an extensional tectonic regional regime.
 614 We have applied the regional active stress tensor (Herraiz et al., 2000) for studying the
 615 reactivation of previous fault patterns measured in HTM17 (Figs. 8 and 9). To de
 616 thascarry out this study, we assume that the fault plane reactivation depends on σ_1 and
 617 σ_3 , and the shape of the failure envelope. Therefore, we have used the Mohr-Coulomb
 618 failure criteria for preexisting fault planes (Xu et al., 2010; Labuz and Zang, 2012), by
 619 using the Mohr Plotter v3.0 code (Allmendinger, 2012). Moreover, to calculate the
 620 Mohr-Coulomb circle, it is necessary to know the cohesion and friction parameters of
 621 the host rock of the reservoir rock. Bearing in mind that the reservoir rocks are Lower-
 622 Jurassic carbonates (dolostone and oolitic limestone, Alcalde et al., 2013, 2014; Ogaya
 623 et al., 2013), we have assumed the averaged cohesion for carbonates (limestone and
 624 dolostone) in 35° and the coefficient of internal friction of 0.7 (Goodman, 1989). In
 625 addition, we have assumed no cohesion with an angle of static friction of 0.7 for
 626 preexisting faults.
 627 Figure 10 shows the main results for the Mohr analysis. The reactivated planes under
 628 the active-present stress field are red dots, 52 out of the original 1+05 fault-slip
 629 measurements at HTM17. Green and orange dots indicate faults with no tectonic

Con formato: Subíndice

Con formato: Subíndice

Con formato: Sin Superíndice / Subíndice

Con formato: Sin Resaltar

Con formato: Sin Superíndice / Subíndice

Con formato: Fuente: Symbol

Con formato: Subíndice

Con formato: Fuente: Symbol

Con formato: Subíndice

Con formato: Sin Resaltar

Con formato: Sin Resaltar

630 strength accumulation under the present-day stress field. Reactivated fault sets are
631 oriented between N to N60°E and N115° to 180°E, with N-S and NNE-SSW as main
632 trends (Fig. 10, red rose diagram). Under an extensional tectonic field with $R = 0.5$, N-S
633 are normal faults, whereas NNE-SSW and NNW-SSE trends are strike-slips faults with
634 extensional component. According to the results shown in figure 10, these faults could
635 be reactivated without a pore pressure increase. The inactive fault orientation is
636 constrained between N60°E and N115°E, mainly WNW-ESE (Fig. 10, green rose
637 diagram). Regarding the uncertainties of these fault orientations, these values can
638 oscillate $\pm 5^\circ$, according to the field error measurement (averaged error for measuring
639 structures by a compass).

640 Concerning the reliability of the results, some constrains need to be explained. The
641 Mohr-Coulomb failure criterion is an approximation that assumes that the normal stress
642 on the fault plane is not tensile. Furthermore, the increasing of pore pressure in the
643 storage reservoir rock reduces the normal stress on the plane of failure and the interval of
644 fault reactivation could be higher. This effect was not considered in the previous
645 analysis since the calculation of the critical pore pressure was out of the focus beyond
646 the purpose of this work. Nevertheless, the MohrPlotter software (Allmendinger, 2012),
647 allows estimating the increase of pore pressure to the critical value under some
648 conditions.

649 Finally, we have applied the Slip Model and Right Dihedral to the reactivated fault-slip
650 data from HTM17 outcrop (Fig. 11), by including the rake estimated from the active
651 regional stress tensor determined by (Herraiz et al., (2000). At a glance, faults oriented
652 between N10°E and N10°W act as normal faults (4 out 52, Figs. 11a, c), faults between
653 N10°E - N50°E, and N10°W - N50°W act as extensional faults with strike-slip
654 component (31 out 52), and NE-SW and NW-SE vertical faults act as pure strike slips

Con formato: Fuente: Negrita

Con formato: Fuente: Negrita

655 [\(8 out 52\). The Right Dihedral shows a tectonic regime of strike-slip with extensional](#)
656 [component \(see De Vicente et al., 1992\), with orthorhombic symmetry and \$S_{Hmax}\$](#)
657 [oriented N10°W, which is in agreement with the stress-tensor proposed by Herraiz et al.](#)
658 [\(2000\) with \$\sigma_2 = 01^\circ/355^\circ\$ and \$\sigma_1\$ vertical. However, strain analysis in this case shows](#)
659 [a strike-slip extensional tectonic regime, instead of the extensional regime derived from](#)
660 [the stress field. Despite this, both the Mohr-Coulomb analysis and the Paleostrain](#)
661 [analysis \(SM and RD\), suggest N-S normal faulting, NNE-SSW to NE-SW and NNW-](#)
662 [SSE to NW-SE strike-slips as the active fault network affecting the reservoir. De](#)
663 [Vicente et al. \(1992\) pointed out that the SM analysis is more robust applied in fault-](#)
664 [slip data classified previously by other techniques. Here, we have used the Mohr](#)
665 [Coulomb failure criteria to separate active fault set under the same strain tensor,](#)
666 [yielding robustness to the results from SM and RD analysis.](#)

667

668

669 [5.2 Active faulting in the surrounding of HPP](#)

670 Quaternary tectonic markers for the UFS are suggested by Tavani et al. (2011).
671 According to the tectonic behavior of this fault as right-lateral strike-slip, and the fault
672 segments proposed by Tavani et al. (2011), ranging between 12 and 14 km long, the
673 question is whether this fault could trigger significant earthquakes and which could be
674 the maximum associated magnitude. This is a relevant question given that the “natural
675 seismicity” in the vicinity could affect the integrity of the caprock. Bearing in mind the
676 expectable long-life for the reservoir, estimated in thousands of years, the potential
677 natural earthquake that this master fault could trigger has to be estimated. In this sense,
678 it is necessary to depict seismic scenarios related to large earthquake triggering;
679 however, this type of analysis is beyond the focus of this work.

680 The income information that we have to manage in the area of influence (20 km) is: (a)
681 the instrumental seismicity, (b) the geometry of the fault, (c) the total surface rupture,
682 (d) the upper crust thickness and (e) the heat flow across the lithosphere. Starting for the
683 heat flow value, the Hontomín wells show a value that lies between 62 and 78 mW/m²
684 at a 1,500 m depth approximately (Fernández et al., 1998). Regarding the Moho depth
685 in the area, these aforementioned authors obtained a value ranging between 36 and 40
686 km depth, while the lithosphere base ranges between 120 and 130 km depth (Torre et
687 al., 2015). The relevance of this value is the study of the thermal weakness into the
688 lithosphere that could nucleate earthquakes in intraplate areas (Holford et al., 2011). For
689 these authors, the comparison between the crustal heat-flow in particular zones, in
690 contrast with the background regional value, could explain large seismicity and high
691 rates of small earthquakes occurrence, as the case of the New Madrid seismic zone
692 (Landgraf et al., 2018). For example, in Australia heat-flow values as much as 90
693 mW/m² are related with earthquakes sized M > 5 (Holford et al., 2011).
694 Regarding the maximum expected earthquake into the zone, we have applied the
695 empirical relationships obtained by Wells and Coppersmith (1994). We have used the
696 equations for strike-slip earthquakes according to the strain field obtained in the area
697 (pure shear), and the surface rupture segment for the Ubierna Fault System, assuming a
698 surface rupture segments between 12 and 14 km (Tavani et al., 2011). The obtained
699 results show that the maximum expected earthquake ranges between M 6.0 and M 6.1.
700 Wells and Coppersmith (1994) indicate for these fault parameters a total area rupture
701 ranging between 140 and 150 km². Surface fault traces rupture as lower as 7 km needs
702 at least 20 km of depth in order to reach a value of the fault-area rupturing greater than
703 100 km², in line with a Moho between 36 and 40 in depth.

704 Regarding the instrumental earthquakes recorded into the area, the two largest
705 earthquakes recorded correspond to magnitude M 3.4 and M 3.3, with a depth ranging
706 between 8 and 11 km, respectively, and a felt macroseismic intensity of III (EMS98,
707 www.ign.es, last access on May, 2019). Both earthquakes occurred between 50 and 60
708 km of distance from the Hontomín Pilot Plant. Only five earthquakes have been
709 recorded within the 20-km radius area of influence and with small magnitudes ranging
710 between M 1.5 and M 2.3. The interesting data is the depth of these earthquakes,
711 ranging between 10 and 20 km, which suggest that the seismogenic crust could reach 20
712 km of depth.

713 ~~Furthermore, if E-W sets act as extensional faults in this regional tectonic context, it~~
714 ~~would be related to the upper part of the no-deformational compressive zone and reverse~~
715 ~~earthquakes would appear with the foci located deeper than 2 km. The strain field is~~
716 ~~directly related to the permeability tensor due to rock dissolution. Hence, this value~~
717 ~~could play an important role for long term reservoir expected life.~~

718

719 5.3 Local tectonic field and ~~Induced-induced~~ *Seismicityseismicity*

720 The fluid injection into a deep saline aquifer, which is used as ~~CCSGSC~~, generally
721 increases the pore pressure. The increasing of the pore pressure migrates from the point
722 of injection to the whole reservoir. Moreover, changes into the stress field for faults that
723 are located below the reservoir, could also trigger induced earthquakes (Verdon et al.,
724 2014). Nevertheless, to understand this possibility and the study the volumetric strain
725 field spatial distribution is required (Lisle et al., 2009).

726 ~~We have applied a physic model to estimate the total volume injected (room~~
727 ~~conditions), and then we have applied the McGarr's (2014) approximation.~~ The
728 injection of 10 k tons of CO₂ in Hontomín (Gastine et al., 2017), represents an

729 approximated injected volume of CO₂ of 5.56 x 10⁶ m³ (room conditions). We have used
730 the expression Mo(max) (Nm) = G · ΔV (McGarr 2014, eq. 13), where G is the modulus
731 of rigidity and for the upper limit is 3 x 10¹⁰ Pa, and ΔV is 5.56 x 10³ m³ for the total
732 injected volume (in room conditions). The result is Mo(max) equal to 1.67 x 10¹⁷ Nm
733 (Joules), which corresponds to a maximum seismic moment magnitude $M_o(max) - w$
734 $(max) = 65.345$, of the maximum Richter magnitude by applying the equation $M_w =$
735 $(\text{Log } E_{Mo(max)} = 11.8 + 1.5 M - 9.05)/1.5$ from Hanks and Kanamori (1979); where
736 Log is the logarithm to the base 10, E is the seismic released energy in Joules, and M
737 the Richter magnitude. McGarr (2014) applied this approach for three cases: (1)
738 wastewater injection, (2) hydraulic fracturing, and (3) geothermal injection. We propose
739 to include this approach for fluid injection related to geological storage of CO₂. We
740 assume that the pore pressure increases from CO₂ injection in a similar way that
741 wastewater does (originally defined by Frohlich, 2012). According to McGarr (2014),
742 the utility of the analysis that we have performed is “to predict in advance of a planned
743 injection whether there will be induced seismicity”, and in the case of the Hontomín
744 Pilot Plant HPP, by the estimation to estimate of the “total injected volume” in a small-
745 scale injection plant. Therefore, the earthquake magnitude to this fluid-injected
746 volume according to the McGarr (2014) and Verdon et al. (2014) could be M > 5 if
747 there are faults with a minimum size of 104 km and oriented according to the present-
748 day stress field within the influence area (N-S extensional faults and NNE-SSW/NNW-
749 SSE strike slip faults; Fig. 10). In the case of HPP, there are faults below the reservoir
750 with this potential earthquake triggering (Alcalde et al., 2014). Also according to
751 McGarr (2014), this value has not to be considered as an absolute physic limit
752 instead but as of a qualitative approximation. Alternatively on the other hand,
753 overpressure increasing the permeability increasing by overpressure of the carbonate

Con formato: Fuente: Symbol

Con formato: Superíndice

Con formato: Fuente: Symbol

Con formato: Superíndice

Con formato: Superíndice

Con formato: Superíndice

Con formato: Subíndice

Con formato: Subíndice

Con formato: Fuente: Negrita

754 | reservoir along with the pore pressure variations of about 0.5 MPa, could trigger
755 | earthquakes, as well. Stress-drop related to fluid injections are also reported (Huang et
756 | al., 2016).

757 | Le Gallo and de Dios (2018) described two main fault sets affecting the reservoir with
758 | N-S and E-W trend, respectively. According to the present-day stress tensor described
759 | by Herraiz et al. (2000) and Tavani et al. (2011), E-W fault-sets are accommodating
760 | horizontal shortening, which means that the permeability could be low, ~~and~~. Besides,
761 | ~~these faults are decoupled from the present-day stress tensor. However,~~ N-S faults
762 | could act as ~~strike-slip with trans-tensional component~~ normal faults and, hence, with
763 | higher permeability. ~~On the other hand, increasing the pore pressure of E-W faults~~
764 | ~~could reduce seismic cycle in these faults. Therefore, special attention has to be paid~~
765 | ~~in microseismicity related to E-W faults.~~ In this sense, the study of focal mechanisms
766 | solutions could improve the safety management, even for microearthquakes of
767 | magnitude lesser than M 3.

768 | Moreover, the CO₂ lateral diffusion and pressure variation change during the fluid
769 | injection phase, and then the system would relax before to be increased during the next
770 | injection phase. In this context, the intermittent and episodic injection of CO₂ could also
771 | trigger earthquakes by the stress-field and fluid pressure variations in short time periods.

772

773 | 6. CONCLUSIONS

774 | The application of the analysis for brittle deformation determines the tectonic evolution
775 | of the strain field, applied in ~~Carbon Capture and Sequestration~~ Geological Carbon
776 | Storage (CCSGSC). The possibility that pore pressure variations due to fluid injection
777 | could change the stress/strain conditions in the reservoir's caprock, makes the study of
778 | the present-day tectonic field as mandatory for the storage safety operations. In this

779 sense, we have to bear in mind that this kind of subsurface storage is designed for long-
780 life expectancy, about thousands of years, and therefore, relevant earthquakes could
781 occur affecting the sealing and the seepage of CO₂, compromising the integrity of the
782 reservoir. Hence, we can conclude from our analysis the following items:

783 (1) The study of this tectonic field allows classifying the geometry of the faults to
784 prevent prone earthquake-related structures and design monitoring seismic network.

785 (2) The influence area around the facilities of the ~~ECS-GSC~~ for studying the active
786 stress/strain field could reach 20 km from the facility and the tectonic evolution of the
787 geological history of the reservoir have to be established, adding missing information
788 from map scale and boreholes. This information could be used from the 3D local
789 fracture pattern estimation to avoid ~~the pore overpressure, for increasing the~~
790 ~~permeability paths~~. Analysis of the stress-drop due to the fluid injection could be
791 combined with this information to understand potential microseismicity associated with
792 the injection operations.

793 (3) In the case of Hontomín Pilot-Plant, we have obtained two strain active tectonic
794 fields featured as shear deformation. These fields are defined by (a) a local tectonic
795 strain field with e_y , S_{Hmax} striking N50°E and (b) the regional one defined by e_y , S_{Hmax}
796 with N150°E trend. In this context, strike-slip faults with N-S, NNE-SSW and NNW-
797 SSE trends, ~~reverse faults with NW-SE trend and reverse oblique faults oriented E-W,~~
798 are accumulating present-day tectonic deformation. Analysis of Mohr-Coulomb failure
799 criterion shows a potential reactivation of these fault sets. ~~Therefore, we propose the~~
800 ~~monitoring of E-W faults and the intersection with strike-slip faults, either due to the~~
801 ~~possibility to make high permeable paths for CO₂ mobility, or due to the possibility to~~
802 ~~act as compressional faulting due to the increasing of the pore pressure during injection.~~

803 | (4) ~~Both WNW-ESE fault plus N-S and NE-SW directions~~faults are accumulating
804 tectonic deformation and they could act as normal faults. This means that this fault set
805 are-is the preferential ~~fault-directions~~ for potential fluid leakage. ~~E-W could act as~~
806 ~~compressive faults.~~In addition, intersection with NNE-SSW and NNW-SSE could
807 arrange 3D networks for fluid mobilization and leakage.

808 (5) The Ubierna Fault System represents a tectonically active fault array that could
809 trigger natural earthquakes as large as M 6 (± 0.1), from the empirical relationship of the
810 total rupture segment (ranging between 12 and 14 km, and the total fault-area rupture,
811 oscillating between 100 and 150 km²). Despite the lack of instrumental seismicity into
812 the influence area, we cannot obviate the potential earthquake occurrence within
813 intraplate areas due to the long- timescale expected-life of the ~~EESSGSC~~. The heat-flow
814 values and thermal crust conditions could determine the presence of intraplate
815 earthquakes with magnitude $M > 5$, for a long timescale (thousands of years).

816 The tectonic evolution and kinematics of the west part of the Burgalesa Platform
817 domain from upper Triassic to present day show a Cretaceous tectonic inversion, local
818 reverse strain field during the early Oligocene and early Miocene, with a Normal strain
819 field during the middle Miocene. The active strain field is now defined by ~~aan shear~~
820 extensional tectonic defined by e_y with N-S trend, activating ~~EN-W-S thrust-normal~~
821 faults and right-lateral faults with ~~WNNW-~~ and ~~NWNNE-~~ trends.

822 Finally, we state that the determination of the active tectonic strain field, the recognition
823 and study of active faults within the area of influence (20 km), the estimation of the
824 maximum potential triggered natural earthquake, the modeling of the stress-change
825 during the fluid injection and stress-drop, probably improve the operations for a secure
826 storage. In a short future, earthquake scenarios will be the next step: modeling the

827 Coulomb static stress-changes due to fluid injection and the modeling of intensity maps
828 of horizontal seismic acceleration.
829

830 ACKNOWLEDGEMENTS

831 Thanks are given to Pr. Graham Yielding and an anonymous reviewer for their remarks
832 during the open discussion. We wish to thank Pr. Allmendinger for the free use of the
833 MohrPlotter 3.0 software, last access in March of 2020 at the web browser:
834 <http://www.geo.cornell.edu/geology/faculty/RWA/programs/mohrplotter.html>. This
835 work has been partially supported by the European Project ENOS: ENabling Onshore
836 CO₂ Storage in Europe, H2020 Project ID: 653718 and the Spanish project 3GEO,
837 CGL2017-83931-C3-2-P, MICIU-FEDER. The authors would also thank the crew of
838 CIUDEN at Hontomín facilities for their kind assistance during our fieldwork.
839

840 REFERENCES

- 841 Alcalde, J., Martí, D., Calahorrano, A., Marzan, I., Ayarza, P., Carbonell, R., Juhlin, C.,
842 and Pérez-Estaún, A.: Active seismic characterization experiments of the Hontomín
843 research facility for geological storage of CO₂, Spain, *Int. J. Greenh. Gas Con.*, 19,
844 785–795, <http://dx.doi.org/10.1016/j.ijggc.2013.01.039>, 2013.
- 845 Alcalde J., Marzán I., Saura E., Martí D., Ayarza P., Juhlin C., Pérez-Estaún, A., and
846 Carbonell, R: 3D geological characterization of the Hontomín CO₂ storage site,
847 Spain: Multidisciplinary approach from seismic, well-log and regional data,
848 *Tectonophysics*, 627, 6–25, <http://dx.doi.org/10.1016/j.tecto.2014.04.025>, 2014.
- 849 Allmendinger, R. W., Cardozo, N. C., and Fisher, D.: *Structural Geology Algorithms:*
850 *Vectors & Tensors, Cambridge, England, Cambridge University Press, 289 pp, 2012.*
- 851 Álvarez-Gómez, J. A.: FMC: a one-liner python program to manage, classify and plot
852 focal mechanisms, EGU General Assembly, Vienna, Austria, 27 April-02 May,
853 EGU2014-10887, 2014.
- 854 Anderson, E. M.: *The Dynamics of Faulting and Dyke Formation with application to*
855 *Britain*, 2nd ed., Oliver and Boyd, Edinburgh, 206 pp., 1951.
- 856 Angelier, J.: Determination of the mean principal directions of stresses for a given fault
857 population, *Tectonophysics*, 56, 17-26, [https://doi.org/10.1016/0040-1951\(79\)90081-](https://doi.org/10.1016/0040-1951(79)90081-7)
858 [7](https://doi.org/10.1016/0040-1951(79)90081-7), 1979.
- 859 Angelier, J.: Tectonic analysis of fault slip data sets, *J. Geophys. Res.*, 89, 5835-5848,
860 <https://doi.org/10.1029/JB089iB07p05835>, 1984.
- 861 Angelier, J.: Inversion of field data in fault tectonics to obtain the regional stress-III. A
862 new rapid direct inversion method by analytical means, *Geophys. J. Int.*, 103, 363-
863 376, <https://doi.org/10.1111/j.1365-246X.1990.tb01777.x>, 1990.
- 864 Angelier, J. and Mechler, P.: Sur une méthode graphique de recherche des contraintes
865 principales également utilisable en tectonique et en séismologie: la méthode des
866 dièdres droits, *B. Soc. Geol. Fr.*, 19, 1309-1318,
867 <http://dx.doi.org/10.2113/gssgfbull.S7-XIX.6.1309>, 1977.
- 868 Aurell, M., Meléndez, G., Olóriz, F., Bádenas, B., Caracuel, J. E., García-Ramos, J. C.,
869 Goy, A., Linares, A., Quesada, S. and Robles, S.: Jurassic, in *The geology of Spain*,
870 pp. 213–253, The Geological Society of London., 2002.
- 871 Bentham, M. and Kirby, G.: CO₂ Storage in Saline Aquifers. *Oil Gas Sci. Technol.*, 60,
872 559-567, <https://doi.org/10.2516/ogst:2005038>, 2005.

Código de campo cambiado

- 873 Bott, M.H.P.: The mechanism of oblique-slip faulting, *Geol. Mag.*, 96: 109-117.
874 <https://doi.org/10.1017/S0016756800059987>, 1959.
- 875 Capote, R., De Vicente, G., and González Casado, J. M.: An application of the slip
876 model of brittle deformation to focal mechanism analysis in three different plate
877 tectonics situation. *Tectonophysics*, 191, 399-409, [https://doi.org/10.1016/0040-](https://doi.org/10.1016/0040-1951(91)90070-9)
878 1951(91)90070-9, 1991.
- 879 Calvet, F., Anglada, E. and Salvany, J. M.: El Triásico de los Pirineos, in Vera, J.A.
880 (ed.) *Geología de España*, pp. 272–274, SGE–IGME, Madrid, 2004.
- 881 Carola, E.: The transition between thin-to-thick-skinned styles of deformation in the
882 Western Pyrenean Belt. Ph.D. thesis, Universitat de Barcelona, 271 pp., 2004.
- 883 Christensen, N. P.: Report on the current state and need for further research on CO₂
884 capture and storage. CO2NET, European Carbon Dioxide Network,
885 www.co2net.com, 2004.
- 886 Chu, S.: Carbon Capture and Sequestration, *Science*, 325, 1599,
887 <http://dx.doi.org/10.1126/science.1181637>, 2009.
- 888 Dallmeyer, R. D. and Martínez-García, E., Eds.: *Pre-Mesozoic Geology of Iberia*,
889 Springer-Verlag, Berlin Heidelberg, 1990.
- 890 De Vicente, G.: Análisis Poblacional de Fallas. El sector de enlace Sistema Central-
891 Cordillera Ibérica. Ph.D. thesis, Universidad Complutense de Madrid, Spain, 317
892 pp., 1988.
- 893 [De Vicente, G. Muñoz, A., Giner, J.L.: Use of the Right Dihedral Method: implications](#)
894 [from the Slip Model of Fault Population Analysis, *Rev. Soc. Geol. España*, 5\(3-4\), 7-](#)
895 [19. 1992.](#)
- 896 De Vicente, G., Cloetingh, S., Muñoz-Martín, A., Olaiz, A., Stich, D., Vegas, R.,
897 Galindo-Zaldivar, J., and Fernández-Lozano, J.: Inversion of moment tensor focal
898 mechanisms for active stresses around Microcontinent Iberia: Tectonic implications,
899 *Tectonics*, 27: 1-22, <http://dx.doi.org/10.1029/2006TC002093>, 2008.
- 900 De Vicente, G., Cloetingh, S., Van Wees, J. D., and Cunha, P. P.: Tectonic
901 classification of Cenozoic Iberian foreland basins, *Tectonophysics*, 502, 38–61,
902 <http://dx.doi.org/10.1016/j.tecto.2011.02.007>, 2011.
- 903 Etchecopar, A., Vasseur, G., and Daignieres, M.: An inverse problem in microtectonics
904 for the determination of stress tensor from fault striation analysis, *J. Struct. Geol.*, 3,
905 51-65, [http://dx.doi.org/10.1016/0191-8141\(81\)90056-0](http://dx.doi.org/10.1016/0191-8141(81)90056-0), 1981.

- 906 Fernández, M., Marzán, I., Correia, A., and Ramalho, E.: Heat flow, heat production,
907 and lithospheric thermal regime in the Iberian Peninsula, *Tectonophysics*, 291, 29-
908 53, [http://dx.doi.org/10.1016/S0040-1951\(98\)00029-8](http://dx.doi.org/10.1016/S0040-1951(98)00029-8), 1998.
- 909 Foulger, G. R., Wilson, M., Gluyas, J., Julian, B. R. and Davies, R.: Global review of
910 human-induced earthquakes, *Earth-Sci. Rev.*, 178, 438–514,
911 <http://dx.doi.org/10.1016/j.earscirev.2017.07.008>, 2018.
- 912 Frohlich, C.: Two-year survey comparing earthquake activity and injection-well
913 locations in the Barnett Shale, Texas. *PNAS*, vol. 109 (35), 13934 – 13938,
914 <https://doi.org/10.1073/pnas.1207728109>, 2012.
- 915 García-Mondéjar, J., Pujalte, V. and Robles, S.: Características sedimentológicas,
916 secuenciales y tectoestratigráficas del Triásico de Cantabria y norte de Palencia,
917 *Cuad. Geol. Ibérica*, (10), 151–172, 1986.
- 918 García-Mondéjar, J., Agirrezabala, L. M., Aranburu, A., Fernández-Mendiola, P. A.,
919 Gómez-Pérez, I., López-Horgue, M. and Rosales, I.: Aptian-Albian tectonic pattern
920 of the Basque-Cantabrian Basin (Northern Spain), *Geological Journal*, 31(1), 13–45,
921 [http://dx.doi.org/10.1002/\(SICI\)1099-1034\(199603\)31:1<13::AID-GJ689>3.0.CO;2-](http://dx.doi.org/10.1002/(SICI)1099-1034(199603)31:1<13::AID-GJ689>3.0.CO;2-Y)
922 [Y](http://dx.doi.org/10.1002/(SICI)1099-1034(199603)31:1<13::AID-GJ689>3.0.CO;2-Y), 1996.
- 923 Gastine, M., Berenblyum, R., Czernichowski-lauriol, I., de Dios, J. C., Audigane, P.,
924 Hladik, V., Poulsen, N., Vercelli, S., Vincent, C., and Wildenborg, T.: Enabling
925 onshore CO₂ storage in Europe: fostering international cooperation around pilot and
926 test sites, *Energy Proced.*, 114, 5905–5915,
927 <http://dx.doi.org/10.1016/j.egypro.2017.03.1728>, 2017.
- 928 Giner-Robles, J.L., Pérez-López, R., Elez, J., Silva, P.G., Rodríguez Escudero, E.,
929 Canora, C., Rodríguez-Pascua, M.A., Bardají, T., Roquero, E., Huerta, P., Perucha,
930 M.A.: Strain analysis in the Iberian Peninsula from focal mechanism solutions,
931 seismic hazard impacts, In: C. Canora, F. Martín, E. Masana, R. Pérez y M. Ortuño,
932 Eds., pp. 249-252. Tercera reunión ibérica sobre fallas activas y paleosismología,
933 Alicante (España), 2018.
- 934 Goldberg, D. S., Kent, D. V., and Olsen, P. E.: Potential on-shore and off-shore
935 reservoirs for CO₂ sequestration in Central Atlantic magmatic province basalts, *P.*
936 *Natl. Acad. Sci. USA*, 107, 1327–1332, <http://dx.doi.org/10.1073/pnas.0913721107>,
937 2010.

Código de campo cambiado

Con formato: Inglés (Reino Unido)

Con formato: Inglés (Reino Unido)

Con formato: Español (alfab. internacional)

Código de campo cambiado

Con formato: Español (alfab. internacional)

Con formato: Español (alfab. internacional)

- 938 Gómez, M., Vergés, J. and Riaza, C.: Inversion tectonics of the northern margin of the
939 Basque Cantabrian Basin, *Bulletin de la Société Géologique de France*, 173(5), 449–
940 459, <http://dx.doi.org/10.2113/173.5.449>, 2002.
- 941 ~~[Hanks, T.C., Kanamori, H.: A Moment Magnitude Scale, *J. Geophys. Res.*, 84 \(B5\),](#)~~
942 ~~[2348–2350, <https://doi.org/10.1029/JB084iB05p02348>, 1979.](#)~~
- 943 ~~[Goodman, R. E.: *Introduction to Rock Mechanics*, 2nd Edition, John Wiley & Sons, Inc.,](#)~~
944 ~~[New York. 576 pp., 1989.](#)~~
- 945 Herraiz, M., De Vicente, G., Lindo-Naupari, R., Giner, J., Simón, J.L., González-
946 Casado, J.M., Vadillo, O., Rodríguez-Pascua, M.A., Cicuéndez, J.I., Casas, A.,
947 Cabañas, L., Rincón, P., Cortés, A.L., Ramírez, M., and Lucini, M.: The recent
948 (upper Miocene to Quaternary) and present tectonic stress distributions in the Iberian
949 Peninsula, *Tectonics*, 19, 762–786, <https://doi.org/10.1029/2000TC900006>, 2000.
- 950 Holford, S. M., Hillis, R. R., Hand, M., and Sandiford, M.: Thermal weakening
951 localizes intraplate deformation along the southern Australian continental margin,
952 *Earth Planet. Sc. Lett.*, 305, 207–214, <http://dx.doi.org/10.1016/j.epsl.2011.02.056>,
953 2011.
- 954 Huang, Y., Beroza, G. C., and Ellsworth, W. L.: Stress drop estimates of potentially
955 induced earthquakes in the Guy-Greenbrier sequence, *J. Geophys. Res.-Sol. Ea.*, 121,
956 6597–6607, <http://dx.doi.org/10.1002/2016JB013067>, 2016.
- 957 ~~[Kanamori, H.: The energy release in great earthquakes, *J. Geophys. Res.*, 82 \(20\),](#)~~
958 ~~[2981–2987, \[doi:10.1029/JB082i020p02981\]\(https://doi.org/10.1029/JB082i020p02981\), 1977.](#)~~
- 959 Kaverina, A. N., Lander, A. V., and Prozorov, A. G.: Global creepex distribution and its
960 relation to earthquake-source geometry and tectonic origin, *Geophys. J. Int.*, 125,
961 249–265, <https://doi.org/10.1111/j.1365-246X.1996.tb06549.x>, 1996.
- 962 ~~[Labuz, J. F., Zang, A.: Mohr–Coulomb Failure Criterion. *Rock Mech. Rock Eng.*, 45,](#)~~
963 ~~[975–979, <https://doi.org/10.1007/s00603-012-0281-7>, 2012.](#)~~
- 964 ~~[Landgraf, A., Kuebler, S., Hintersberger, E., Stein, S.: Active tectonics, earthquakes and](#)~~
965 ~~[palaeoseismicity in slowly deforming continents, Landgraf, A., Kuebler, S.,](#)~~
966 ~~[Hintersberger, E. & Stein, S. \(eds\) *Seismicity, Fault Rupture and Earthquake*](#)~~
967 ~~[Hazards in Slowly Deforming Regions. Geological Society, London, Special](#)~~
968 ~~[Publications, 432, <http://doi.org/10.1144/SP432.13>, 2018.](#)~~
- 969 Le Gallo, Y. and de Dios, J. C.: Geological Model of a Storage Complex for a CO₂
970 Storage Operation in a Naturally-Fractured Carbonate Formation, *Geosciences*, 2018,
971 8, 354, <http://dx.doi.org/10.3390/geosciences8090354>, 2018.

Con formato: Superíndice

Con formato: Inglés (Reino Unido)

Con formato: Inglés (Reino Unido)

- 972 Le Pichon, X. and Sibuet, J.-C.: Western extension of boundary between European and
973 Iberian plates during the Pyrenean orogeny, *Earth and Planetary Science Letters*,
974 12(1), 83–88, [http://dx.doi.org/10.1016/0012-821X\(71\)90058-6](http://dx.doi.org/10.1016/0012-821X(71)90058-6), 1971.
- 975 Lepvrier, C. and Martínez-García, E.: Fault development and stress evolution of the
976 post-Hercynian Asturian Basin (Asturias and Cantabria, northwestern Spain),
977 *Tectonophysics*, 184, 345, [http://dx.doi.org/10.1016/0040-1951\(90\)90447-G](http://dx.doi.org/10.1016/0040-1951(90)90447-G), 1990.
- 978 Lisle, R. J., Aller, J., Bastida, F., Bobillo-Ares, N. C., and Toimil, N. C.: Volumetric
979 strains in neutral surface folding, *Terra Nova*, 21, 14–20,
980 <http://dx.doi.org/10.1111/j.1365-3121.2008.00846.x>, 2009.
- 981 McGarr, A.: Maximum magnitude earthquakes induced by fluid injection, *J. Geophys.*
982 *Res.*, 119, 1008–1019, <https://doi.org/10.1002/2013JB010597>, 2014.
- 983 McNamara, D.D. Methods and techniques employed to monitor induced seismicity
984 from carbon capture and storage, *GNS Science Report 2015/18*, 23 pp.,
985 <http://dx.doi.org/10.13140/RG.2.2.13830.98888>, 2016.
- 986 Muñoz, J. A.: Evolution of a continental collision belt: ECORS-Pyrenees crustal
987 balanced cross-section, in *Thrust Tectonics*, edited by K. R. McClay, pp. 235–246,
988 Springer Netherlands, Dordrecht., 1992.
- 989 Ogaya, X., Ledo J., Queralt P., Marcuello, A., and Quintà, A.: First geoelectrical image
990 of the subsurface of the Hontomín site (Spain) for CO₂ geological storage: A
991 magnetotelluric 2D characterization, *Int. J. Greenh. Gas Con.*, 13, 168–179,
992 <https://dx.doi.org/10.1016/j.ijggc.2012.12.023>, 2013.
- 993 Orr, F.M.: Onshore Geologic Storage of CO₂, *Science*, 325, 1656-1658,
994 <http://dx.doi.org/10.1126/science.1175677>, 2009.
- 995 [Pan, P., Wu, Z., Feng, X., Yan, F.: Geomechanical modeling of CO₂ geological storage:
996 A review, *J. Rock Mech. and Geotech. Eng.*, 8, 936-947,
997 <http://dx.doi.org/10.1016/j.jrmge.2016.10.002>, 2016.](#)
- 998 Pérez-López, R., Mediato, J.F., Rodríguez-Pascua, M.A., Giner-Robles, J.L., Martínez-
999 Orío, R., Arenillas-González, A., Fernández-Canteli, P., de Dios, J.C., Loubeau, L.:
1000 Aplicación del análisis estructural y campos de deformación para el estudio de
1001 sismicidad inducida en almacenamiento profundo: Hontomín, In: C. Canora, F.
1002 Martín, E. Masana, R. Pérez y M. Ortuño, Eds., pp. 279-282. Tercera reunión ibérica
1003 sobre fallas activas y paleosismología, Alicante (España), 2018.
- 1004 Pearce, J. M.: What can we learn from Natural Analogues? An overview of how
1005 analogues can benefit the geological storage of CO₂, in: *Advances in the Geological*

Con formato: Inglés (Reino Unido)

Con formato: Inglés (Reino Unido)

Con formato: Inglés (Reino Unido)

Con formato: Inglés (Reino Unido)

Con formato: Inglés (Reino Unido)

Con formato: Inglés (Reino Unido),
Subíndice

Con formato: Inglés (Reino Unido)

Con formato: Español (alfab.
internacional)

Con formato: Español (alfab.
internacional)

- 1006 Storage of Carbon Dioxide, edited by: Lombardi, S., Altunina, L. K., and Beaubien,
1007 S. E., Springer, Dordrecht, The Netherlands, 129–139, 2005.
- 1008 Pegoraro, O.: Application de la microtectonique à un étude de neotectonique. Le golfe
1009 Maliaque (Grèce centrale). Ph.D. thesis, U.S.T.L. Montpellier, France, 41 pp., 1972.
- 1010 Permentier, K., Vercammen, S., Soetaert, S., and Schellemans, Ch.: Carbon dioxide
1011 poisoning: a literature review of an often forgotten cause of intoxication in the
1012 emergency department, *International Journal of Emergency Medicine*, 10, 14,
1013 <http://dx.doi.org/10.1186/s12245-017-0142-y>, 2017.
- 1014 Quintà, A. and Tavani S., The foreland deformation in the south-western Basque–
1015 Cantabrian Belt (Spain), *Tectonophysics*, 576–577, 4–19,
1016 <http://dx.doi.org/10.1016/j.tecto.2012.02.015>, 2012.
- 1017 Reches, Z.: Faulting of rocks in three-dimensional strain fields, II. Theoretical analysis,
1018 *Tectonophysics*, 95, 133-156, [https://doi.org/10.1016/0040-1951\(83\)90264-0](https://doi.org/10.1016/0040-1951(83)90264-0), 1983.
- 1019 Reches, Z.: Determination of the tectonic stress tensor from slip along faults that obey
1020 the Coulomb yield condition, *Tectonics*, 7, 849-861,
1021 <https://doi.org/10.1029/TC006i006p00849>, 1987.
- 1022 Rice, S. A.: Health effects of acute and prolonged CO₂ exposure in normal and sensitive
1023 populations, Second Annual Conference on Carbon Sequestration, Alexandria,
1024 Virginia, USA, 5-6 May, 2003.
- 1025 Roca, E., Muñoz, J. A., Ferrer, O. and Ellouz, N.: The role of the Bay of Biscay
1026 Mesozoic extensional structure in the configuration of the Pyrenean orogen:
1027 Constraints from the MARCONI deep seismic reflection survey, *Tectonics*, 30(2),
1028 <https://10.1029/2010TC002735>, 2011.
- 1029 Röhrmann, L., Tillner, E., Magri, F., Kühn, M., and Kempka, T.: Fault reactivation and
1030 ground surface uplift assessment at a prospective German CO₂ storage site, *Energy*
1031 *Proced.*, 40, 437–446. <http://dx.doi.org/10.1016/j.egypro.2013.08.050>, 2013.
- 1032 Scholz, C.: The seismic cycle. In *The Mechanics of Earthquakes and Faulting* 3rd
1033 *edition*, Cambridge, Cambridge University Press, pp. 228-277, 2018.
- 1034 Serrano, A. and Martínez del Olmo, W.: Tectónica salina en el Dominio Cantabro–
1035 Navarro: evolución, edad y origen de las estructuras salinas, in: Formaciones
1036 evaporíticas de la Cuenca del Ebro y cadenas perifericas, y de la zona de Levante,
1037 edited by: Orti, F. and Salvany, J.M., Empresa Nacional De Residuos Radiactivos
1038 S.A, ENRESA-GPPG, Barcelona, Spain, 39–53, 1990.

Con formato: Inglés (Reino Unido)

Con formato: Inglés (Reino Unido)

Con formato: Superíndice

Con formato: Inglés (Reino Unido)

Con formato: Inglés (Reino Unido)

Con formato: Inglés (Reino Unido)

- 1039 Simpson, R. S.: Quantifying Anderson's fault types, *J. Geophys. Res.*, 102, 17,909-
1040 17,919, <https://doi.org/10.1029/97JB01274>, 1997.
- 1041 Stich, D., Serpelloni, E., Mancilla, F. L., and Morales, J.: Kinematics of the Iberia-
1042 Maghreb plate contact from seismic moment tensors and GPS observations,
1043 *Tectonophysics*, 426, 295-317. <https://doi.org/10.1016/j.tecto.2006.08.004>, 2006.
- 1044 Soto R., Casa-Sainz A. M., and Villalaín, J. J.: Widespread Cretaceous inversion event
1045 in northern Spain: evidence from subsurface and palaeomagnetic data, *Journal of the*
1046 *Geological Society London*, 168, 899-912, [http://dx.doi.org/10.1144/0016-](http://dx.doi.org/10.1144/0016-76492010-072)
1047 [76492010-072](http://dx.doi.org/10.1144/0016-76492010-072), 2011.
- 1048 Tavani, S., Quintá, A., and Granado, P.: Cenozoic right-lateral wrench tectonics in the
1049 Western Pyrenees (Spain): The Ubierna Fault System, *Tectonophysics*, 509, 238-
1050 253, <http://dx.doi.org/10.1016/j.tecto.2011.06.013>, 2011.
- 1051 Tavani, S.: Plate kinematics in the Cantabrian domain of the Pyrenean orogeny, *Solid*
1052 *Earth*, 3, 265–292, <http://dx.doi.org/10.5194/se-3-265-2012>, 2012
- 1053 Tavani, S., Carola, C., Granado, P., Quintà, A., and Muñoz, J. A.: Transpressive
1054 inversion of a Mesozoic extensional forced fold system with an intermediate
1055 décollement level in the Basque - Cantabrian Basin (Spain), *Tectonics*, 32,
1056 <http://dx.doi.org/10.1002/tect.20019>, 2013.
- 1057 Torne, M., Fernández, M., Vergés, J., Ayala, C., Salas, M. C., Jimenez-Munt, I.,
1058 Buffett, G. G., and Díaz, J.: Crust and mantle lithospheric structure of the Iberian
1059 Peninsula deduced from potential field modeling and thermal analysis,
1060 *Tectonophysics*, 663, 419–433, <http://dx.doi.org/10.1016/j.tecto.2015.06.003>, 2015.
- 1061 Tugend, J., Manatschal, G., Kuszniir, N. J., Masini, E., Mohn, G. and Thinon, I.:
1062 Formation and deformation of hyperextended rift systems: Insights from rift domain
1063 mapping in the Bay of Biscay-Pyrenees, *Tectonics*, 33(7), 1239–1276,
1064 <http://dx.doi.org/10.1002/2014TC003529>, 2014.
- 1065 Vegas, R., Vázquez, J. T., Olaiz, A. J., and Medialdea, T.: Tectonic model for the latest
1066 Triassic - Early Jurassic extensional event in and around the Iberian Peninsula,
1067 *Geogaceta*, 60, 23-26, 2016.
- 1068 Verdon, J. P.: Significance for secure CO₂ storage of earthquakes induced by fluid
1069 injection, *Environ. Res. Lett.*, 9, 064022 (10pp), [http://dx.doi.org/10.1088/1748-](http://dx.doi.org/10.1088/1748-9326/9/6/064022)
1070 [9326/9/6/064022](http://dx.doi.org/10.1088/1748-9326/9/6/064022), 2014.

Código de campo cambiado

- 1071 Verdon, J. P., Stork, A. L., Bissell, R. C., Bond, C. E., and Werner, M. J.: Simulation of
1072 seismic events induced by CO₂ injection at In Salah, Algeria, *Earth Planet. Sci. Lett.*,
1073 426, 118–129, <http://dx.doi.org/10.1016/j.epsl.2015.06.029>, 2015.
- 1074 Vergés, J., Fernández, M. and Martínez, A.: The Pyrenean orogen: pre-, syn-, and post-
1075 collisional evolution, *J. Virt. Ex.*, 08, <http://dx.doi.org/10.3809/jvirtex.2002.00058>,
1076 2002.
- 1077 Wells, D. L. and Coppersmith, K. J.: New empirical relationships among magnitude,
1078 rupture length, rupture width, rupture area, and surface displacement, *B. Seismol.*
1079 *Soc. Am.*, 84, 974–1002, 1994.
- 1080 Wilson, M. P., Foulger, G. R., Gluyas, J. G., Davies, R. J., and Julian, B. R.: HiQuake
1081 the human-induced earthquake database, *Seismol. Res. Lett.*, 88, 1560-1565,
1082 <http://dx.doi.org/10.1785/0220170112>, 2017.
- 1083 Winthaegen, P., Arts, R., and Schroot, B.: Monitoring Subsurface CO₂ Storage. *Oil Gas*
1084 *Sci. Technol.*, 60, 573-582, 2005.
- 1085 Xu, S.-S., A.F. Nieto-Samaniego, S.A. Alaniz-Álvarez: 3D Mohr diagram to explain
1086 reactivation of pre-existing planes due to changes in applied stresses, *Rock Stress*
1087 and Earthquakes – Xie (ed.), 739-745 p, 2010.
- 1088 Žalohar, J. and Vrabec, M.: Combined kinematic and paleostress analysis of fault-slip
1089 data: The Multiple-slip method, *J. Struct. Geol.*, 30, 1603–1613,
1090 <http://dx.doi.org/10.1016/j.jsg.2008.09.004>, 2008.

Con formato: Inglés (Reino Unido)

Con formato: Inglés (Reino Unido)

Con formato: Inglés (Reino Unido)

Con formato: Sangría: Izquierda: 0 cm, Primera línea: 0 cm

1093 **FIGURE CAPTIONS**

1094

1095 **Figure 1.** a) Location map of the study area in the Iberian Peninsula, along with the
1096 geological map of the Asturian and Basque-Cantabrian areas, labelling major units and
1097 faults (modified after Quintà and Tavani 2012); b) Geographical location of Hontomín
1098 pilot-plant (red dot) within the Basque-Cantabrian Basin. This basin is tectonically
1099 controlled by the Ubierna Fault System (UFS; NW-SE oriented) and the parallel
1100 Polientes syncline, the Duero and Ebro Tertiary basins and Poza de la Sal evaporitic
1101 diapir. Cret: Cretaceous; F: Facies.

1102

1103 **Figure 2.** Interpretation of a 2D seismic reflection profile crossing the oil exploration
1104 wells (H1, H2 and H4), along with the monitoring well (Ha) and injection well (Hi)
1105 through Hontomin Pilot Plant (HPP). Modified from Alcalde et al. (2014). See Figure 1
1106 for location, black line at the red circle.

1107

1108 **Figure 3.** a) Kaverina original diagram to represent the tectonic regime from an
1109 earthquake focal mechanism population (see Kaverina et al., 1996 and Álvarez-Gómez,
1110 2014). b) K' -strain diagram used in this work. Dotted lines represent the original
1111 Kaverina limits. Colored zones represent the type of fault. The tectonic regime is also
1112 indicated by the relationship between the strain axes and the colored legend. SS Strike
1113 slip. The B axis is the orthogonal to the P and T axes.

1114

1115 **Figure 4.** Methodology proposed to obtain the strain field affecting the ~~CCS-GSC~~
1116 reservoir. The distances for outcrops and quadrants proposed is 20 km. The technique of
1117 Right Dihedral and the K' strain diagram is described in the main text. The e_y and e_x
1118 represented are a model for explaining the methodology. Dey and Dex are the direction
1119 of the maximum and minimum strain, respectively. Blue box at the center is the CO_2
1120 storage geological underground formation.

1121

1122 **Figure 5.** Geographical location of field outcrops in the eastern part of the Burgalesa
1123 Platform domain. Black lines: observed faults; red circle: 20km radius study zone. Rosd
1124 diagram are the fault orientations from the map. A total of 447 fault data were collected
1125 in 32 outcrops. Data were measured by a tectonic compass on fault planes at outcrops.

Con formato: Subíndice

1126 The spatial distribution of the field stations is constrained by the lithology. Coordinates
1127 are in meters, UTM H30.

1128

1129 **Figure 6.** Stereographic representation (cyclographic plot in Schmidt net, lower
1130 hemisphere) of the fault planes measured in the field stations. “n” is the number of
1131 available data for each geostructural station. HTM24, 27, 28 are not included due to
1132 lack of data, and HTM17 due to the high number of faults.

1133

1134 **Figure 7.** Results of the paleostrain analysis obtained and classified by age. Deym:
1135 striking of the averaged of the Dey value; F: fault stereographic representation; K':
1136 diagram with dots for each fault slip solution; RD: Right Dihedral method; SM: Slip
1137 Method, K'. See Methods for further explanation.

1138

1139 **Figure 8.** Fault data from the outcrop HTM17 located on top of the HPP. See figure 5
1140 for the geographical location. Stereogram plot is lower hemisphere and Schmidt net.
1141 Upper left frame: Synthesis of the K' map obtained from Giner Robles et al. (2018) for
1142 the whole Iberian Peninsula from focal mechanism solutions. HPP is located between a
1143 triple junction of K' defined by compression towards the north, extension to the
1144 southeast and strike-slip to the west. Black dots are the earthquakes with focal
1145 mechanism solutions used. Sketches represent the σ_1 , SHmax trajectories obtained from
1146 the outcrops for early Triassic, Early Cretaceous, Late Cretaceous, Early Oligocene,
1147 Early–Middle Miocene and Present-day strain field from Herraiz et al. (2000). Main
1148 structures activated under the strain field defined are also included.

1149

1150 **Figure 9.** Normal and reverse faults stereograms (lower hemisphere and Schmidt net),
1151 and rose diagrams measured in HTM17. Green arrows indicate the orientation of the
1152 local paleostrain field. Grey arrows indicate the orientation of the present-day regional
1153 stress field (Herraiz et al., 2000).

1154 Tectonic field evolution of the Burgalesa Platform domain (20 km radius circle centered
1155 at HPP), interpreted from the paleostrain analysis. The regional tectonic field from other
1156 authors are also included. Ages were estimated from the HTM outcrops affecting
1157 geological well-dated deposits. N: extensional faulting; R: compressive faulting; SS:
1158 strike-slip faulting. Red and white means local paleostrain field, and red with white dots
1159 means superposed modern paleostrain field.

1160 **Figure 10.** Mohr-Coulomb failure analysis for the fault-slip data measured in HTM17
1161 under the present-day stress tensor determined by Herraiz et al. (2000). Red dots are
1162 faults reactivated, and green and orange dots are located within the stable zone. Red
1163 rose diagram shows the orientation of reactivated faults, between N-S to N60°E and
1164 from N115°E to N180°E. Green rose diagram shows the fault orientation for faults non-
1165 reactivated under the active tress field within the area. See text for further details.

Con formato: Fuente: Negrita

1166
1167 **Figure 11.** a) Stereogram and poles of fault sets (HTM17) reactivated under the present-
1168 day stress field suggested by Herraiz et al. (2000). b) Right-Dihedral of the reactivated
1169 fault sets. c) K'-strain diagram showing the type of fault for each fault-set.

Con formato: Fuente: Negrita

1170

1171 **TABLE CAPTIONS**

1172

1173 **Table 1.** Different tectonic regimes, K' values, dip values and fault type for the
1174 Kaverina modified diagram used in this work. According to the strain axes relationship,
1175 faults can be classified and the tectonic regime can be established.

1176

1177 **Table 2.** Summary of the outcrops showing the number of faults, the type of the strain
1178 tensor obtained, the Dey, S_{Hmax} striking and the age of the affected geological materials.

1179 ~~Asterisk indicates those field stations detailed in the figure 7.~~ N-C is normal component
1180 for strike-slip movement.

1181

Con formato: Subíndice

Dear Dave,

Thank you very much for your comments. We agree with your recommendations and consequently, we have included the volume estimation of the total injected brine plus CO₂ in reservoir conditions. Also, a brief explanation about the orange dots obtained in M-C analysis is included in the caption of Figure 10 and finally, we have discussed the role of the slip and dilatation tendency as suggested.

Best regards,

The authors

DETAILED COMMENTS:

I would like to insist on one more change: please calculate the volume of the CO₂ at the reservoir conditions (depth/pressure, temperature) and then re-calculate the maximum predicted moment for comparison to the room conditions value. This is important, as it will surely be less.

New calculation and text:

We have applied a physic model to estimate the total volume injected (room conditions) and in reservoir conditions. Then we have applied the McGarr's (2014) approximation of the maximum expected seismic moment for induced earthquakes. The injection of 10 k tons of CO₂ in Hontomín (Gastine et al., 2017), represents an approximated injected volume of CO₂ of 5.56 x10⁶ m³ (room conditions, pressure of 1 bar and temperature of 20 °C). The P/T conditions at the bottom of the wells have a maximum value close to 190 bar (Ortiz et al., 2015; Kovacs et al., 2015), although oscillating between 125 and 170 bar and with a maximum temperature close to 58 °C. Kovacs et al. (2015) pointed out a pressure gradient 0,023 MPa/m and a thermal vertical gradient of 0.033 °C/m, which would correspond to a pressure of 357 bar and 51 °C at 1,550 m depth. P/T bottom values obtained from the observational wells (HA and HI) by Ortiz et al. (2015) and Kovacs et al. (2015), were 170 bar and 42 °C respectively.

We have used the general law for gases $P_1 \cdot V_1 / T_1 = P_2 \cdot V_2 / T_2$. Therefore, the total injected volume in reservoir conditions according to the parameters observed at the bottom of the wells are, $P_1 = 1.01$ bar, $T_1 = 20$ °C, $V_1 = 5.56 \times 10^6$ m³, $P_2 = 170$ bar and $T_2 = 42$ °C. Hence, the total volume of injected CO₂ plus brine is 6.94×10^4 m³.

McGarr (2014) empirically determined the maximum seismic moment related to a volume increasing by underground injection. The expression is $M_o(max) (Nm) = G \cdot \Delta V$ (McGarr 2014, eq. 13), where G is the modulus of rigidity and for the upper limit is 3×10^{10} Pa, and ΔV is the total injected volume (we have used the total injected volume in reservoir conditions). The result is $M_o(max)$ equal to 2.1×10^{15} Nm, which corresponds to a maximum seismic moment magnitude $M_w (max) = 4.2$, by applying the equation $M_w = (Log M_o(max) - 9.05)/1.5$ from Hanks and Kanamori (1979); where Log is the logarithm to the base 10.

The Mohr-Coulomb diagrams in relation to Reviewer 1 comments are good, but you might want to look at slip and dilation tendency (Morris et al., 1996; Ferrill et al., 1999) too, if not for this paper then for the future.

We guess that the complete reference is Morris, Alan, David A. Ferrill and D. Brent Henderson: Slip-tendency analysis and fault reactivation. *Geology*, 24,275-278. doi: [http://doi.org/10.1130/0091-7613\(1996\)024<0275:STAAFR>2.3.CO;2](http://doi.org/10.1130/0091-7613(1996)024<0275:STAAFR>2.3.CO;2), 1996.

Yes, we are aware of this type of analysis for fault reactivation and it is totally complementary with our work. In fact, applying this analysis is similar because both analyses are based on the same concepts: stress tensor (R and K) and the fault orientation. Moreover, if you see the original paper of Morris et al. (1996), Fig. 4A shows σ_2 with N-S trend and σ_3 with E-W trend, under a strike-slip stress tensor. In this context, the most likelihood fault orientation to slip reactivation is N-S with dip greater than 59°. These values are similar to our results in Hontomin, with the same stress tensor and fault orientation than Morris et al. (1996), but in the Basque Cantabria basin instead of Yucca Mountains. The most interesting thing is that results are similar in both cases. Anyway, we can perform this kind of analysis combined with our analysis but as you say, for future works. Even so, we have mentioned this type of analysis in Discussion section of fault reactivation. Thank you for the suggestion.

Included text:

We propose as a complementary and future work, a combined analysis between the fault population analysis and the slip-tendency analysis (Morris et al. 1996), which could improve and discriminate those fault sets most likely to be reactivated under an active stress field. Although both analyses (Fault Population and slip-tendency) are based on the stress tensor and the orientation of fault traces, the slip-tendency also includes rock strength values obtained from the "in situ" tests.

Also, what are the yellow data on the M-C plot? They do not have a corresponding rose plot...

The yellow data in the M-C diagrams are referred to those planes close to be reactivated, and potentially reactivated by increasing the pore pressure.

We have included this sentence in the caption of Figure 9.

REFERENCES

Morris, Alan, David A. Ferrill and D. Brent Henderson: Slip-tendency analysis and fault reactivation. *Geology*, 24,275-278. [http://doi.org/10.1130/0091-7613\(1996\)024<0275:STAAFR>2.3.CO;2](http://doi.org/10.1130/0091-7613(1996)024<0275:STAAFR>2.3.CO;2), 1996.

Ortiz, G., Kovacs, T., Poulussen, D.F. and C.de Dios: Hontomin reservoir characterisation test. Final Technical Report. Global Carbon Capture and Storage Institute Ltd. 2015. 48p. 2015. <https://www.globalccsinstitute.com/resources/publications-reports-research/?filter=2015-05-01,2015-07-25&type=date>

Kovacs, T., Poulussen D.F. and C.de Dios: Strategies for injection of CO₂ into carbonate rocks at Hontomin. Final Technical Report. Global Carbon Capture and Storage Institute Ltd. 2015. 66p. 2015. <https://www.globalccsinstitute.com/archive/hub/publications/193428/strategies-injection-co2-carbonate-rocks-hontomin-final-technical-report.pdf>

Active tectonic field for CO₂ Storage management: Hontomín onshore study-case (SPAIN)

Raúl Pérez-López¹, José F. Mediato¹, Miguel A. Rodríguez-Pascua¹, Jorge L. Giner-Robles², Adrià Ramos¹, Silvia Martín-Velázquez³, Roberto Martínez-Orío¹, Paula Fernández-Canteli¹

1. IGME – Instituto Geológico y Minero de España – Geological Survey of Spain. C/Ríos Rosas 23, Madrid 28003 – SPAIN. Email: r.perez@igme.es, jf.mediato@igme.es, ma.rodriguez@igme.es, a.ramos@igme.es, ro.martinez@igme.es, paula.canteli@igme.es
2. Departamento de Geología y Geoquímica. Facultad de Ciencias. Universidad Autónoma de Madrid. Campus Cantoblanco, Madrid. SPAIN. Email: jorge.giner@uam.es
3. Universidad Rey Juan Carlos. Email: silvia.martin@urjc.es

Abstract

One of the concerns of underground CO₂ onshore storage is the triggering of Induced Seismicity and fault reactivation by pore pressure increasing. Hence, a comprehensive analysis of the tectonic parameters involved in the storage rock formation is mandatory for safety management operations. Unquestionably, active faults and seal faults depicting the storage bulk are relevant parameters to be considered. However, there is a lack of analysis of the active tectonic strain field affecting these faults during the CO₂ storage monitoring. The advantage of reconstructing the tectonic field is the possibility to determine the strain trajectories and describing the fault patterns affecting the reservoir rock. In this work, we adapt a methodology of systematic geostructural analysis to the underground CO₂ storage, based on the calculation of the strain field and defined by the strain field from kinematics indicators on the fault planes (e_y and e_x for the maximum and minimum horizontal shortening respectively). This methodology is based on a statistical analysis of individual strain tensor solutions obtained from fresh outcrops from Triassic to Miocene. Consequently, we have collected 447 fault data in 32 field stations located within a 20 km radius. The understanding of the fault sets role for underground fluid circulation can also be established, helping for further analysis about of CO₂ leakage and seepage. We have applied this methodology to Hontomín

Con formato: Español (alfab. internacional)

Con formato: Español (alfab. internacional)

Con formato: Español (alfab. internacional)

Código de campo cambiado

Con formato: Español (alfab. internacional)

Código de campo cambiado

Con formato: Español (alfab. internacional)

Con formato: Español (alfab. internacional)

Código de campo cambiado

Con formato: Español (alfab. internacional)

Con formato: Español (alfab. internacional)

Código de campo cambiado

Con formato: Español (alfab. internacional)

Con formato: Español (alfab. internacional)

Código de campo cambiado

Con formato: Español (alfab. internacional)

Con formato: Español (alfab. internacional)

Código de campo cambiado

Con formato: Español (alfab. internacional)

Código de campo cambiado

32 onshore CO₂ storage facilities (Central Spain). The geology of the area and the number
33 of high-quality outcrops made this site as a good candidate for studying the strain field
34 from kinematics fault analysis. The results indicate a strike-slip tectonic regime with the
35 maximum horizontal shortening with N160°E and N50°E trend for local regime, which
36 activates NE-SW strike-slip faults. A regional extensional tectonic field was also
37 recognized with N-S trend, which activates N-S extensional faults, and NNE-SSW and
38 NNW-SSE strike-slip faults, measured in the Cretaceous limestone on top of the
39 Hontomín facilities. Monitoring these faults within the reservoir is suggested in addition
40 ~~with to~~ the possibility of obtaining focal mechanism solutions for microearthquakes (M
41 < 3).

42

43 Keywords: onshore CO₂ storage, tectonic field, paleostrain analysis, active fault,
44 Hontomín onshore pilot-plant.

45

46 1. INTRODUCTION

47 Industrial made-man activities generate CO₂ that could change the chemical balance of
48 the atmosphere and their relationship with the geosphere. The Geological Carbon
49 Storage (GSC) appears as a good choice to reduce the CO₂ gas emission to the
50 atmosphere (Christensen, 2004), allowing the industry increasing activity with a low
51 pollution impact. There is a lot of literature about what must have a site to be a potential
52 underground storage suitable to GSC (e.g. Chu, 2009; Orr, 2009; Goldberg et al., 2010
53 among others). The reservoir sealing, the caprock, permeability and porosity, plus
54 injection pressure and volume injected, are the main considerations to choose one
55 geological subsurface formation as the CO₂ host-rock. In this frame, the tectonic active
56 field is considered in two principal ways: (1) to prevent the fault activation and

57 earthquakes triggering, with the consequence of leakage and seepage, and (2) the long-
58 term reservoir behavior, understanding as long-term from centennial to millennial time-
59 span. Therefore, what is the long-term behavior of GSC? What do we need to monitor
60 for a safe GSC management? [Winthaegen et al. \(2005\)](#) suggest three subjects for
61 monitoring: (a) the atmosphere air quality near the injection facilities, due to the CO₂
62 toxicity (values greater than 4%, see [Rice, 2003](#) and [Permentier et al., 2017](#)), (b) the
63 overburden monitoring faults and wells and (c) the sealing of the reservoir. The study of
64 natural analogues for GSC is a good strategy to estimate the long-term behavior of the
65 reservoir, considering parameters as the injected CO₂ pressure and volume, plus the
66 brine mixing with CO₂ ([Pearce, 2006](#)). Hence, the prediction of site performance over
67 long timescales also requires an understanding of CO₂ behavior within the reservoir, the
68 mechanisms of migration out of the reservoir, and the potential impacts of a leak on the
69 near surface environment. The assessments of such risks will rely on a combination of
70 predictive models of CO₂ behavior, including the fluid migration and the long-term
71 CO₂-porewater-mineralogical interactions ([Pearce, 2006](#)). Once again, the tectonic
72 active field interacts directly on this assessment. Moreover, the fault reactivation due to
73 the pore pressure increasing during the injection and storage has also to be considered
74 ([Röhmman et al., 2013](#)). Despite the uplift measure by [Röhmman et al. \(2013\)](#) are
75 submillimeter (c.a. 0.021 mm) at the end of the injection processes, given the ongoing
76 occurrence of microearthquakes, long-term monitoring is required. The geomechanical
77 and geological models predict the reservoir behavior and the caprock sealing properties.
78 The role of the faults inside these models is crucial for the tectonic long-term behavior
79 and the reactivation of faults that could trigger earthquakes.

80 Concerning the Induced Seismicity, [Wilson et al. \(2017\)](#) published the Hi-Quake
81 database, with a classification of all man-made earthquakes according to the literature,

82 in an online repository (<https://inducedearthquakes.org/>, last access on May, 2019). This
83 database includes 834 projects with proved Induced Seismicity, where two different
84 cases with earthquakes as large as M 1.7, detected in swarms about 9,500
85 microearthquakes, are related to GSC operations. Additionally, [Foulger et al. \(2018\)](#)
86 pointed out that GSC can trigger earthquakes with magnitudes lesser than M 2, namely
87 the cases described in their work are as great as M 1.8, with the epicenter location 2 km
88 around the facilities. [McNamara \(2016\)](#) described a comprehensive method and
89 protocol for monitoring GSC reservoir for the assessment and management of Induced
90 Seismicity. The knowledge of active fault patterns and the stress/strain field could help
91 on designing monitoring network and identifying those faults capable of triggering
92 micro-earthquakes ($M < 2$) and/or breaking the sealing for leakage (patterns of open
93 faults for low-permeability CO₂ migration).

94 In this work, we propose that the description, the analysis and establishment of the
95 tectonic strain field have to be mandatory for long-term GSC monitoring and
96 management, implementing the fault behavior in the geomechanical models. This
97 analysis does not increase the cost for long-term monitoring, given that they are low-
98 cost and the results are acquired in a few months. Therefore, we propose a methodology
99 based on the reconstruction of the strain field from the classical studies in geodynamics
100 ([Angelier, 1979 and 1984](#); [Reches, 1983](#); [Reches, 1987](#)). As a novelty, we introduce the
101 strain fields (SF) analysis between 20 away from the subsurface reservoir deep
102 geometry, under the area of influence of induced seismicity for fluid injection. The
103 knowledge of the strain field at local scale allows classifying the type of faulting and
104 their role for leakage processes, whilst the regional scale explores the tectonic active
105 faults that could affect the reservoir. The methodology is rather simple, taking measures
106 of slickensides and striations on fault planes to establish the orientation of the maximum

107 horizontal shortening (e_y), and the minimum horizontal shortening (e_x) for the strain
108 tensor. The principal advantage of the SF analysis is the directly classification of all the
109 faults involved into the geomechanical model and the prediction of the failure
110 parameters. Besides, a Mohr-Coulomb failure analysis was performed to the fault
111 pattern recognized in the Cretaceous outcrop located on top of the pilot plant.

112 The tectonic characterization of the GSC of Hontomín was implemented in the
113 geological model described by [Le Gallo and de Dios \(2018\)](#). Beyond the use of Induced
114 Seismicity and potentially active faults, the scope of this method is to propose an initial
115 analysis to manage underground storage operations. We present how the Structural
116 Analysis of fault/slip data can improve the knowledge of the tectonic large-scale fault
117 network for the potential seismic reactivation during fluid injection and time-depend
118 scale for fluid stays.

119

120 2. HONTOMÍN ONSHORE STUDY CASE

121 2.1 Geological description of the reservoir

122 The CO₂ storage site of Hontomín is enclosed in the southern section of the Mesozoic
123 Basque–Cantabrian Basin, known as Burgalesa Platform ([Serrano and Martínez del](#)
124 [Olmo, 1990](#); [Tavani, 2012](#)), within the sedimentary Bureba Basin (**Fig. 1**). This
125 geological domain is located in the northern junction of the Cenozoic Duero and Ebro
126 basins, forming an ESE-dipping monocline bounded by the Cantabrian Mountains
127 Thrust to the north, the Ubierna Fault System (UFS) to the south and the Asturian
128 Massif to the west (**Fig. 1**).

129 The Meso-Cenozoic tectonic evolution of the Burgalesa Platform starts with a first rift
130 period during Permian and Triassic times ([Dallmeyer and Martínez-García, 1990](#);
131 [Calvet et al., 2004](#)), followed by a relative tectonic quiescence during Early and Middle

132 Jurassic times (e.g. Aurell et al., 2002). The main rifting phase took place during the
133 Late Jurassic and Early Cretaceous times, due to the opening of the North Atlantic and
134 the Bay of Biscay-Pyrenean rift system (García-Mondéjar et al., 1986; Le Pichon and
135 Sibuet, 1971; Lepvrier and Martínez-García, 1990; García-Mondéjar et al., 1996; Roca
136 et al., 2011; Tugend et al., 2014). The convergence between Iberia and Eurasia from
137 Late Cretaceous to Miocene times triggered the inversion of previous Mesozoic
138 extensional faults and the development of an E-W orogenic belt (Cantabrian domain to
139 the west and Pyrenean domain to the east) formed along the northern Iberian plate
140 margin (Muñoz, 1992; Gómez et al., 2002; Vergés et al., 2002).

141 The Hontomín facilities are located within the Basque-Cantabrian Basin (**Fig. 1b**). The
142 geological reservoir structure is bordered by the UFS to the south and west, by the Poza
143 de la Sal diapir and the Zamanzas Popup structure (Carola, 2014) to the north and by the
144 Ebro Basin to the east (**Fig. 1**). The structure is defined as a forced fold related dome
145 structure (Tavani et al., 2013; **Fig. 2**), formed by an extensional fault system with
146 migration of evaporites towards the hanging wall during the Mesozoic (Soto et al.,
147 2011). During the tectonic compressional phase, associated with the Alpine Orogeny
148 affecting the Pyrenees, the right-lateral transpressive inversion of the basement faults
149 was activated, along with the reactivation of transverse extensional faults (**Fig. 2**;
150 Tavani et al., 2013; Alcalde et al., 2014).

151 The target reservoir and seal formations consist of Lower Jurassic marine carbonates,
152 arranged in an asymmetric dome-like structure (**Fig. 2**) with an overall extent of 15 km²
153 and located at 1,485 m of depth (Alcalde et al., 2013, 2014; Ogaya et al., 2013). The
154 target CO₂ injection point is a saline aquifer formed by a dolostone unit, known as
155 “Carniolas”, and an oolitic limestone of the Sopeña Formation, both corresponding to
156 Lias in time (Early Jurassic). The estimated porosity of the Carniolas reaches over 12%

157 (Ogaya et al., 2013; Le Gallo and de Dios, 2018) and it is slightly lower at the
158 Carbonate Lias level (8.5% in average). The reservoir levels contain saline water with
159 more than 20 g/l of NaCl and very low oil content. The high porosity of the lower part
160 of the reservoir (i.e., the Carniolas level) is the result of secondary dolomitization and
161 different fracturing events (Alcalde et al., 2014). The minimum thickness of the
162 reservoir units is 100 m. The potential upper seal unit comprises Lias marlstones and
163 black shales from a hemipelagic ramp (Fig. 2); Pliensbachian and Toarcian) of the
164 “Puerto del Pozazal” and Sopeña Formations.

165

166 2.2 Regional tectonic field

167 The tectonic context has been described from two different approaches: (1) the tectonic
168 style of the fractures bordering the Hontomín reservoir (De Vicente et al., 2011; Tavani
169 et al., 2011) and (2) the tectonic regional field described from earthquakes with
170 mechanism solutions and GPS data (Herraiz et al., 2000; Stich et al., 2006; De Vicente
171 et al., 2008).

172 (1) The tectonic style of the Bureba Basin was described by De Vicente et al. (2011),
173 which classified the Basque-Cantabrian Cenozoic Basin (Fig. 1a) as transpressional
174 with contractional horsetail splay basin. The NW-SE oriented Ventaniella fault (Fig.
175 1a), includes the UFS in the southeastward area, being active between the Permian and
176 Triassic period, and strike-slip during the Cenozoic contraction. In this tectonic
177 configuration, the Ubierna Fault acts as a right-lateral strike-slip fault. These authors
178 pointed out the sharp contacts between the thrusts and the strike-slip faults in this basin.
179 Furthermore, Tavani et al. (2011) also described complex Cenozoic tectonic context
180 where right-lateral tectonic style reactivated WNW-ESE trending faults. Both the
181 Ventaniella and the Ubierna faults acted as transpressive structures forming 120 km

182 long and 15 km wide of the UFS, and featured by 0.44 mm/yr of averaged tectonic
183 strike-slip deformation between the Oligocene and the present day. The aforementioned
184 authors described different surface segments of the UFS of right-lateral strike-slip
185 ranging between 12 and 14 km length. The structural data collected by [Tavani et al.](#)
186 [\(2011\)](#) pointed out the 60% of data correspond to right lateral strike-slip with WNW-
187 ESE trend, together with conjugate reverse faulting with NE-SW, NW-SE and E-W
188 trend, and left-lateral strike-slip faults N-S oriented. They concluded that this scheme
189 could be related to a transpressional right-lateral tectonic system with a maximum
190 horizontal compression, S_{Hmax} , striking N120°E. Concerning the geological evidence of
191 recent sediments affected by tectonic movements of the UFS, [Tavani et al. \(2011\)](#)
192 suggest Middle Miocene in time for this tectonic activity. However, geomorphic
193 markers (river and valley geomorphology) could indicate tectonic activity at present-
194 times. All of these data correspond to regional or small-scale data collected to explain
195 the Basque-Cantabrian Cenozoic transpressive basin. The advantage of the
196 methodology proposed here to establish the tectonic local regime affecting the reservoir,
197 is the searching for local-scale tectonics (20 km sized), and the estimation of the depth
198 for the non-deformation surface for strata folding in transpressional tectonics ([Lisle et](#)
199 [al., 2009](#)).

200 (2) Regarding the stress field from earthquake focal mechanism solutions, [Herraiz et al.](#)
201 [\(2000\)](#) pointed out the regional trajectories of S_{Hmax} with NNE-SSW trend, and with a
202 NE-SW S_{Hmax} trend from slip-fault inversion data. [Stich et al. \(2006\)](#) obtained the stress
203 field from seismic moment tensor inversion and GPS data. These authors pointed out a
204 NW-SE Africa-Eurasia tectonic convergence at tectonic rate of 5 mm/yr approximately.
205 However, no focal mechanism solutions are found within the Hontomín area (20 km)
206 and only long-range spatial correlation could be made with high uncertainty (in time,

207 space and magnitude). The same lack of information appears in the work of De Vicente
208 et al. (2008), with no focal mechanism solutions in the 50 km surrounding the HPP. In
209 this work, these authors classified the tectonic regime as uniaxial extension to strike-slip
210 with NW-SE S_{Hmax} trend.

211 Regional data about the tectonic field inferred from different works (Herraiz et al.,
212 2000; Stich et al., 2006; De Vicente et al., 2008, 2011; Tavani et al., 2011; Tavani,
213 2012), show differences for the S_{Hmax} . These works explain the tectonic framework for
214 regional scale. Nevertheless, local tectonics could determine the low permeability and
215 the potential induced seismicity within the reservoir. In the next section, we have
216 applied the methodology described at the section 3 of this manuscript, in order to
217 compare the regional results from these works and to establish the tectonic evolution of
218 the Burgalesa Platform.

219

220 *2.3 Strategy of the ENOS European Project*

221 Hontomín pilot-plant (HPP) for CO₂ onshore storage is the only one in Europe
222 recognized as a key-test-facility, and it is managed and conducted by CIUDEN
223 (*Fundación Ciudad de la Energía*). The HPP is located within the province of Burgos
224 (**Fig. 1b**), in the northern central part of Spain.

225 The methodology proposed in this work and its application for long-term onshore GSC
226 managing in the frame of geological risk, is based on the strain tensor calculation, as
227 part of the objectives proposed in the European project “ENabling Onshore CO₂
228 Storage in Europe” (ENOS). The ENOS project is an initiative of CO₂GeoNet, the
229 European Network of Excellence on the geological storage of CO₂ for supporting
230 onshore storage and fronting the associated troubles as GSC perception, the safe storage
231 operation, potential leaking management and health, and environmental safety (Gastine

232 [et al., 2017](#)). ENOS combines a multidisciplinary European project, which focuses in
233 onshore storage, with the demonstration of best practices through pilot-scale projects in
234 the case of Hontomín facilities. Moreover, this project claims for creating a favorable
235 environment for GSC onshore through public engagement, knowledge sharing, and
236 training ([Gastine et al., 2017](#)). In this context, the work-package WP1 is devoted to
237 “ensuring safe storage operations”.

238

239 3. METHODS AND RATIONALE

240 The lithosphere remains in a permanent state of deformation, related to plate tectonics
241 motion. Strain and stress fields are the consequence of this deformation on the upper
242 lithosphere, arranging different fault patterns that determine sedimentary basins and
243 geological formations. Kinematics of these faults describes the stress/strain fields, for
244 example measuring grooves and slickensides on fault planes (see [Angelier, 1979](#),
245 [Reches, 1983 among others](#)). The relevance of the tectonic field is that stress and strain
246 determine the earthquake occurrence by the fault activity. In this work, we have
247 performed a brittle analysis of the fault kinematics, by measuring slickenfiber on fault
248 planes (dip/ dip direction and rake), in several outcrops in the surroundings of the
249 onshore reservoir. To carry out the methodology proposed in this work, the study area
250 was divided in a circle with four equal areas, and we searched outcrops of fresh rock to
251 perform the fault kinematic analysis. This allows establishing a realistic tectonic very-
252 near field to be considered during the storage seismic monitoring and long-term
253 management. Finally, we have studied the fault plane reactivation by using the Mohr-
254 Coulomb failure criterion ([Pan et al., 2016](#)), from the fault pattern obtained in the
255 Cretaceous limestone outcrop located on top of the HPP facilities.

256

257 3.1 Paleostrain Analysis

258 We have applied the strain inversion technique to reconstruct the tectonic field
259 (paleostrain evolution), affecting the Hontomín site between the Triassic, Jurassic,
260 Cretaceous and Neogene ages (late Miocene to present times). For a further
261 methodology explanation, see [Etchecopar et al. \(1981\)](#), [Reches \(1983\)](#) and [Angelier](#)
262 [\(1990\)](#). The main assumption for the inversion technique of fault population is the self-
263 similarity to the scale invariance for the stress/strain tensors. This means that we can
264 calculate the whole stress/strain fields by using the slip data on fault planes and for
265 homogeneous tectonic frameworks. The strain tensor is an ellipsoid defined by the
266 orientation of the three principal axes and the shape of the ellipsoid (k). This method
267 assumes that the slip-vectors, obtained from the pitch of the striation on different fault
268 planes, define a common strain tensor or a set in a homogeneous tectonic arrangement.
269 We assume that the strain field is homogeneous in space and time, the number of faults
270 activated is greater than five and the slip vector is parallel to the maximum shear stress
271 (τ).

272 The inversion technique is based on the Bott equations ([Bott, 1959](#)). These equations
273 show the relationship between the orientation and the shape of the stress ellipsoid:

274

$$275 \quad \text{Tan}(\theta) = [n / (1 * m)] * [m^2 - (1 - n^2) * R'] \quad [\text{eq.1}]$$

$$276 \quad R' = (\sigma_z - \sigma_x) / (\sigma_y - \sigma_x) \quad [\text{eq.2}]$$

277

278 Where l , m and n are the direction cosines of the normal to the fault plane, θ is the pitch
279 of the striation and R' is the shape of the stress ellipsoid obtained in an orthonormal
280 coordinate system, x , y , z . In this system, σ_y is the maximum horizontal stress, σ_x is the
281 minimum horizontal stress axis and σ_z is the vertical stress axis.

282

283 *3.2 The Right-Dihedral Model for Paleostrain Analysis*

284 The Right-Dihedral (RD) is a semi-quantitative method based on the overlapping of
285 compressional and extensional zones by using a stereographic plot. The final plot is an
286 interferogram figure, which usually defines the strain-regime. This method is strongly
287 robust for conjugate fault sets and with different dip values for a same tensor. The RD
288 was originally defined by Pegoraro (1972) and Angelier and Mechler (1977), as a
289 geometric method, adjusting the measured fault-slip data (slickensides) in agreement
290 with theoretical models for extension and compressive fault-slip. Therefore, we can
291 constraint the regions of maximum compression and extension related to the strain
292 regime.

293

294 *3.3 The Slip Model for the Paleostrain Analysis*

295 The Slip Model (SM) is based on the Navier-Coulomb fracturing criteria (Reches,
296 1983), taking the Anderson model solution for this study (Anderson, 1951; Simpson,
297 1997). The Anderson model represents the geometry of the fault plane as monoclinic,
298 relating the quantitative parameters of the shape parameter (K') with the internal
299 frictional angle for rock mechanics (ϕ) (De Vicente 1988; Capote et al., 1991).
300 Moreover, this model is valid for neoformed faults, and some considerations have to be
301 accounted for previous faults and weakness planes present in the rock. These
302 considerations are related to the dip of normal and compressional faults, such as for
303 compressional faulting dip values lower than 45° , reactivated as extensional faults. This
304 model shows the relationships between the K' , ϕ and the direction cosines for the
305 striation on the fault plane (De Vicente, 1988; Capote et al., 1991):

306

307 $K' = e_y / e_z$ [eq.3]

308

309 Where e_z is the vertical strain axis, e_y is the maximum horizontal shortening and e_x is
310 the minimum horizontal shortening. This model assumes that there is no change of
311 volume during the deformation and $e_y = e_x + e_z$.

312 For isotropic solids, principal strain axes coincide with the principal stress axes. This
313 means that in this work, the orientation of the principal stress axis, S_{Hmax} is parallel to
314 the orientation of the principal strain axes, e_y , and hence, the minimum stress axis, S_{hmin} ,
315 is parallel to the minimum strain axis, e_x . This assumption allows us to estimate the
316 stress trajectories (S_{Hmax} and S_{hmin}) from the e_y SM results.

317 Resolving the equations of Anderson for different values (Anderson, 1951), we can
318 classify the tectonic regime that activates one fault from the measurement of the fault
319 dip, sense of dip (0° - 360°) and pitch of the slickenside, assuming that one of the
320 principal axes (e_x , e_y or e_z) is vertical (Angelier, 1984). We can classify the tectonic
321 regime and represent the strain tensor by using the e_y and e_x orientation.

322

323 3.4 The K' strain diagram

324 Another analysis can be achieved by using the K' -strain diagram developed by Kaverina
325 et al. (1996) and codified in python-code by Álvarez-Gómez (2014). These authors have
326 developed a triangular representation based on the fault-slip, where tectonic patterns can
327 be discriminated between strike-slip and dip-slip types. This diagram is divided in 7
328 different zones according to the type of fault: (1) pure normal, (2) pure reverse and (3)
329 pure strike-slip; combined with the possibility of oblique faults: (4) reverse strike-slip
330 and (5) strike-slip with reverse component; and lateral faults: (6) normal strike-slip and
331 (7) strike-slip faults with normal component (Fig. 3). Strike-slip faults are defined by

332 small values for pitch ($p < 25^\circ$), and dips close to vertical planes ($\beta > 75^\circ$). High pitch
333 values ($p > 60^\circ$) are related to normal or/reverse fault-slip vectors. Extensional faults
334 show e_y in vertical whereas compressional faults show e_y in horizontal plane.

335 This method was originally performed for earthquake focal mechanism solutions by
336 using the focal parameters, the nodal planes (dip and strike) and rake (Kaverina et al.,
337 1996). The triangular graph is based on the equal-areal representation of the T, N or B
338 and P axes in spherical coordinates (T tensile, N or B neutral and P pressure axes), and
339 the orthogonal regression between earthquake magnitudes M_s and m_b for the Harvard
340 earthquake CMT global catalogue in 1996. [Álvarez-Gómez \(2014\)](#) presented a code
341 python-based for computing the Kaverina diagrams, and we have modified the input
342 parameters by including the K' intervals for the strain field from the SM. The
343 relationship between the original diagram of Kaverina (**Fig. 3a**) and the K' -dip diagram
344 (**Fig. 3b**) that we have used in this work is shown in the figure 3. The advantage of this
345 diagram is the fast assignation of the type of fault and the tectonic regime that determine
346 this fault pattern, and the strain axes relationship.

347 Table 1 summarizes the different tectonic regimes of the figure 3b showing the
348 relationship with the strain main axes e_y , e_x and e_z . This diagram exhibits a great
349 advantage to classify the type of fault according to the strain tensor. Therefore, we can
350 assume the type of fault from the fault orientation affecting geological deposits for each
351 strain tensor obtained.

352

353 *3.5 The Circular-Quadrant-Search (CQS) strategy for the paleostain analysis*

354 In this work, we propose a low-cost strategy based on a well-known methodology for
355 determining the stress/strain tensor affecting a GSC reservoir, which will allow the
356 long-term monitoring of the geological and seismic behavior (**Fig. 4**). The objective is

357 to obtain enough structural data and spatially homogeneous of faults (**Figs. 4, 5**) for
358 reconstructing the stress/strain tensor. The key-point is the determination of the
359 orientation of the e_y , e_x and K' to plot in a map and therefore, to establish the tectonic
360 regime. We have chosen quadrants of the circles with the aim to obtain a high-quality
361 spatial distribution of point for the interpretation of the local and very near strain field.
362 Hence, data are homogeneously distributed, instead of being only concentrated in one
363 quadrant of the circle.

364 [Pérez-López et al. \(2018\)](#) carried out a first approach to the application of this
365 methodology at Hontomín, under the objective of the ENOS project (see next section
366 for further details). We propose a circular searching of structural field stations (**Figs. 4,**
367 **5**), located within a 20 km radius. This circle was taken, given that active faults with the
368 capacity of triggering earthquakes of magnitudes close to M 6, exhibits a surface rupture
369 of tens of kilometers, according to the empirical models ([Wells and Coppersmith,](#)
370 [1994](#)). Moreover, [Verdon et al. \(2015\)](#) pointed out that the maximum distance of
371 induced earthquakes for fluid injection is 20 km. Larger distances could not be related
372 to the stress/strain regime within the reservoir, except for the case of large geological
373 structures (folds, master faults, etc.). Microseismicity in GSC reservoir is mainly related
374 to the operations during the injection/depletion stages and long-term storage ([Verdon](#)
375 [2014; Verdon et al., 2015; McNamara, 2016](#)).

376 The presence of master faults (capable to trigger earthquakes of magnitude = or > than 6
377 and 5 km long segment) inside the 20 km radius circle, implicates that the regional
378 tectonic field determines the strain accumulation in kilometric fault-sized. Furthermore,
379 the presence of master faults could increase the occurrence of micro-earthquakes, due to
380 the presence of secondary faults prone to trigger earthquakes by their normal seismic
381 cycle ([Scholz, 2018](#)). Bearing in mind that GSC onshore reservoirs use to be deep saline

382 aquifers (e.g. [Bentham and Kirby, 2005](#)) as the Hontomín case ([Gastine et al., 2017](#), [Le](#)
383 [Gallo and de Dios, 2018](#)), which is confined in folded and fractured deep geological
384 structures, in which local tectonics plays a key role in micro-seismicity and the
385 possibility of CO₂ leakage.

386 The constraints of this strategy are related to the absence of kinematics indicators on
387 fault planes. It could occur due to later overlapping geological processes as neoformed
388 mineralization. Also, a low rigidity eludes the slicken fiber formation, and no
389 kinematic data will be marked on the fault plane.. A poor spatial distribution of the
390 outcrops was also taken into account for constraining the strategy. The age of sediments
391 does not represent the age of the active deformations and hence, the active deformation
392 has to be analyzed by performing alternative methods (i.e. paleoseismology,
393 archaeoseismology).

394

395 4. RESULTS

396 *4.1 Strain Field Analysis*

397 We have collected 447 fault-slip data on fault planes in 32 outcrops, located within a 20
398 km radius circle centered at the HPP (**Fig. 5**). The age of the outcrops ranges between
399 Early Triassic to post-Miocene and are mainly located in Cretaceous limestone and
400 dolostone (**Fig. 5, Table 2**). However, no Jurassic outcrops were located, and only
401 seven stations are located on Neogene sediments, ranging between Early Oligocene to
402 Middle-Late Miocene. The small number of Neogene stations is due to the mechanical
403 properties of the affected sediments, mainly poor-lithified marls and soft-detrital fluvial
404 deposits. Despite that, all the Neogene stations exhibit high-quality data with a number
405 of fault-slip data ranging between 7 and 8, enough for a minimum quality analysis.

406 We have labeled the outcrops with the acronym HTM followed by a number (see **figure**
407 **5** for the geographical location and **Table 2** and **figure 6** for the fault data). The station
408 with the highest number of faults measured is HTM17 with 105 faults on Cretaceous
409 limestone. Conjugate fault systems can be recognized in most of the stations (HTM1, 3,
410 5, 7, 10, 14, 16, 21, 23, 24, 25, 29, 30 and 32, **Fig. 6**), although there are a few stations
411 with only one well defined fault set (6, 22, 32). We have to bear in mind that the
412 recording of conjugate fault systems is more robust for the brittle analysis than
413 recording isolated fault sets, better constraining the solution ([Žaholar and Vrabc,](#)
414 [2008](#)). In total, 29 of 32 stations were used (HTM24, 27, 28 with no quality data), and
415 from these 29 stations, 21 were analyzed with the paleostrain technique. Solutions
416 obtained here are robust to establish the paleostrain field in each outcrop as the
417 orientation of the e_y , S_{Hmax} (**Fig. 7**).

418 The results obtained from the application of the paleostrain method have been expressed
419 in stereogram, right dihedral (RD), slip method (SM) and K' - diagram (**Fig. 7**). The K' -
420 diagram shows the fault classification as normal faults, normal with strike-slip
421 component, pure strike-slip, strike-slip with reverse component and reverse faults (see
422 **Fig. 3**). Main faults are lateral strike-slips and normal faults, followed by reverse faults,
423 strike-slips and oblique strike-slips faults. The results of the strain regime are as
424 follows: 1) 43% of extensional with shear component; 2) 22% of shear; 3) 13% of
425 compressive strain (lower Cretaceous and early-middle Miocene, **Table 2**); 4) 13% of
426 pure shear and 5) 9% of shear with compression strain field, although with the presence
427 of five reverse faults.

428 In contrast, we can observe that there are solutions with a double value for the e_y , S_{Hmax}
429 orientation: HTM1, 2, 10, 11, 13, 15, 19, 26, and 30. The stations HTM3 and 23 (upper

430 Cretaceous), show the best solution for strike-slip strain field as a pure strike-slip
431 regime and e_y with N25°E and N99°E trend, respectively (**Fig. 7**).

432 It is easy to observe the agreement between the e_y results from the SM and the K'- strain
433 diagram, for instance, in the HTM2 the K'-diagram indicates strike-slip faults with
434 reverse component for low dips ($0^\circ < \beta < 40^\circ$), but also indicates strike-slip faults with
435 normal component for larger dips ($40^\circ < \beta < 90^\circ$). However, both results are in
436 agreement with a strain field defined by the orientation for e_y , S_{Hmax} with $N150^\circ \pm 18^\circ$
437 trend. This tectonic field affects Cretaceous carbonates and coincides with the regional
438 tectonic field proposed by [Herraiz et al. \(2000\)](#), [Tavani et al. \(2011\)](#) and [Alcalde et al.](#)
439 [\(2014\)](#).

440

441 *4.2 Late Triassic Outcrop Paleostrain*

442 Strain analysis from HTM5 fault set shows e_y with NW-SE trending and shear regime
443 with extension defined by strike-slip faults (**Figs. 7a**). This is in agreement with the
444 uniaxial extension described in [Tavani \(2012\)](#), constraining this regime with S_{hmin} with
445 NE-SW trending.

446

447 *4.3 Cretaceous Outcrops Paleostrain*

448 We have divided this result in two groups, (a) outcrops within the 20km circle from
449 HPP and (b) the outcrop the HTM17 (**Fig. 5**), which is located in the HPP facilities and
450 described in the next section. HTM14 is the only outcrop from Early Cretaceous age,
451 showing a compressive tectonic stage with reverse fault solutions, defined by e_y with
452 NE-SW trend (**Fig. 7b and 7c**). Taking into account the extensional stage related to the
453 Main Rifting Stage that took place in Early Cretaceous times (i.e. [Carola, 2004](#); [Tavani,](#)

454 2012; Tugend et al., 2014), we interpreted these results as a modern strain field,
455 probably related to the Cenozoic Inversion stage.
456 Outcrops HTM 2, 3, 8, 17, 19, 20, 21, 22, 23, 25, 26, 29, 31 and 32 are from the upper
457 Cretaceous carbonates (**Fig. 7**). Results are: (1) a compressive strain stage featured by e_y
458 with NW-SE trend, similar to the stage described in Tavani (2012), and (2) a normal
459 strain stage with e_y striking both E-W and NE-SW (**Fig. 7**, HTM 20, 21, 31 and 32).
460 Finally, a (3) shear stage (activated strike-slip faults) and (4) a shear with extension
461 (strike-slip with normal component) were described as well. These two late stages are
462 featured by e_y with NE-SW and NW-SE trends. The existence of four different strain
463 fields is determined by different ages during the Cretaceous and different spatial
464 locations in relation to the main structures, the Ubierna Fault System, Hontomín Fault,
465 Cantabrian Thrust, Montorio folded band and the Polientes syncline (**Fig. 1**).

466

467 4.4 Cretaceous Outcrop HTM17 on the Hontomín Pilot Plant

468 This outcrop is located on top of the geological reservoir, in a quarry of Upper
469 Cretaceous limestones. The main advantage of this outcrop is the well-development of
470 striation and carbonate microfibrils which yields high-quality data. 105 fault-slip data
471 were measured, with the main orientation striking N75°E; N-50°E; and a conjugate set
472 with N130°E ($\pm 10^\circ$) trend (**Fig. 8**). The result of the strain inversion technique shows an
473 extensional field featured by an e_y trajectory striking N107°E ($\pm 24^\circ$) related to an
474 extensional strain field (see the K' diagram in **figure 8**). Most of the faults are
475 extensional faults NE-SW and NW-SE oriented (**Fig. 9**), in agreement with the
476 extensional RD solution. Reverse faults are oriented NNE-SSW, E-W and WNW-ESE.
477 The advantage of this outcrop is the geographical and stratigraphic position. It is located
478 on top of the HPP facilities in younger sediments than the reservoir rocks. Furthermore,

479 given that the Jurassic reservoir rock and the Cretaceous upper unit are both composed
480 by carbonates, the fault pattern measured here could be a reflex of the fracture network
481 affecting the Jurassic storage rocks in depth (see **Figs. 2, 9**).

482

483 *4.5 Cenozoic outcrops strain field*

484 The Cenozoic tectonic inversion was widely described in the area by different authors
485 (e.g. Carola, 2004; Tavani, 2012; Tungend et al., 2014). This tectonic inversion is
486 related to compressive structures, activating NW-SE and NE-SW thrusts with NW-SE
487 and NNE-SSW e_y trends, respectively. The Ubierna Fault has been inverted with a
488 right-lateral transpressive kinematics during the Cenozoic (Tavani et al., 2011). Early
489 Oligocene outcrop (HTM13, **Figs. 7c**) shows a local extensional field with e_y with
490 NNE-SSW and N150°E trend. During the Lower-Middle Miocene, HTM15 and HTM30
491 outcrops exhibit the same e_y trend, but for a compressive tectonic regime (**Figs. 7d**).
492 HTM1 shows extensional tectonics with e_y oriented N50°E and N130°E. Summarizing,
493 the Cenozoic inversion and tectonic compression are detected during the Early to
494 Middle Miocene and the Oligocene. However, during the middle Miocene only one
495 extensional stage was interpreted (HTM1, **Fig. 7c**).

496 The outcrops located closer to the HPP (HTM 17, 31, 32, **Figs. 5 and 7**) show E-W
497 faults. HTM5 is located on the Ubierna Fault, showing a NW-SE trend, whilst HTM3
498 shows NE-SW strike-slip.

499 Strain analysis suggests that the planes parallel to the S_{Hmax} orientation (NNW-SSE and
500 N-S), could induce the leakage into the reservoir (**Fig. 7**). Moreover, N50°E S_{Hmax}
501 orientation could also affect the reservoir. HPP facilities are close to the Hontomin Fault
502 (**Fig. 5**), a WNW-ESE oriented fault, although the HTM17 station shows that N-S fault
503 planes could play an important role for seepage of fluid into the reservoir.

504

505 5. DISCUSSION

506 5.1 Regional active stress tensor in HTM17 fault pattern

507 The active regional field proposed by [Herraiz et al. \(2000\)](#), [Stich et al. \(2006\)](#), [Tavani et](#)
508 [al. \(2011\)](#) and [Alcalde et al. \(2014\)](#), shows e_y , S_{Hmax} with almost NNW-SSE and N-S
509 trends. Namely, the work from Herraiz et al. (2000) calculates three stress tensors
510 within the 20 km of our study area and a Quaternary stress tensor close to the area (c.a.
511 40 km southward of Hontomín). The age of the first one is Miocene, and defined by σ_1
512 $87^\circ/331^\circ$; σ_2 $01^\circ/151^\circ$; σ_3 $00^\circ/061^\circ$ (dip/dip sense 0° - 360°), with an $R=0.06$ and S_{Hmax}
513 trending $N151^\circ E$, under an extensional tectonic regime. Two post-Miocene stress
514 tensors are defined by: (1) σ_1 $87^\circ/299^\circ$; σ_2 $00^\circ/209^\circ$; σ_3 $01^\circ/119^\circ$ with $R = 0.13$, S_{Hmax}
515 with $N29^\circ E$ trend under an extensional tectonic regime and (2) σ_1 $00^\circ/061^\circ$; σ_2
516 $86^\circ/152^\circ$; σ_3 $03^\circ/331^\circ$, with $R=0.76$, and S_{Hmax} $N62^\circ E$ under strike-slip tectonic regime.
517 Finally, these authors calculated a Quaternary stress tensor defined by: σ_1 $85^\circ/183^\circ$; σ_2
518 $02^\circ/273^\circ$; σ_3 $03^\circ/003^\circ$; $R=0.02$ and S_{Hmax} with $N101^\circ E$ trend under an extensional
519 tectonic regime. The regional active stress tensor defined for Pliocene-Quaternary ages
520 is σ_1 $88^\circ/197^\circ$; σ_2 $01^\circ/355^\circ$; σ_3 $00^\circ/085^\circ$ for 327 data with $R = 0.5$ and S_{Hmax} with N-S
521 trend under an extensional tectonic regional regime.

522 We have applied the regional active stress tensor ([Herraiz et al., 2000](#)) for studying the
523 reactivation of previous fault patterns measured in HTM17 (**Figs. 8 and 9**). To carry out
524 this study, we assume that the fault plane reactivation depends on σ_1 and σ_3 , and the
525 shape of the failure envelope. Therefore, we have used the Mohr-Coulomb failure
526 criteria for preexisting fault planes ([Xu et al., 2010](#); [Labuz and Zang, 2012](#)), by using
527 the Mohr Plotter v3.0 code ([Allmendinger, 2012](#)). Moreover, to calculate the Mohr-
528 Coulomb circle, it is necessary to know the cohesion and friction parameters of the

529 reservoir rock. Bearing in mind that the reservoir rocks are Lower-Jurassic carbonates
530 (dolostone and oolitic limestone, [Alcalde et al., 2013, 2014](#); [Ogaya et al., 2013](#)), we
531 have assumed the averaged cohesion for carbonates (limestone and dolostone) in 35°
532 and the coefficient of internal friction of 0.7 ([Goodman, 1989](#)). In addition, we have
533 assumed no cohesion with an angle of static friction of 0.7 for preexisting faults.

534 Figure 10 shows the main results for the Mohr analysis. The reactivated planes under
535 the active-present stress field are red dots, 52 out of the original 105 fault-slip
536 measurements at HTM17. Green and orange dots indicate faults with no tectonic
537 strength accumulation under the present-day stress field. Reactivated fault sets are
538 oriented between N to $N60^\circ\text{E}$ and $N115^\circ$ to 180°E , with N-S and NNE-SSW as main
539 trends (**Fig. 10**, red rose diagram). Under an extensional tectonic field with $R = 0.5$, N-S
540 are normal faults, whereas NNE-SSW and NNW-SSE trends are strike-slips faults with
541 extensional component. According to the results shown in figure 10, these faults could
542 be reactivated without a pore pressure increase. The inactive fault orientation is
543 constrained between $N60^\circ\text{E}$ and $N115^\circ\text{E}$, mainly WNW-ESE (**Fig. 10**, green rose
544 diagram). Regarding the uncertainties of these fault orientations, these values can
545 oscillate $\pm 5^\circ$, according to the field error measurement (averaged error for measuring
546 structures by a compass).

547 Concerning the reliability of the results, some constrains need to be explained. The
548 Mohr-Coulomb failure criterion is an approximation that assumes that the normal stress
549 on the fault plane is not tensile. Furthermore, the increasing of pore pressure in the
550 reservoir rock reduces the normal stress on the plane of failure and the interval of fault
551 reactivation could be higher. This effect was not considered in the previous analysis
552 since the calculation of the critical pore pressure is beyond the purpose of this work.

553 Nevertheless, the MohrPlotter software (Allmendinger, 2012), allows estimating the
554 increase of pore pressure to the critical value under some conditions.

555 Finally, we have applied the Slip Model and Right Dihedral to the reactivated fault-slip
556 data from HTM17 outcrop (Fig. 11), by including the rake estimated from the active
557 regional stress tensor determined by Herraiz et al. (2000). At a glance, faults oriented
558 between N10°E and N10°W act as normal faults (4 out 52, Figs. 11a, c), faults between
559 N10°E - N50°E, and N10°W – N50°W act as extensional faults with strike-slip
560 component (31 out 52), and NE-SW and NW-SE vertical faults act as pure strike slips
561 (8 out 52). The Right Dihedral shows a tectonic regime of strike-slip with extensional
562 component (see De Vicente et al., 1992), with orthorhombic symmetry and S_{Hmax}
563 oriented N10°W, which is in agreement with the stress-tensor proposed by Herraiz et al.
564 (2000) with $\sigma_2 = 01^\circ/355^\circ$ and σ_1 vertical. However, strain analysis in this case shows
565 a strike-slip extensional tectonic regime, instead of the extensional regime derived from
566 the stress field. Despite this, both the Mohr-Coulomb analysis and the Paleostain
567 analysis (SM and RD), suggest N-S normal faulting, NNE-SSW to NE-SW and NNW-
568 SSE to NW-SE strike-slips as the active fault network affecting the reservoir. De
569 Vicente et al. (1992) pointed out that the SM analysis is more robust applied in fault-
570 slip data classified previously by other techniques. Here, we have used the Mohr
571 Coulomb failure criteria to separate active fault set under the same strain tensor,
572 yielding robustness to the results from SM and RD analysis.

573 We propose as a complementary and future work, a combined analysis between the fault
574 population analysis and the slip-tendency analysis (Morris et al. 1996), which could
575 improve and discriminate those fault sets most likely to be reactivated under an active
576 stress field. Although both analyses (Fault Population and slip-tendency) are based on

577 | the stress tensor and the orientation of fault traces, the slip-tendency also includes rock
578 | strength values obtained from the "in situ" tests.

579

580 5.2 Active faulting in the surrounding of HPP

581 Quaternary tectonic markers for the UFS are suggested by [Tavani et al. \(2011\)](#).

582 According to the tectonic behavior of this fault as right-lateral strike-slip, and the fault

583 segments proposed by [Tavani et al. \(2011\)](#), ranging between 12 and 14 km long, the

584 question is whether this fault could trigger significant earthquakes and which could be

585 the maximum associated magnitude. This is a relevant question given that the “natural

586 seismicity” in the vicinity could affect the integrity of the caprock. Bearing in mind the

587 expectable long-life for the reservoir, estimated in thousands of years, the potential

588 natural earthquake that this master fault could trigger has to be estimated. In this sense,

589 it is necessary to depict seismic scenarios related to large earthquake triggering;

590 however, this type of analysis is beyond the focus of this work.

591 The income information that we have to manage in the area of influence (20 km) is: (a)

592 the instrumental seismicity, (b) the geometry of the fault, (c) the total surface rupture,

593 (d) the upper crust thickness and (e) the heat flow across the lithosphere. Starting for the

594 heat flow value, the Hontomín wells show a value that lies between 62 and 78 mW/m²

595 at a 1,500 m depth approximately ([Fernández et al., 1998](#)). Regarding the Moho depth

596 in the area, these aforementioned authors obtained a value ranging between 36 and 40

597 km depth, while the lithosphere base ranges between 120 and 130 km depth ([Torre et](#)

598 [al., 2015](#)). The relevance of this value is the study of the thermal weakness into the

599 lithosphere that could nucleate earthquakes in intraplate areas ([Holford et al., 2011](#)). For

600 these authors, the comparison between the crustal heat-flow in particular zones, in

601 contrast with the background regional value, could explain large seismicity and high

602 rates of small earthquakes occurrence, as the case of the New Madrid seismic zone
603 (Landgraf et al., 2018). For example, in Australia heat-flow values as much as 90
604 mW/m^2 are related with earthquakes sized $M > 5$ (Holford et al., 2011).

605 Regarding the maximum expected earthquake into the zone, we have applied the
606 empirical relationships obtained by Wells and Coppersmith (1994). We have used the
607 equations for strike-slip earthquakes according to the strain field obtained in the area
608 (pure shear), and the surface rupture segment for the Ubierna Fault System, assuming a
609 surface rupture segments between 12 and 14 km (Tavani et al., 2011). The obtained
610 results show that the maximum expected earthquake ranges between $M 6.0$ and $M 6.1$.
611 Wells and Coppersmith (1994) indicate for these fault parameters a total area rupture
612 ranging between 140 and 150 km^2 . Surface fault traces rupture as lower as 7 km needs
613 at least 20 km of depth in order to reach a value of the fault-area rupturing greater than
614 100 km^2 , in line with a Moho between 36 and 40 in depth.

615 Regarding the instrumental earthquakes recorded into the area, the two largest
616 earthquakes recorded correspond to magnitude $M 3.4$ and $M 3.3$, with a depth ranging
617 between 8 and 11 km, respectively, and a felt macroseismic intensity of III (EMS98,
618 www.ign.es, last access on May, 2019). Both earthquakes occurred between 50 and 60
619 km of distance from the Hontomín Pilot Plant. Only five earthquakes have been
620 recorded within the 20-km radius area of influence and with small magnitudes ranging
621 between $M 1.5$ and $M 2.3$. The interesting data is the depth of these earthquakes,
622 ranging between 10 and 20 km, which suggest that the seismogenic crust could reach 20
623 km of depth.

624

625 *5.3 Local tectonic field and induced seismicity*

626 The fluid injection into a deep saline aquifer, which is used as GSC, generally increases
627 the pore pressure. The increasing of the pore pressure migrates from the point of
628 injection to the whole reservoir. Moreover, changes into the stress field for faults that
629 are located below the reservoir, could also trigger induced earthquakes (Verdon et al.,
630 2014). Nevertheless, to understand this possibility and the study the volumetric strain
631 field spatial distribution is required (Lisle et al., 2009).

632 We have applied a physic model to estimate the total volume injected (room conditions)
633 and in reservoir conditions.—~~and~~—~~†~~Then we have applied the McGarr's (2014)
634 approximation of the maximum expected seismic moment for induced earthquakes. The
635 injection of 10 k-tons of CO₂ in Hontomín (Gastine et al., 2017), represents an
636 approximated injected volume of CO₂ of 5.56 x10⁶ m³ (room conditions, pressure of 1
637 bar and temperature of 20 °C).—The P/T conditions at the bottom of the wells have a
638 maximum value close to 190 bar (Ortiz et al., 2015; Kovacs et al., 2015), although
639 oscillating between 125 and 170 bar and with a maximum temperature close to 58 °C.
640 Kovacs et al. (2015) pointed out a pressure gradient 0.023 MPa/m and a thermal vertical
641 gradient of 0.033 °C/m, which would correspond to a pressure of 357 bar and 51 °C at
642 1,550 m depth. P/T bottom values obtained from the observational wells (HA and HI)
643 by Ortiz et al. (2015) and Kovacs et al. (2015), were 170 bar and a temperature of 42 °C
644 respectively.

645 We have used the general law for gases $P_1 \cdot V_1 / T_1 = P_2 \cdot V_2 / T_2$. Therefore, the total
646 injected volume in reservoir conditions according to the parameters observed at the
647 bottom of the wells are, $P_1 = 1.01$ bar, $T_1 = 20$ °C, $V_1 = 5.56 \times 10^6$ m³, $P_2 = 170$ bar and
648 $T_2 = 42$ °C. Hence, the total volume of injected CO₂ plus brine is 6.94×10^4 m³.

649 McGarr (2014) empirically determined the maximum seismic moment related to a
650 volume increasing by underground injection. The expression is $M_o(\max) (\text{Nm}) = G \cdot \Delta V$

Con formato: Interlineado: Doble

Con formato: Interlineado: Doble

651 (McGarr 2014, eq. 13), where G is the modulus of rigidity and for the upper limit is 3 x
652 10¹⁰ Pa, and ΔV is the total injected volume (we have used the total injected volume in
653 reservoir conditions). The result is Mo(max) equal to 2.1 x 10¹⁵ Nm, which corresponds
654 to a maximum seismic moment magnitude Mw (max) = 4.2, by applying the equation
655 Mw = (Log Mo(max) – 9.05)/1.5 from Hanks and Kanamori (1979); where Log is the
656 logarithm to the base 10.

657 ~~We have used the expression Mo(max) (Nm) = G ΔV (McGarr 2014, eq. 13), where G~~
658 ~~is the modulus of rigidity and for the upper limit is 3 x 10¹⁰ Pa, and ΔV is the total~~
659 ~~injected volume (in room conditions). The result is Mo(max) equal to 1.67 x 10¹⁷ Nm~~
660 ~~(Joules), which corresponds to a maximum seismic moment magnitude Mw (max) =~~
661 ~~5.45, by applying the equation Mw = (Log Mo(max) – 9.05)/1.5 from Hanks and~~
662 ~~Kanamori (1979); where Log is the logarithm to the base 10.~~

Con formato: Resaltar

663 McGarr (2014) applied this approach for three cases: (1) wastewater injection, (2)
664 hydraulic fracturing, and (3) geothermal injection. We propose to include this approach
665 for fluid injection related to geological storage of CO₂. We assume that the pore
666 pressure increases from CO₂ injection in a similar way that wastewater does (originally
667 defined by Frohlich, 2012). According to McGarr (2014), the utility of the analysis we
668 have performed is “to predict in advance of a planned injection whether there will be
669 induced seismicity”, and in the case of the HPP, to estimate of the “total injected
670 volume” in a small-scale injection plant.

671 Therefore, the earthquake magnitude to this fluid-injected volume according to the
672 McGarr (2014) and Verdon et al. (2014) could be $M > 5.4$ if there are faults with a
673 minimum size of 4 km and oriented according to the present-day stress field (N-S
674 extensional faults and NNE-SSW/NNW-SSE strike slip faults; **Fig. 10**). In the case of
675 HPP, there are faults below the reservoir with this potential earthquake triggering

Con formato: Resaltar

676 (Alcalde et al., 2014). Also according to McGarr (2014), this value has not to be
677 considered as an absolute physic limit but as a qualitative approximation. Alternatively,
678 increasing by overpressure of the carbonate reservoir along with the pore pressure
679 variations of about 0.5 MPa could trigger earthquakes, as well. Stress-drop related to
680 fluid injections are also reported (Huang et al., 2016).

681 Le Gallo and de Dios (2018) described two main fault sets affecting the reservoir with
682 N-S and E-W trend, respectively. According to the present-day stress tensor described
683 by Herraiz et al. (2000) and Tavani et al. (2011), E-W fault-sets are accommodating
684 horizontal shortening, which means that the permeability could be low. Besides, these
685 faults are decoupled from the present-day stress tensor. However, N-S faults could act
686 as normal faults and, hence, with higher permeability. In this sense, the study of focal
687 mechanisms solutions could improve the safety management, even for
688 microearthquakes of magnitude lesser than M 3.

689 Moreover, the CO₂ lateral diffusion and pressure variation change during the fluid
690 injection phase, and then the system would relax before to be increased during the next
691 injection phase. In this context, the intermittent and episodic injection of CO₂ could also
692 trigger earthquakes by the stress-field and fluid pressure variations in short time periods.

693

694 6. CONCLUSIONS

695 | The application of the analysis for brittle deformation determines the active tectonic
696 | ~~evolution of the~~ strain field, applied in the ongoing seismic monitoring for Geological
697 | Carbon Storage (GSC). The possibility that pore pressure variations due to fluid
698 | injection could change the stress/strain conditions in the reservoir's caprock, makes the
699 | study of the present-day tectonic field as mandatory for the storage safety operations. In
700 | this sense, we have to bear in mind that this kind of subsurface storage is designed for

701 long-life expectancy, about thousands of years, and therefore, relevant earthquakes
702 could occur affecting the sealing and the seepage of CO₂, compromising the integrity of
703 the reservoir. Hence, we can conclude from our analysis the following items:

704 (1) The study of ~~this-the~~ tectonic field allows classifying the geometry of the faults to
705 prevent prone earthquake-related structures and design monitoring seismic network.

706 (2) The influence area around the facilities of the GSC for studying the active
707 stress/strain field could reach 20 km from the facility ~~and the tectonic evolution of the~~
708 ~~geological history of the reservoir have to be established~~, adding missing information
709 from map scale and boreholes. This information could be used from the 3D local
710 fracture pattern estimation to avoid the pore overpressure. Analysis of the stress-drop
711 due to the fluid injection could be combined with this information to understand
712 potential microseismicity associated with the injection operations.

713 (3) In the case of Hontomín Pilot-Plant, we have obtained two strain active tectonic
714 fields featured as shear deformation. These fields are defined by (a) a local tectonic
715 strain field with e_y , S_{Hmax} striking N50°E and (b) the regional one defined by e_y , S_{Hmax}
716 with N150°E trend. In this context, strike-slip faults with N-S, NNE-SSW and NNW-
717 SSE trends, are accumulating present-day tectonic deformation. Analysis of Mohr-
718 Coulomb failure criterion shows a potential reactivation of these fault sets.

719 (4) N-S faults are accumulating tectonic deformation and they could act as normal
720 faults. This means that this fault set is the preferential direction for potential fluid
721 leakage. In addition, intersection with NNE-SSW and NNW-SSE could arrange 3D
722 networks for fluid mobilization and leakage.

723 (5) The Ubierna Fault System represents a tectonically active fault array that could
724 trigger natural earthquakes as large as M 6 (± 0.1), from the empirical relationship of the
725 total rupture segment (ranging between 12 and 14 km, and the total fault-area rupture,

726 oscillating between 100 and 150 km²). Despite the lack of instrumental seismicity into
727 the influence area, we cannot obviate the potential earthquake occurrence within
728 intraplate areas due to the long- timescale expected-life of the GSC. The heat-flow
729 values and thermal crust conditions could determine the presence of intraplate
730 earthquakes with magnitude $M > 5$, for a long timescale (thousands of years), and the
731 total injected fluid could trigger induced earthquakes greater than M 4.
732 ~~The tectonic evolution and kinematics of the west part of the Burgalesa Platform~~
733 ~~domain from upper Triassic to present day show a Cretaceous tectonic inversion, local~~
734 ~~reverse strain field during the early Oligocene and early Miocene, with a Normal strain~~
735 ~~field during the middle Miocene.~~ The active strain field is now defined by an
736 extensional tectonic defined by e_y with N-S trend, activating N-S normal faults and
737 right-lateral faults with NNW- and NNE- trends.
738 Finally, we state that the determination of the active tectonic strain field, the application
739 of the slip-tendency analysis, the recognition and study of active faults within the area
740 of influence (20 km), the estimation of the maximum potential triggered natural
741 earthquake, the modeling of the stress-change during the fluid injection and stress-drop,
742 probably improve the operations for a secure storage. In a short future, earthquake
743 scenarios will be the next step: modeling the Coulomb static stress-changes due to fluid
744 injection and the modeling of intensity maps of horizontal seismic acceleration.

745

746 ACKNOWLEDGEMENTS

747 | Thanks are given to Pr. Graham Yielding, [Dr. Dave Haley](#), and an anonymous reviewer
748 | for their remarks during the open discussion. We wish to thank Pr. Allmendinger for the
749 | free use of the MohrPlotter 3.0 software, last access in March of 2020 at the web
750 | browser:

751 | <http://www.geo.cornell.edu/geology/faculty/RWA/programs/mohrplotter.html>. This
752 | work has been partially supported by the European Project ENOS: ENabling Onshore
753 | CO₂ Storage in Europe, H2020 Project ID: 653718 and the Spanish project 3GEO,
754 | CGL2017-83931-C3-2-P, MICIU-FEDER. The authors would also thank the crew of
755 | CIUDEN at Hontomín facilities for their kind assistance during our fieldwork.

756

Código de campo cambiado

757 REFERENCES

- 758 Alcalde, J., Martí, D., Calahorrano, A., Marzan, I., Ayarza, P., Carbonell, R., Juhlin, C.,
759 and Pérez-Estaún, A.: Active seismic characterization experiments of the Hontomín
760 research facility for geological storage of CO₂, Spain, *Int. J. Greenh. Gas Con.*, 19,
761 785–795, <http://dx.doi.org/10.1016/j.ijggc.2013.01.039>, 2013.
- 762 Alcalde J., Marzán I., Saura E., Martí D., Ayarza P., Juhlin C., Pérez-Estaún, A., and
763 Carbonell, R: 3D geological characterization of the Hontomín CO₂ storage site,
764 Spain: Multidisciplinary approach from seismic, well-log and regional data,
765 *Tectonophysics*, 627, 6–25, <http://dx.doi.org/10.1016/j.tecto.2014.04.025>, 2014.
- 766 Allmendinger, R. W., Cardozo, N. C., and Fisher, D.: *Structural Geology Algorithms:*
767 *Vectors & Tensors*, Cambridge, England, Cambridge University Press, 289 pp, 2012.
- 768 Álvarez-Gómez, J. A.: FMC: a one-liner python program to manage, classify and plot
769 focal mechanisms, EGU General Assembly, Vienna, Austria, 27 April-02 May,
770 EGU2014-10887, 2014.
- 771 Anderson, E. M.: *The Dynamics of Faulting and Dyke Formation with application to*
772 *Britain*, 2nd ed., Oliver and Boyd, Edinburgh, 206 pp., 1951.
- 773 Angelier, J.: Determination of the mean principal directions of stresses for a given fault
774 population, *Tectonophysics*, 56, 17-26, [https://doi.org/10.1016/0040-1951\(79\)90081-](https://doi.org/10.1016/0040-1951(79)90081-7)
775 [7](https://doi.org/10.1016/0040-1951(79)90081-7), 1979.
- 776 Angelier, J.: Tectonic analysis of fault slip data sets, *J. Geophys. Res.*, 89, 5835-5848,
777 <https://doi.org/10.1029/JB089iB07p05835>, 1984.
- 778 Angelier, J.: Inversion of field data in fault tectonics to obtain the regional stress-III. A
779 new rapid direct inversion method by analytical means, *Geophys. J. Int.*, 103, 363-
780 376, <https://doi.org/10.1111/j.1365-246X.1990.tb01777.x>, 1990.
- 781 Angelier, J. and Mechler, P.: Sur une méthode graphique de recherche des contraintes
782 principales également utilisable en tectonique et en séismologie: la méthode des
783 dièdres droits, *B. Soc. Geol. Fr.*, 19, 1309-1318,
784 <http://dx.doi.org/10.2113/gssgfbull.S7-XIX.6.1309>, 1977.
- 785 Aurell, M., Meléndez, G., Olóriz, F., Bádenas, B., Caracuel, J. E., García-Ramos, J. C.,
786 Goy, A., Linares, A., Quesada, S. and Robles, S.: Jurassic, in *The geology of Spain*,
787 pp. 213–253, The Geological Society of London., 2002.
- 788 Bentham, M. and Kirby, G.: CO₂ Storage in Saline Aquifers. *Oil Gas Sci. Technol.*, 60,
789 559-567, <https://doi.org/10.2516/ogst:2005038>, 2005.

- 790 Bott, M.H.P.: The mechanism of oblique-slip faulting, *Geol. Mag.*, 96: 109-117.
791 <https://doi.org/10.1017/S0016756800059987>, 1959.
- 792 Capote, R., De Vicente, G., and González Casado, J. M.: An application of the slip
793 model of brittle deformation to focal mechanism analysis in three different plate
794 tectonics situation. *Tectonophysics*, 191, 399-409, [https://doi.org/10.1016/0040-](https://doi.org/10.1016/0040-1951(91)90070-9)
795 1951(91)90070-9, 1991.
- 796 Calvet, F., Anglada, E. and Salvany, J. M.: El Triásico de los Pirineos, in Vera, J.A.
797 (ed.) *Geología de España*, pp. 272–274, SGE–IGME, Madrid, 2004.
- 798 Carola, E.: The transition between thin-to-thick-skinned styles of deformation in the
799 Western Pyrenean Belt. Ph. D. thesis, Universitat de Barcelona, 271 pp., 2004.
- 800 Christensen, N. P.: Report on the current state and need for further research on CO₂
801 capture and storage. CO2NET, European Carbon Dioxide Network,
802 www.co2net.com, 2004.
- 803 Chu, S.: Carbon Capture and Sequestration, *Science*, 325, 1599,
804 <http://dx.doi.org/10.1126/science.1181637>, 2009.
- 805 Dallmeyer, R. D. and Martínez-García, E., Eds.: *Pre-Mesozoic Geology of Iberia*,
806 Springer-Verlag, Berlin Heidelberg, 1990.
- 807 De Vicente, G.: Análisis Poblacional de Fallas. El sector de enlace Sistema Central-
808 Cordillera Ibérica. Ph. D. thesis, Universidad Complutense de Madrid, Spain, 317
809 pp., 1988.
- 810 De Vicente, G. Muñoz, A., Giner, J.L.: Use of the Right Dihedral Method: implications
811 from the Slip Model of Fault Population Analysis, *Rev. Soc. Geol. España*, 5(3-4), 7-
812 19. 1992.
- 813 De Vicente, G., Cloetingh, S., Muñoz-Martín, A., Olaiz, A., Stich, D., Vegas, R.,
814 Galindo-Zaldivar, J., and Fernández-Lozano, J.: Inversion of moment tensor focal
815 mechanisms for active stresses around Microcontinent Iberia: Tectonic implications,
816 *Tectonics*, 27: 1-22, <http://dx.doi.org/10.1029/2006TC002093>, 2008.
- 817 De Vicente, G., Cloetingh, S., Van Wees, J. D., and Cunha, P. P.: Tectonic
818 classification of Cenozoic Iberian foreland basins, *Tectonophysics*, 502, 38–61,
819 <http://dx.doi.org/10.1016/j.tecto.2011.02.007>, 2011.
- 820 Etchecopar, A., Vasseur, G., and Daignieres, M.: An inverse problem in microtectonics
821 for the determination of stress tensor from fault striation analysis, *J. Struct. Geol.*, 3,
822 51-65, [http://dx.doi.org/10.1016/0191-8141\(81\)90056-0](http://dx.doi.org/10.1016/0191-8141(81)90056-0), 1981.

- 823 Fernández, M., Marzán, I., Correia, A., and Ramalho, E.: Heat flow, heat production,
824 and lithospheric thermal regime in the Iberian Peninsula, *Tectonophysics*, 291, 29-
825 53, [http://dx.doi.org/10.1016/S0040-1951\(98\)00029-8](http://dx.doi.org/10.1016/S0040-1951(98)00029-8), 1998.
- 826 Foulger, G. R., Wilson, M., Gluyas, J., Julian, B. R. and Davies, R.: Global review of
827 human-induced earthquakes, *Earth-Sci. Rev.*, 178, 438–514,
828 <http://dx.doi.org/10.1016/j.earscirev.2017.07.008>, 2018.
- 829 Frohlich, C.: Two-year survey comparing earthquake activity and injection-well
830 locations in the Barnett Shale, Texas. *PNAS*, vol. 109 (35), 13934 – 13938,
831 <https://doi.org/10.1073/pnas.1207728109>, 2012.
- 832 García-Mondéjar, J., Pujalte, V. and Robles, S.: Características sedimentológicas,
833 secuenciales y tectoestratigráficas del Triásico de Cantabria y norte de Palencia,
834 *Cuad. Geol. Ibérica*, (10), 151–172, 1986.
- 835 García-Mondéjar, J., Agirrezabala, L. M., Aranburu, A., Fernández-Mendiola, P. A.,
836 Gómez-Pérez, I., López-Horgue, M. and Rosales, I.: Aptian-Albian tectonic pattern
837 of the Basque-Cantabrian Basin (Northern Spain), *Geological Journal*, 31(1), 13–45,
838 [http://dx.doi.org/10.1002/\(SICI\)1099-1034\(199603\)31:1<13::AID-GJ689>3.0.CO;2-](http://dx.doi.org/10.1002/(SICI)1099-1034(199603)31:1<13::AID-GJ689>3.0.CO;2-Y)
839 [Y](http://dx.doi.org/10.1002/(SICI)1099-1034(199603)31:1<13::AID-GJ689>3.0.CO;2-Y), 1996.
- 840 Gastine, M., Berenblyum, R., Czernichowski-lauriol, I., de Dios, J. C., Audigane, P.,
841 Hladik, V., Poulsen, N., Vercelli, S., Vincent, C., and Wildenborg, T.: Enabling
842 onshore CO₂ storage in Europe: fostering international cooperation around pilot and
843 test sites, *Energy Proced.*, 114, 5905–5915,
844 <http://dx.doi.org/10.1016/j.egypro.2017.03.1728>, 2017.
- 845 Giner-Robles, J.L., Pérez-López, R., Elez, J., Silva, P.G., Rodríguez Escudero, E.,
846 Canora, C., Rodríguez-Pascua, M.A., Bardají, T., Roquero, E., Huerta, P., Perucha,
847 M.A.: Strain analysis in the Iberian Peninsula from focal mechanism solutions,
848 seismic hazard impacts, In: C. Canora, F. Martín, E. Masana, R. Pérez y M. Ortuño,
849 Eds., pp. 249-252. Tercera reunión ibérica sobre fallas activas y paleosismología,
850 Alicante (España), 2018.
- 851 Goldberg, D. S., Kent, D. V., and Olsen, P. E.: Potential on-shore and off-shore
852 reservoirs for CO₂ sequestration in Central Atlantic magmatic province basalts, *P.*
853 *Natl. Acad. Sci. USA*, 107, 1327–1332, <http://dx.doi.org/10.1073/pnas.0913721107>,
854 2010.

Código de campo cambiado

- 855 Gómez, M., Vergés, J. and Riaza, C.: Inversion tectonics of the northern margin of the
856 Basque Cantabrian Basin, *Bulletin de la Société Géologique de France*, 173(5), 449–
857 459, <http://dx.doi.org/10.2113/173.5.449>, 2002.
- 858 Goodman, R. E.: *Introduction to Rock Mechanics*, 2nd Edition, John Wiley & Sons, Inc.,
859 New York. 576 pp., 1989.
- 860 Hanks, T.C., Kanamori, H.: A Moment Magnitude Scale, *J. Geophys. Res.*, 84 (B5),
861 2348–2350, <https://doi.org/10.1029/JB084iB05p02348>, 1979.
- 862 Herraiz, M., De Vicente, G., Lindo-Naupari, R., Giner, J., Simón, J.L., González-
863 Casado, J.M., Vadillo, O., Rodríguez-Pascua, M.A., Cicuéndez, J.I., Casas, A.,
864 Cabañas, L., Rincón, P., Cortés, A.L., Ramírez, M., and Lucini, M.: The recent
865 (upper Miocene to Quaternary) and present tectonic stress distributions in the Iberian
866 Peninsula, *Tectonics*, 19, 762–786, <https://doi.org/10.1029/2000TC900006>, 2000.
- 867 Holford, S. M., Hillis, R. R., Hand, M., and Sandiford, M.: Thermal weakening
868 localizes intraplate deformation along the southern Australian continental margin,
869 *Earth Planet. Sc. Lett.*, 305, 207–214, <http://dx.doi.org/10.1016/j.epsl.2011.02.056>,
870 2011.
- 871 Huang, Y., Beroza, G. C., and Ellsworth, W. L.: Stress drop estimates of potentially
872 induced earthquakes in the Guy-Greenbrier sequence, *J. Geophys. Res.-Sol. Ea.*, 121,
873 6597–6607, <http://dx.doi.org/10.1002/2016JB013067>, 2016.
- 874 Kaverina, A. N., Lander, A. V., and Prozorov, A. G.: Global creepex distribution and its
875 relation to earthquake-source geometry and tectonic origin, *Geophys. J. Int.*, 125,
876 249–265, <https://doi.org/10.1111/j.1365-246X.1996.tb06549.x>, 1996.
- 877 Kovacs, T., Poulussen, D.F. and de Dios, C.: Strategies for injection of CO₂ into
878 carbonate rocks at Hontomin. Final Technical Report, Global Carbon Capture and
879 Storage Institute Ltd. 2015. 66p.
880 <https://www.globalccsinstitute.com/archive/hub/publications/193428/strategies->
881 [injection-co2-carbonate-rocks-hontomin-final-technical-report.pdf](https://www.globalccsinstitute.com/archive/hub/publications/193428/strategies-injection-co2-carbonate-rocks-hontomin-final-technical-report.pdf), 2015.
- 882 Labuz, J. F., Zang, A.: Mohr–Coulomb Failure Criterion. *Rock Mech. Rock Eng.*, 45,
883 975–979, <https://doi.org/10.1007/s00603-012-0281-7>, 2012.
- 884 Landgraf, A., Kuebler, S., Hintersberger, E., Stein, S.: Active tectonics, earthquakes and
885 palaeoseismicity in slowly deforming continents, Landgraf, A., Kuebler, S.,
886 Hintersberger, E. & Stein, S. (eds) *Seismicity, Fault Rupture and Earthquake*
887 *Hazards in Slowly Deforming Regions*. Geological Society, London, Special
888 Publications, 432, <http://doi.org/10.1144/SP432.13>, 2018.

Con formato: Subíndice

- 889 Le Gallo, Y. and de Dios, J. C.: Geological Model of a Storage Complex for a CO₂
890 Storage Operation in a Naturally-Fractured Carbonate Formation, *Geosciences*, 2018,
891 8, 354, <http://dx.doi.org/10.3390/geosciences8090354>, 2018.
- 892 Le Pichon, X. and Sibuet, J.-C.: Western extension of boundary between European and
893 Iberian plates during the Pyrenean orogeny, *Earth and Planetary Science Letters*,
894 12(1), 83–88, [http://dx.doi.org/10.1016/0012-821X\(71\)90058-6](http://dx.doi.org/10.1016/0012-821X(71)90058-6), 1971.
- 895 Lepvrier, C. and Martínez-García, E.: Fault development and stress evolution of the
896 post-Hercynian Asturian Basin (Asturias and Cantabria, northwestern Spain),
897 *Tectonophysics*, 184, 345, [http://dx.doi.org/10.1016/0040-1951\(90\)90447-G](http://dx.doi.org/10.1016/0040-1951(90)90447-G), 1990.
- 898 Lisle, R. J., Aller, J., Bastida, F., Bobillo-Ares, N. C., and Toimil, N. C.: Volumetric
899 strains in neutral surface folding, *Terra Nova*, 21, 14–20,
900 <http://dx.doi.org/10.1111/j.1365-3121.2008.00846.x>, 2009.
- 901 McGarr, A.: Maximum magnitude earthquakes induced by fluid injection, *J. Geophys.*
902 *Res.*, 119, 1008–1019, <https://doi.org/10.1002/2013JB010597>, 2014.
- 903 McNamara, D.D. Methods and techniques employed to monitor induced seismicity
904 from carbon capture and storage, GNS Science Report 2015/18, 23 pp.,
905 <http://dx.doi.org/10.13140/RG.2.2.13830.98888>, 2016.
- 906 Morris, A., Ferrill, D. A. and Henderson, D. B.: Slip-tendency analysis and fault
907 reactivation, *Geology*, 24, 275-278, [7613\(1996\)024<0275:STAAFR>2.3.CO;2](http://doi.org/10.1130/0091-</u>
908 <u><a href=), 1996.
- 909 Muñoz, J. A.: Evolution of a continental collision belt: ECORS-Pyrenees crustal
910 balanced cross-section, in *Thrust Tectonics*, edited by K. R. McClay, pp. 235–246,
911 Springer Netherlands, Dordrecht., 1992.
- 912 Ogaya, X., Ledo J., Queralt P., Marcuello, A., and Quintà, A.: First geoelectrical image
913 of the subsurface of the Hontomín site (Spain) for CO₂ geological storage: A
914 magnetotelluric 2D characterization, *Int. J. Greenh. Gas Con.*, 13, 168–179,
915 <https://dx.doi.org/10.1016/j.ijggc.2012.12.023>, 2013.
- 916 Orr, F.M.: Onshore Geologic Storage of CO₂, *Science*, 325, 1656-1658,
917 <http://dx.doi.org/10.1126/science.1175677>, 2009.
- 918 Ortiz, G., Kovacs, T., Poulussen, D.F. and de Dios, C.: Hontomin reservoir
919 characterisation test, Final Technical Report. Global Carbon Capture and Storage
920 Institute Ltd. 2015. 48p. [https://www.globalccsinstitute.com/resources/publications-](https://www.globalccsinstitute.com/resources/publications-reports-research/?filter=2015-05-01,2015-07-25&type=date)
921 [reports-research/?filter=2015-05-01,2015-07-25&type=date](https://www.globalccsinstitute.com/resources/publications-reports-research/?filter=2015-05-01,2015-07-25&type=date), 2015.

- 922 Pan, P., Wu, Z., Feng, X., Yan, F.: Geomechanical modeling of CO₂ geological storage:
923 A review, *J. Rock Mech. and Geotech. Eng.*, 8, 936-947,
924 <http://dx.doi.org/10.1016/j.jrmge.2016.10.002>, 2016.
- 925 Pérez-López, R., Mediato, J.F., Rodríguez-Pascua, M.A., Giner-Robles, J.L., Martínez-
926 Orío, R., Arenillas-González, A., Fernández-Canteli, P., de Dios, J.C., Loubeau, L.:
927 Aplicación del análisis estructural y campos de deformación para el estudio de
928 sismicidad inducida en almacenamiento profundo: Hontomín, In: C. Canora, F.
929 Martín, E. Masana, R. Pérez y M. Ortuño, Eds., pp. 279-282. Tercera reunión ibérica
930 sobre fallas activas y paleosismología, Alicante (España), 2018.
- 931 Pearce, J. M.: What can we learn from Natural Analogues? An overview of how
932 analogues can benefit the geological storage of CO₂, in: *Advances in the Geological
933 Storage of Carbon Dioxide*, edited by: Lombardi, S., Altunina, L. K., and Beaubien,
934 S. E., Springer, Dordrecht, The Netherlands, 129–139, 2005.
- 935 Pegoraro, O.: Application de la microtectonique à un étude de neotectonique. Le golfe
936 Maliaque (Grèce centrale). Ph.D. thesis, U.S.T.L. Montpellier, France, 41 pp., 1972.
- 937 Permentier, K., Vercammen, S., Soetaert, S., and Schellemans, Ch.: Carbon dioxide
938 poisoning: a literature review of an often forgotten cause of intoxication in the
939 emergency department, *International Journal of Emergency Medicine*, 10, 14,
940 <http://dx.doi.org/10.1186/s12245-017-0142-y>, 2017.
- 941 Quintà, A. and Tavani S., The foreland deformation in the south-western Basque–
942 Cantabrian Belt (Spain), *Tectonophysics*, 576–577, 4–19,
943 <http://dx.doi.org/10.1016/j.tecto.2012.02.015>, 2012.
- 944 Reches, Z.: Faulting of rocks in three-dimensional strain fields, II. Theoretical analysis,
945 *Tectonophysics*, 95, 133-156, [https://doi.org/10.1016/0040-1951\(83\)90264-0](https://doi.org/10.1016/0040-1951(83)90264-0), 1983.
- 946 Reches, Z.: Determination of the tectonic stress tensor from slip along faults that obey
947 the Coulomb yield condition, *Tectonics*, 7, 849-861,
948 <https://doi.org/10.1029/TC006i006p00849>, 1987.
- 949 Rice, S. A.: Health effects of acute and prolonged CO₂ exposure in normal and sensitive
950 populations, Second Annual Conference on Carbon Sequestration, Alexandria,
951 Virginia, USA, 5-6 May, 2003.
- 952 Roca, E., Muñoz, J. A., Ferrer, O. and Ellouz, N.: The role of the Bay of Biscay
953 Mesozoic extensional structure in the configuration of the Pyrenean orogen:
954 Constraints from the MARCONI deep seismic reflection survey, *Tectonics*, 30(2),
955 <https://10.1029/2010TC002735>, 2011.

Código de campo cambiado

- 956 Röhmman, L., Tillner, E., Magri, F., Kühn, M., and Kempka, T.: Fault reactivation and
957 ground surface uplift assessment at a prospective German CO₂ storage site, *Energy*
958 *Proced.*, 40, 437–446. <http://dx.doi.org/10.1016/j.egypro.2013.08.050>, 2013.
- 959 Scholz, C.: The seismic cycle. In *The Mechanics of Earthquakes and Faulting* 3rd
960 edition, Cambridge, Cambridge University Press, pp. 228-277, 2018.
- 961 Serrano, A. and Martínez del Olmo, W.: Tectónica salina en el Dominio Cantabro–
962 Navarro: evolución, edad y origen de las estructuras salinas, in: *Formaciones*
963 *evaporíticas de la Cuenca del Ebro y cadenas periféricas, y de la zona de Levante*,
964 edited by: Orti, F. and Salvany, J.M., Empresa Nacional De Residuos Radiactivos
965 S.A, ENRESA-GPPG, Barcelona, Spain, 39–53, 1990.
- 966 Simpson, R. S.: Quantifying Anderson's fault types, *J. Geophys. Res.*, 102, 17,909–
967 17,919, <https://doi.org/10.1029/97JB01274>, 1997.
- 968 Stich, D., Serpelloni, E., Mancilla, F. L., and Morales, J.: Kinematics of the Iberia–
969 Maghreb plate contact from seismic moment tensors and GPS observations,
970 *Tectonophysics*, 426, 295–317. <https://doi.org/10.1016/j.tecto.2006.08.004>, 2006.
- 971 Soto R., Casa-Sainz A. M., and Villalaín, J. J.: Widespread Cretaceous inversion event
972 in northern Spain: evidence from subsurface and palaeomagnetic data, *Journal of the*
973 *Geological Society London*, 168, 899–912, [http://dx.doi.org/10.1144/0016-](http://dx.doi.org/10.1144/0016-76492010-072)
974 [76492010-072](http://dx.doi.org/10.1144/0016-76492010-072), 2011.
- 975 Tavani, S., Quintá, A., and Granada, P.: Cenozoic right-lateral wrench tectonics in the
976 Western Pyrenees (Spain): The Ubierna Fault System, *Tectonophysics*, 509, 238–
977 253, <http://dx.doi.org/10.1016/j.tecto.2011.06.013>, 2011.
- 978 Tavani, S.: Plate kinematics in the Cantabrian domain of the Pyrenean orogeny, *Solid*
979 *Earth*, 3, 265–292, <http://dx.doi.org/10.5194/se-3-265-2012>, 2012.
- 980 Tavani, S., Carola, C., Granada, P., Quintà, A., and Muñoz, J. A.: Transpressive
981 inversion of a Mesozoic extensional forced fold system with an intermediate
982 décollement level in the Basque - Cantabrian Basin (Spain), *Tectonics*, 32,
983 <http://dx.doi.org/10.1002/tect.20019>, 2013.
- 984 Torne, M., Fernández, M., Vergés, J., Ayala, C., Salas, M. C., Jimenez-Munt, I.,
985 Buffett, G. G., and Díaz, J.: Crust and mantle lithospheric structure of the Iberian
986 Peninsula deduced from potential field modeling and thermal analysis,
987 *Tectonophysics*, 663, 419–433, <http://dx.doi.org/10.1016/j.tecto.2015.06.003>, 2015.
- 988 Tugend, J., Manatschal, G., Kuszniir, N. J., Masini, E., Mohn, G. and Thinon, I.:
989 Formation and deformation of hyperextended rift systems: Insights from rift domain

Código de campo cambiado

- 990 mapping in the Bay of Biscay-Pyrenees, *Tectonics*, 33(7), 1239–1276,
991 <http://dx.doi.org/10.1002/2014TC003529>, 2014.
- 992 Vegas, R., Vázquez, J. T., Olaiz, A. J., and Medialdea, T.: Tectonic model for the latest
993 Triassic - Early Jurassic extensional event in and around the Iberian Peninsula,
994 *Geogaceta*, 60, 23-26, 2016.
- 995 Verdon, J. P.: Significance for secure CO₂ storage of earthquakes induced by fluid
996 injection, *Environ. Res. Lett.*, 9, 064022 (10pp), <http://dx.doi.org/10.1088/1748-9326/9/6/064022>, 2014.
- 998 Verdon, J. P., Stork, A. L., Bissell, R. C., Bond, C. E., and Werner, M. J.: Simulation of
999 seismic events induced by CO₂ injection at In Salah, Algeria, *Earth Planet. Sci. Lett.*,
1000 426, 118–129, <http://dx.doi.org/10.1016/j.epsl.2015.06.029>, 2015.
- 1001 Vergés, J., Fernández, M. and Martínez, A.: The Pyrenean orogen: pre-, syn-, and post-
1002 collisional evolution, *J. Virt. Ex.*, 08, <http://dx.doi.org/10.3809/jvirtex.2002.00058>,
1003 2002.
- 1004 Wells, D. L. and Coppersmith, K. J.: New empirical relationships among magnitude,
1005 rupture length, rupture width, rupture area, and surface displacement, *B. Seismol.*
1006 *Soc. Am.*, 84, 974–1002, 1994.
- 1007 Wilson, M. P., Foulger, G. R., Gluyas, J. G., Davies, R. J., and Julian, B. R.: HiQuake
1008 the human-induced earthquake database, *Seismol. Res. Lett.*, 88, 1560-1565,
1009 <http://dx.doi.org/10.1785/0220170112>, 2017.
- 1010 Winthaegen, P., Arts, R., and Schroot, B.: Monitoring Subsurface CO₂ Storage. *Oil Gas*
1011 *Sci. Technol.*, 60, 573-582, 2005.
- 1012 Xu, S.-S., A.F. Nieto-Samaniego, S.A. Alaniz-Álvarez: 3D Mohr diagram to explain
1013 reactivation of pre-existing planes due to changes in applied stresses, *Rock Stress*
1014 *and Earthquakes – Xie (ed.)*, 739-745 p, 2010.
- 1015 Žalohar, J. and Vrabec, M.: Combined kinematic and paleostress analysis of fault-slip
1016 data: The Multiple-slip method, *J. Struct. Geol.*, 30, 1603–1613,
1017 <http://dx.doi.org/10.1016/j.jsg.2008.09.004>, 2008.

1018

1019 **FIGURE CAPTIONS**

1020

1021 **Figure 1.** a) Location map of the study area in the Iberian Peninsula, along with the
1022 geological map of the Asturian and Basque-Cantabrian areas, labelling major units and

1023 faults (modified after Quintà and Tavani 2012); b) Geographical location of Hontomín
1024 pilot-plant (red dot) within the Basque-Cantabrian Basin. This basin is tectonically
1025 controlled by the Ubierna Fault System (UFS; NW-SE oriented) and the parallel
1026 Polientes syncline, the Duero and Ebro Tertiary basins and Poza de la Sal evaporitic
1027 diapir. Cret: Cretaceous; F: Facies.

1028

1029 **Figure 2.** Interpretation of a 2D seismic reflection profile crossing the oil exploration
1030 wells (H1, H2 and H4), along with the monitoring well (Ha) and injection well (Hi)
1031 through Hontomin Pilot Plant (HPP). Modified from Alcalde et al. (2014). See Figure 1
1032 for location, black line at the red circle.

1033

1034 **Figure 3.** a) Kaverina original diagram to represent the tectonic regime from an
1035 earthquake focal mechanism population (see Kaverina et al., 1996 and Álvarez-Gómez,
1036 2014). b) K' -strain diagram used in this work. Dotted lines represent the original
1037 Kaverina limits. Colored zones represent the type of fault. The tectonic regime is also
1038 indicated by the relationship between the strain axes and the colored legend. SS Strike
1039 slip. The B axis is the orthogonal to the P and T axes.

1040

1041 **Figure 4.** Methodology proposed to obtain the strain field affecting the GSC reservoir.
1042 The distances for outcrops and quadrants proposed is 20 km. The technique of Right
1043 Dihedral and the K' strain diagram is described in the main text. The ey and ex
1044 represented are a model for explaining the methodology. Dey and Dex are the direction
1045 of the maximum and minimum strain, respectively. Blue box at the center is the CO₂
1046 storage geological underground formation.

1047

1048 **Figure 5.** Geographical location of field outcrops in the eastern part of the Burgalesa
1049 Platform domain. Black lines: observed faults; red circle: 20km radius study zone. Rosd
1050 diagram are the fault orientations from the map. A total of 447 fault data were collected
1051 in 32 outcrops. Data were measured by a tectonic compass on fault planes at outcrops.
1052 The spatial distribution of the field stations is constrained by the lithology. Coordinates
1053 are in meters, UTM H30.

1054

1055 **Figure 6.** Stereographic representation (cyclographic plot in Schmidt net, lower
1056 hemisphere) of the fault planes measured in the field stations. “n” is the number of

1057 available data for each geostructural station. HTM24, 27, 28 are not included due to
1058 lack of data, and HTM17 due to the high number of faults.

1059

1060 **Figure 7.** Results of the paleostrain analysis obtained and classified by age. Deym:
1061 striking of the averaged of the Dey value; F: fault stereographic representation; K':
1062 diagram with dots for each fault slip solution; RD: Right Dihedral method; SM: Slip
1063 Method, K'. See Methods for further explanation.

1064

1065 **Figure 8.** Fault data from the outcrop HTM17 located on top of the HPP. See figure 5
1066 for the geographical location. Stereogram plot is lower hemisphere and Schmidt net.

1067

1068 **Figure 9.** Normal and reverse faults stereograms (lower hemisphere and Schmidt net),
1069 and rose diagrams measured in HTM17. Green arrows indicate the orientation of the
1070 local paleostrain field. Grey arrows indicate the orientation of the present-day regional
1071 stress field (Herraiz et al., 2000).

1072

1073 **Figure 10.** Mohr-Coulomb failure analysis for the fault-slip data measured in HTM17
1074 under the present-day stress tensor determined by Herraiz et al. (2000). Red dots are
1075 faults reactivated, and green and orange dots are located within the stable zone. Red
1076 rose diagram shows the orientation of reactivated faults, between N-S to N60°E and
1077 from N115°E to N180°E. Green rose diagram shows the fault orientation for faults non-
1078 reactivated under the active tress field within the area. See text for further details. The
1079 yellow data in the M-C diagrams are referred to those planes close to be reactivated, and
1080 potentially reactivated by increasing the pore pressure.

1081

1082 **Figure 11.** a) Stereogram and poles of fault sets (HTM17) reactivated under the present-
1083 day stress field suggested by Herraiz et al. (2000). b) Right-Dihedral of the reactivated
1084 fault sets. c) K'-strain diagram showing the type of fault for each fault-set.

1085

1086 **TABLE CAPTIONS**

1087

1088 **Table 1.** Different tectonic regimes, K' values, dip values and fault type for the
1089 Kaverina modified diagram used in this work. According to the strain axes relationship,
1090 faults can be classified and the tectonic regime can be established.

1091

1092 **Table 2.** Summary of the outcrops showing the number of faults, the type of the strain
1093 tensor obtained, the Dey, S_{Hmax} striking and the age of the affected geological materials.
1094 N-C is normal component for strike-slip movement.

1095